TRAJECTORY-BASED COULOMB-CORRECTED STRONG FIELD APPROXIMATION

Dissertation
zur
Erlangung des akademischen Grades
doctor rerum naturalium (Dr. rer. nat.)

der Mathematisch-Naturwissenschaftlichen Fakultät
der Universität Rostock

vorgelegt von
TIAN-MIN YAN

Rostock, 26. 11. 2012

urn:nbn:de:gbv:28-diss2013-0026-6

BETREUER:
Prof. Dr. Dieter Bauer (Institut für Physik, Universität Rostock)

GUTACHTER:
Prof. Dr. Dieter Bauer (Institut für Physik, Universität Rostock)
Prof. Dr. Manfred Lein (Institut für Theoretische Physik, Leibniz Universität Hannover)

VERTEIDIGUNG:
30. 01. 2013

ABSTRACT

The strong field approximation (SFA) is a widely used theoretical tool in the field of strong field physics and has been applied to various non-perturbative ionization processes. In particular, the SFA provides an intuitive semi-classical interpretation of strong field phenomena in terms of "quantum orbits". However, recent experimental results and *ab initio* simulations revealed deviations from the predictions of the SFA. We have developed a systematical extension of the SFA, the trajectory-based Coulomb-corrected strong field approximation (TCSFA), to explore Coulomb effects on strong field processes.

We apply the TCSFA to the ionization of hydrogen-like systems in long-wavelength, linearly polarized laser fields. Photoelectron momentum spectra are explored by comparing results from the SFA, the TCSFA and solutions of the *ab initio* time-dependent Schrödinger equation (TDSE). It is shown that the TCSFA yields good agreement with exact TDSE results.

The TCSFA provides unprecedentedly intuitive insights into the ionization dynamics. All spectral features can be interpreted in terms of trajectories. With the aid of the TCSFA, we successfully identify new types of quantum trajectories induced by the Coulomb potential and explain the origin of the recently discovered "low-energy structure" (LES). In addition, the interferences between different types of trajectories are explored to account for diverse complex interference patterns in spectra. Within the TCSFA, it is possible to distinguish the influences on interferences from real-space and under-barrier Coulomb corrections in classically forbidden regions.

ZUSAMMENFASSUNG

Die Starkfeldnäherung (engl. "strong field approximation" (SFA)) ist ein weit verbreitetes theoretisches Hilfsmittel auf dem Gebiet der Starkfeldphysik und wurde auf verschiedene nichtstörungstheoretische Ionisationsprozesse angewandt. Die SFA ermöglicht eine intuitive, semi-klassische Interpretation von Starkfeldphänomenen mittels "Quantenbahnen". Neuere experimentelle Resultate und ab initio-Simulationen haben allerdings Abweichungen von den SFA-Vorhersagen aufgezeigt. Wir haben eine systematische Erweiterung der SFA entwickelt, die trajektorien-basierte Coulomb-korrigierte Starkfeldnäherung (engl. "trajectory-based Coulomb-corrected strong field approximation" (TCSFA)), um Coulomb-Effekte in Starkfeldprozessen zu untersuchen.

Wir wenden die TCSFA auf die Ionisation von wasserstoffartigen Systemen in langwelligen, linearpolarisierten Laserfeldern an. Photoelektronenimpulsspektren werden untersucht, in dem Resultate der SFA, der TCSFA und Lösungen der ab initio zeitabhängigen Schrödinger-Gleichung (engl. "time-dependent Schrödinger equation" (TDSE)) verglichen werden. Es wird gezeigt, dass die TCSFA gute Übereinstimmung mit den exakten TDSE-Resultaten erzielt.

Die TCSFA ermöglicht bisher unerreichte, intuitive Einsichten in die Ionisationsdynamik. Alle spektralen Eigenschaften können mittels Trajektorien interpretiert werden. Mit Hilfe der TCSFA können wir erfolgreich neue Typen von Quantentrajektorien, die durch das Coulomb-Potential induziert werden, identifizieren und den Ursprung der kürzlich entdeckten "low-energy structure" (LES) erklären. Darüberhinaus werden die Interferenzen zwischen verschiedenen Typen von Trajektorien untersucht, um die vielfältigen, komplexen Interferenzmuster in den Spektren zu erfassen. Mittels der TCSFA ist es möglich, den Einfluss der Realraum- und den der Sub-Barrieren-Coulomb-Korrekturen in klassisch verbotenen Bereichen auf Interferenzen zu unterscheiden.

PUBLICATIONS

The following papers have been published in the course of the work on this thesis:

- **T.-M. Yan**, S. V. Popruzhenko, M. J. J. Vrakking and D. Bauer, *Low-energy structures in strong field ionization revealed by quantum orbits*, Phys. Rev. Lett. 105, 253002 (2010).
- P. A. Korneev, S. V. Popruzhenko, S. P. Goreslavski, **T.-M. Yan**, D. Bauer, W. Becker, M. Kübel, M. F. Kling, C. Rödel, M. Wünsche, and G. G. Paulus, *Interference Carpets in Above-Threshold Ionization: From the Coulomb-Free to the Coulomb-Dominated Regime*, Phys. Rev. Lett. 108, 223601 (2012).
- Y. Huismans, A. Gijsbertsen, A. S. Smolkowska, J. H. Jungmann, A. Rouzée, P. S. W. M. Logman, F. Lépine, C. Cauchy, S. Zamith, T. Marchenko, J. M. Bakker, G. Berden, B. Redlich, A. F. G. van der Meer, M. Yu. Ivanov, **T.-M. Yan**, D. Bauer, O. Smirnova, and M. J. J. Vrakking, *Scaling laws for photoelectron holography in the midinfrared wavelength regime*, Phys. Rev. Lett. 109, 013002 (2012).
- **T.-M. Yan**, S. V. Popruzhenko, M. J. J. Vrakking and D. Bauer, *Trajectory-Based Coulomb-Corrected Strong Field Approximation*, Multiphoton Processes and Attosecond Physics, Springer Proceedings in Physics 125, edit. K. Yamanouchi and K. Midorikawa, Chapter 37 (Springer-Verlag Berlin Heidelberg 2012).
- **T.-M. Yan** and D. Bauer, *Sub-barrier Coulomb effects on the interference pattern in tunneling ionization photoelectron spectra,* Phys. Rev. A 86, 053403 (2012).

To be published:

- **T.-M. Yan**, S. V. Popruzhenko and D. Bauer, *Trajectory-Based Coulomb-Corrected Strong Field Approximation,* Progress in Ultrafast Intense Laser Science, edit. K. Yamanouchi, K. Midorikawa, vol. 9 (Springer 2013).

CONTENTS

ACRONYMS

ATI	above-threshold ionization
HATI	high-order above-threshold ionization
HHG	high-order harmonic generation
ITM	imaginary time method
LES	low energy structure
MPI	multi-photon ionization
sub-CC	sub-barrier Coulomb correction
SFA	strong field approximation
SMM	simple man's model
SPA	saddle point approximation
SPE	saddle point equation
TCSFA	trajectory-based Coulomb-corrected strong field approximation
TDSE	time-dependent Schrödinger equation

1 INTRODUCTION

In this work we introduce a semi-classical method, the trajectory-based Coulomb-corrected strong field approximation (TCSFA), to account for the influence of Coulomb interaction between the photoelectron and the parent ion for atomic ionization in a strong field. Closely related to contemporary experiments, Coulomb effects on the photoelectron momentum distribution are explored, particularly for an atom in a long wavelength, intense laser field.

A thorough understanding of atomic ionization in strong fields is essential for further explorations and diverse applications—imaging of atomic structure, devising new light sources, investigating more complicated processes such as dynamics of molecule- or cluster-interactions with radiation fields.

In the early days of quantum mechanics, single-photon ionization has been successfully explained by Einstein's photoelectric effect. As an atom of the ionization potential I_p is subjected to a radiation field, the atom is single-ionized when the photon energy $E = \hbar\omega > I_p$. As early as in 1931, Maria Göppert-Mayer predicted two-photon transitions using time-dependent perturbation theory [3]. However, multi-photon transitions could not be experimentally confirmed due to the lack of intense radiation sources until the 1950s (for a historical review, see, e. g., [4]). Such transitions from a bound state to the continuum by absorbing multiple photons is called MULTI-PHOTON IONIZATION (MPI), which was first observed by Voronov [5] and Agostini [6]. The N-photon ionization rate satisfies a power law with respect to the laser intensity I and the number of absorbed photons N, $w = \sigma_N I^N$, where σ_N is the N-photon ionization cross section. In 1979 MPI peaks in photoelectron spectra were observed [7]. Later, experimental results showed the peaks for higher-order multi-photon absorption are even stronger than lower order peaks [8], suggesting that time-dependent perturbation theory is inapplicable and an non-perturbative theoretical treatment of nonlinear ionization is required.

Theoretically, the numerical solution of the time-dependent Schrödinger equation (TDSE) would give the exact result as long as relativistic effects need not be considered. However, even in the most simple case of a single active electron, the computational effort of solving the TDSE grows dramatically with increasing wavelength and laser intensity. The large excursions in strong fields require a sufficiently large grid to adopt the motion and the spreading of an electronic wave packet. For a many-body system the situation deteriorates due to the notorious "exponential wall" in the computational

effort [9]. Moreover, the information obtained by the TDSE often does not provide insight into the mechanisms that are responsible for certain observable phenomena.

The strong field approximation (SFA) is the most widely used theoretical tool in strong field physics, and the majority of strong field effects can be qualitatively understood within the SFA. In the SFA, the continuum state is approximated by plane-wave Gordon-Volkov states describing the oscillatory motion of an electron in a laser field but neglecting the interaction with the binding potential. The SFA transition amplitude can be reduced to a coherent superposition of semi-classical trajectories by means of the saddle point approximation (SPA). In this way, strong field ionization can be analyzed intuitively in terms of (interfering) "quantum orbits" [10, 11].

Unfortunately, the SFA is quantitatively inaccurate in many cases due to the neglect of the interaction between the photoelectron and the parent ion after the emission process. Experiments even show qualitative deviations from the predictions of the SFA. Such examples include the Coulomb-induced enhancement of the ionization rate [12, 13, 14, 15], four-fold symmetry violation of angle-resolved photoelectron distributions in elliptically polarized fields [16, 17], forward-backward symmetry violation of momentum distributions in few-cycle linearly polarized fields [18], a central minimum with a double “horn-like” structure in parallel momentum distributions [19, 20, 21, 22, 23, 24] (though its mechanism is still in debate, see, e. g., [25, 26]), a cusp-like peak at zero transverse momentum distribution [19, 27], radial fanning-out structures in the near-threshold regime [28, 29, 30, 31], the low energy structure (LES) [32, 33], and the below-threshold high-harmonic generation due to the binding potential [34, 35].

Several approaches to “patch” the SFA for Coulomb effects have been developed. The Coulomb-Volkov approximation (CVA) [36, 37] is a method applicable for a continuum electron in a “fast” ionization process using the sudden approximation. The method has been used to study photoelectron spectra [38, 39, 40]. The imaginary time method (ITM) [12] is another widely used approach to study the influence of the binding potential on tunneling processes, particularly when the quasi-classical condition is satisfied. The ITM incorporates the Coulomb interaction into the quasi-classical action along the electron trajectories in the classically forbidden region (sub-barrier region), as the electron is moving under the barrier formed by the laser field and the ionic potential. The concept of ITM, as an important element in our work, is discussed in Chapter 3. The Eikonal-Volkov approximation (EVA) is a theory with the aim of retaining the applicability to both fast and slow ionization [41, 42, 43, 44]. The classical-trajectory Monte-Carlo method [45] in

combination with semi-classical tunneling rates is also used to study long-range Coulomb effects on continuum electrons [46, 18, 33, 47].

In this work, we present a unified semi-classical approach to tackle atomic ionization in strong fields of near- or mid-infrared wavelengths. In particular we focus on the analysis of two-dimensional photoelectron momentum distributions which allows for straightforward comparisons with contemporary experimental or *ab initio* results. The work is organized as follows.

In Chapter 2, the general concept of strong field physics and the SFA transition amplitude is introduced. We use the method of asymptotic expansions to reduce the transition amplitude in integral form to a summation over "quantum trajectories". The intuitive picture of quantum orbits in this chapter lays the cornerstone for the development of the TCSFA.

In Chapter 3, we give a brief review of the ITM. The ITM is used to account for the tunneling process in the TCSFA and to describe the sub-barrier trajectories before the electron enters the continuum. Choosing proper boundary conditions, a unified view of strong field ionization in terms of trajectories becomes available.

In Chapter 4, we introduce the TCSFA by incorporating Coulomb interaction into trajectories. Both trajectories and actions are modified. Details of the numerical implementation are also discussed. We apply the TCSFA method to the study of the interaction between hydrogenlike atoms and monochromatic laser fields. Doubly-differential momentum distributions obtained with the TCSFA are presented. The spectral features are analyzed with a trajectory analysis. In addition, the recently revealed "ionization surprise" [48]—the LES [32, 33] in mid-infrared laser fields is investigated using the TCSFA. The TCSFA results reveal a similar ionization enhancement in the low energy regime of momentum spectra. By analyzing trajectories, the root of the ionization enhancement is found being related to classical boundaries (caustics).

In Chapter 5, interference patterns in momentum spectra are investigated, and a systematical analysis based on phase differences is performed.

Finally, a conclusion is given in Chapter 6.

2 STRONG FIELD APPROXIMATION

The strong field approximation (SFA) is a widely used theoretical approach to tackle field-atom or field-molecule interaction in the non-perturbative regime, as well as high-order harmonic generation (also known as the Lewenstein model) [49], and non-sequential double ionization [50, 51, 52, 53, 54, 55]. In this Chapter, we provide a consistent introduction to basic concepts of strong field physics and the SFA. Atomic units are used unless noted otherwise, i.e., $\hbar = m_e = 1$, $e = -1$, m_e being the electron mass.

2.1 INTENSE LASER-MATTER INTERACTION

2.1.1 *Choice of Gauge*

Let us consider an electron coupled to an electromagnetic field described by the Hamiltonian,

$$\hat{H}(t) = \frac{1}{2}\left[\hat{\vec{p}} + \vec{A}(\vec{r},t)\right]^2 - \phi(\vec{r},t),$$

where ϕ is the scalar potential and $\vec{A}(\vec{r},t)$ is the vector potential.

In terms of $\phi(\vec{r},t)$ and $\vec{A}(\vec{r},t)$, the electric and magnetic fields are given by

$$\vec{E}(t) = -\frac{\partial \vec{A}}{\partial t} - \nabla\phi, \quad \vec{B}(t) = \nabla \times \vec{A}. \tag{1}$$

The way to choose $\vec{A}(\vec{r},t)$, $\phi(\vec{r},t)$, and the wave function ψ is not unique. They are left invariant under the gauge transform

$$\phi' = \phi - \frac{\partial \chi}{\partial t}, \quad \vec{A}' = \vec{A} + \nabla\chi, \quad \psi' = e^{-i\chi}\psi, \tag{2}$$

with the arbitrary $\chi \equiv \chi(\vec{r},t)$ being the generating function of the gauge $(\phi, \vec{A})$ to $(\phi', \vec{A}')$. Gauge transformations do not affect observables and offer possibility to choose the most suitable gauge for the problem to solve. However, gauge invariance may be violated if approximations are applied.

Velocity gauge and length gauge (also called Göppert-Mayer gauge [3]) are commonly used for problems of field-matter interaction. In the velocity gauge,

$$\phi^{\mathrm{V}}(\vec{r},t) = 0, \quad \vec{A}^{\mathrm{V}}(\vec{r},t) = \vec{A}(\vec{r},t). \tag{3}$$

Hence, the Hamiltonian is

$$\hat{H}^{\mathrm{V}}(t) = \frac{1}{2}\left[\hat{\vec{p}} + \vec{A}(\vec{r},t)\right]^2, \tag{4}$$

and the instantaneous (physical) momentum is given by $\vec{v} = \vec{p} + \vec{A}(t)$. In our work, the dipole approximation is used. We assume that the wavelength of the laser is large compared to the interaction region, i. e., the spatial dependence of the light field is negligible, $\vec{A}(r,t) \simeq \vec{A}(t)$. The transformation from velocity gauge to length gauge can be conducted with the generating function

$$\chi = -\vec{A}^{\mathrm{V}}(t) \cdot \vec{r}. \tag{5}$$

Substituting (5) into (2), we obtain ϕ and $\vec{A}$ in length gauge,

$$\phi^{\mathrm{L}} = -\vec{E}(t) \cdot \vec{r}, \quad \vec{A}^{\mathrm{L}}(t) = 0, \tag{6}$$

and the Hamiltonian

$$\hat{H}^{\mathrm{L}}(t) = \frac{1}{2}\hat{\vec{p}}^2 + \vec{r} \cdot \vec{E}(t). \tag{7}$$

2.1.2 *Gordon-Volkov state*

The motion of a free electron in an external electromagnetic field is quantum mechanically described by Gordon-Volkov states. In the non-relativistic limit, the Gordon-Volkov wave function in velocity gauge reads

$$\psi_{\vec{p}}^{(\mathrm{GV,V})}(\vec{r},t) = \frac{1}{(2\pi)^{3/2}} \exp\left\{ i \left[\vec{p} \cdot \vec{r} - \frac{1}{2}\int_0^t dt' \left(\vec{p} + \vec{A}(t') \right)^2 \right] \right\}, \tag{8}$$

or in Dirac's notation

$$|\psi_{\vec{p}}^{(\mathrm{GV,V})}(t)\rangle = |\vec{p}\rangle \exp\left[-iS_{\vec{p}}(t) \right], \tag{9}$$

where $|\vec{p}\rangle$ is the plane wave state of momentum $\vec{p}$, and

$$S_{\vec{p}}(t) = \frac{1}{2}\int_0^t d\tau \left[\vec{p} + \vec{A}(\tau) \right]^2.$$

In the length gauge, applying the gauge transform (2), the Gordon-Volkov state is given by

$$|\psi_{\vec{p}}^{(\mathrm{GV,L})}(t)\rangle = |\vec{p} + \vec{A}(t)\rangle \exp\left[-iS_{\vec{p}}(t) \right]. \tag{10}$$

2.2 STRONG FIELD APPROXIMATION

Let us consider the ionization process of an atom in a strong laser field of the electric field component $\vec{E}(t)$ in the dipole approximation. Initially, the atom is in the bound state $|\psi_0(t)\rangle = |\psi_0\rangle e^{iI_p t}$ of the binding potential $\hat{V}(\vec{r})$. I_p is the ionization potential. The Hamiltonian of an atom coupled to a time-dependent external field, which is described by an operator $\hat{W}(t)$, is given by

$$\hat{H}(t) = -\frac{1}{2}\nabla^2 + \hat{V}(\vec{r}) + \hat{W}(t). \tag{11}$$

The laser-induced ionization corresponds to the transition from the initial state $|\psi_0(t)\rangle$ to the continuum state $|\psi_{\vec{p}}(t)\rangle$ of the asymptotic momentum $\vec{p}$. The transition amplitude reads

$$M_{\vec{p}}(t_f, t_i) = \langle \psi_{\vec{p}}(t_f) | \hat{U}(t_f, t_i) | \psi_0(t_i) \rangle, \tag{12}$$

where $\hat{U}(t_f, t_i)$ is the exact time-evolution operator for the Hamiltonian (11) from the initial time t_i to the final time t_f. The simultaneous presence of the external light field and the atomic potential restrains one from finding analytical solutions to the TDSE. Let us consider separately

$$\hat{H}_0(t) = -\frac{1}{2}\nabla^2 + \hat{V}(\vec{r}), \tag{13}$$

$$\hat{H}^{(\mathrm{GV})}(t) = -\frac{1}{2}\nabla^2 + \hat{W}(t). \tag{14}$$

$\hat{H}_0(t)$ and $\hat{H}^{(\mathrm{GV})}(t)$ describe a bound electron in an unperturbed atom, and a free electron in an external field, respectively. Correspondingly, the time evolution operators are denoted by $\hat{U}_0(t, t')$ and $\hat{U}^{(\mathrm{GV})}(t, t')$. The eigenstate of $\hat{H}_0(t)$ is $|\psi_0(t)\rangle$, while the eigenstates of $\hat{H}^{(\mathrm{GV})}(t)$ are Gordon-Volkov states (10), as discussed in Sec. 2.1.2. With this decomposition we are able to utilize the integral forms expanded in $\hat{U}_0$ and $\hat{U}^{(\mathrm{GV})}$,

$$\hat{U}(t, t') = \hat{U}_0(t, t') - i \int_{t'}^{t} d\tau \hat{U}(t, \tau) \hat{W}(\tau) \hat{U}_0(\tau, t') \tag{15}$$

$$= \hat{U}_0(t, t') - i \int_{t'}^{t} d\tau \hat{U}_0(t, \tau) \hat{W}(\tau) \hat{U}(\tau, t') \tag{16}$$

and

$$\hat{U}(t, t') = \hat{U}^{(\mathrm{GV})}(t, t') - i \int_{t'}^{t} d\tau \hat{U}(t, \tau) \hat{V}(\vec{r}) \hat{U}^{(\mathrm{GV})}(\tau, t') \tag{17}$$

$$= \hat{U}^{(\mathrm{GV})}(t, t') - i \int_{t'}^{t} d\tau \hat{U}^{(\mathrm{GV})}(t, \tau) \hat{V}(\vec{r}) \hat{U}(\tau, t'), \tag{18}$$

respectively.

Substituting (15) into (12) and using the orthogonality $\langle \psi_{\vec{p}}(t_f) | \psi_0(t_i) \rangle = 0$, the transition matrix element reads

$$M_{\vec{p}}(t_f, t_i) = -i \int_{t_i}^{t_f} d\tau \langle \psi_{\vec{p}}(t_f) | \hat{U}(t_f, \tau) \hat{W}(\tau) | \psi_0(\tau) \rangle. \tag{19}$$

Substituting (18) into (19), we have $M_{\vec{p}}(t_f, t_i)$ split in two terms,

$$M_{\vec{p}}(t_f, t_i) = -i \int_{t_i}^{t_f} d\tau \langle \psi_{\vec{p}}(t_f) | \hat{U}_0^{(\mathrm{GV})}(t_f, \tau) \hat{W}(\tau) | \psi_0(\tau) \rangle$$
$$- \int_{t_i}^{t_f} d\tau \int_{\tau}^{t_f} dt \langle \psi_{\vec{p}}(t_f) | \hat{U}^{(\mathrm{GV})}(t_f, t) \hat{V}(\vec{r}) \hat{U}(t, \tau) \hat{W}(\tau) | \psi_0(\tau) \rangle. \tag{20}$$

The first part of (20), as the transition amplitude of the zeroth-order, is denoted by

$$M_{\vec{p}}^{(0)}(t_f,t_i) = -i\int_{t_i}^{t_f} d\tau \langle \psi_{\vec{p}}(t_f)|\hat{U}_0^{(\mathrm{GV})}(t_f,\tau)\hat{W}(\tau)|\psi_0(\tau)\rangle. \tag{21}$$

Using the relation

$$\int_{t_i}^{t_f} d\tau \int_{\tau}^{t_f} dt = \int_{t_i}^{t_f} dt \int_{t_i}^{t_f} d\tau\Theta(t-\tau) = \int_{t_i}^{t_f} dt \int_{t_i}^{t} d\tau,$$

where $\Theta(t-\tau)$ is the Heaviside function, we recast the second part of (20) in the form

$$M_{\vec{p}}^{(1)}(t_f,t_i) = -\int_{t_i}^{t_f} dt \langle \psi_{\vec{p}}(t_f)|\hat{U}^{(\mathrm{GV})}(t_f,t)\int_{t_i}^{t} d\tau \hat{V}(\vec{r})\hat{U}(t,\tau)\hat{W}(\tau)|\psi_0(\tau)\rangle. \tag{22}$$

Both (21) and (22) are still exact. Further expansion of the full propagator $\hat{U}(t,\tau)$ may lead to transition matrix elements of higher orders.

In the SFA, the substitution of the final state, $\langle \psi_{\vec{p}}(t_f)| \to \langle \psi_{\vec{p}}^{(\mathrm{GV})}(t_f)|$, is made. The interpretation of the substitution is that the electron is free from the influence of the binding potential after it transits into the continuum. Using

$$\hat{U}^{(\mathrm{GV})}(t,t') = \int d\vec{k}|\psi_{\vec{k}}^{(\mathrm{GV})}(t)\rangle\langle\psi_{\vec{k}}^{(\mathrm{GV})}(t')| \tag{23}$$

and the orthogonality $\langle \psi_{\vec{p}}^{(\mathrm{GV})}(t_f)|\psi_{\vec{k}}^{(\mathrm{GV})}(t_f)\rangle = \delta(\vec{p}-\vec{k})$, we find from (21) that

$$M_{\vec{p}}^{(0)}(t_f,t_i) = -i\int_{t_i}^{t_f} d\tau \langle \psi_{\vec{p}}^{(\mathrm{GV})}(\tau)|\hat{W}(\tau)|\psi_0(\tau)\rangle, \tag{24}$$

and from (22) that

$$M_{\vec{p}}^{(1)}(t_f,t_i) = -\int_{t_i}^{t_f} dt \langle \psi_{\vec{p}}^{(\mathrm{GV})}(t)|\int_{t_i}^{t} d\tau \hat{V}(\vec{r})\hat{U}(t,\tau)\hat{W}(\tau)|\psi_0(\tau)\rangle. \tag{25}$$

Equations (24) and (25) account for the so-called "direct" ionization and the rescattering process, respectively.

2.2.1 *"Direct" Ionization*

The transition amplitude (26) is also called the Keldysh–Faisal–Reiss (KFR) amplitude [56, 57, 58]. Substituting the Gordon-Volkov state (10) and the interaction $\hat{W} = \vec{r}\cdot\vec{E}(t)$ [see Eq. (6)] into (24), the transition matrix element in the length gauge is given by

$$M_{\vec{p}}^{(0)}(t_f,t_i) = -i\int_{t_i}^{t_f} d\tau \langle \vec{p}+\vec{A}(\tau)|\vec{r}\cdot\vec{E}(\tau)|\psi_0\rangle e^{iS_{I_p,\vec{p}}(\tau)} \tag{26}$$

with

$$S_{I_p,\vec{p}}(t) \equiv S_{\vec{p}}(t) + I_p t = \int_0^t \left[\frac{1}{2}\left(\vec{p} + \vec{A}(\tau)\right)^2 + I_p\right] d\tau. \tag{27}$$

$M_{\vec{p}}^{(0)}$ accounts for the direct ionization, which implies an electron lifted into the continuum is driven towards the detector by external light fields without further interactions with the core.

In the following we present the calculation of the transition amplitude (26). In principle, the S-matrix theory requires the initial time $t_i \to -\infty$, and the final time $t_f \to \infty$ represents the time when the photoelectron arrives at the detector in experiments. Practically, we use $t_i = 0$ and $t_f = T_p$, where T_p is the time when the laser pulse is switched off. Expressing (26) in the position $\vec{r}$-representation, we obtain

$$M_{\vec{p}}^{(0)} = -i \int_0^{T_p} d\tau \left[\int d\vec{r} e^{-i\left(\vec{p}+\vec{A}(\tau)\right)\cdot\vec{r}} \psi_0(\vec{r})\right] \vec{r}\cdot\vec{E}(\tau) e^{iS_{I_p,\vec{p}}(\tau)}, \tag{28}$$

where $\psi_0(\vec{r}) = \langle\vec{r}|\psi_0\rangle$. With $\vec{q} \equiv \vec{p} + \vec{A}(\tau)$, we have

$$\begin{aligned}
M_{\vec{p}}^{(0)} &= -i \int_0^{T_p} d\tau \left[\int d\vec{r}\vec{r} e^{-i\vec{q}\cdot\vec{r}} \psi_0(\vec{r})\right] \cdot \vec{E}(\tau) e^{iS_{I_p,\vec{p}}(\tau)} \\
&= -i \int_0^{T_p} d\tau \left[i \int d\vec{r} \frac{d}{d\vec{q}} \left(e^{-i\vec{q}\cdot\vec{r}}\right) \psi_0(\vec{r})\right] \cdot \vec{E}(\tau) e^{iS_{I_p,\vec{p}}(\tau)} \\
&= \int_0^{T_p} d\tau \frac{d}{d\vec{q}} \left[\int d\vec{r} e^{-i\vec{q}\cdot\vec{r}} \psi_0(\vec{r})\right] \cdot \vec{E}(\tau) e^{iS_{I_p,\vec{p}}(\tau)} \\
&= \int_0^{T_p} d\tau \frac{d}{d\vec{q}} \left[\tilde{\psi}_0(\vec{q})\right] \cdot \vec{E}(\tau) e^{iS_{I_p,\vec{p}}(\tau)},
\end{aligned} \tag{29}$$

where $\tilde{\psi}_0(\vec{q})$ is the Fourier transform of $\psi_0(\vec{r})$. Details of $\tilde{\psi}_0(\vec{q})$ for different states are listed in Sec. A.1. Taking the ground state of atomic hydrogen for instance, we have

$$M_{\vec{p}}^{(0)} = 2^{7/2} \left(2I_p\right)^{5/4} \int_0^{T_p} d\tau \frac{\vec{q}\cdot\vec{E}(\tau)}{\pi\left(\vec{q}^2 + 2I_p\right)^3} e^{iS_{I_p,\vec{p}}(\tau)}. \tag{30}$$

Since the Gordon-Volkov state describes a free electron in an external light field, the SFA in the form of $M_{\vec{p}}^{(0)}$ neglects the influence of binding potential after the emission.

The direct ionization predicted by (26) is within the energy range $E \leq 2U_p$, in agreement with the $2U_p$ cut-off derived from the classical model without re-scattering processes (see Sec. 2.4). However, actual photoelectron spectra extend beyond $2U_p$, though the corresponding ionization probability is usually much lower. In order to correctly account for the spectral distribution for $E > 2U_p$, it is necessary to include the high-order matrix element (25).

2.2.2 *High-Order Ionization*

Analogous to direct ionization, it is straightforward to interpret the high-order transition amplitude (25) in terms of a multiple-step process. The first step in (25) depicts an electron interacting with an external field $\hat{W}$ where the atom is ionized at time τ. Subsequently, the photoelectron propagates within the time interval $[t, \tau]$, as described by $\hat{U}(t, \tau)$. At time t, the interaction with the binding potential $\hat{V}(\vec{r})$ occurs, that is, rescattering takes place. In the study of strong field ionization, the above process accounts for photoelectrons with energies beyond $2U_p$, which is known as high-order above-threshold ionization (HATI).

In the following the first-order transition amplitude within the SFA in length gauge is presented. One should note that the full propagator $\hat{U}(t, \tau)$ in (25) is unknown. Making the assumption $\hat{U}(t, \tau) \to \hat{U}^{(\mathrm{GV})}(t, \tau)$ and using (23) for $\hat{U}^{(\mathrm{GV})}(t, \tau)$, we obtain

$$\begin{aligned} M_{\vec{p}}^{(1)}(t_f, t_i) = -\int_{t_i}^{t_f} dt \int_{t_i}^{t} d\tau \int d\vec{k} \langle \psi_{\vec{p}}^{(\mathrm{GV})}(t) | \hat{V}(\vec{r}) | \psi_{\vec{k}}^{(\mathrm{GV})}(t) \rangle \\ \times \langle \psi_{\vec{k}}^{(\mathrm{GV})}(\tau) | \hat{W}(\tau) | \psi_0(\tau) \rangle. \end{aligned} \tag{31}$$

Substituting (10) into (31), we find

$$\begin{aligned} M_{\vec{p}}^{(1)}(t_f, t_i) &= -\int_{t_i}^{t_f} dt \int d\vec{k} \langle \vec{p} + \vec{A}(t) | \hat{V}(\vec{r}) | \vec{k} + \vec{A}(t) \rangle e^{iS_{\vec{p}}(t)} e^{-iS_{\vec{k}}(t)} \\ &\quad \times \int_{t_i}^{t} d\tau \langle \vec{k} + \vec{A}(\tau) | \vec{r} \cdot \vec{E}(\tau) | \psi_0 \rangle e^{iS_{I_p, \vec{k}}(\tau)} \\ &= -\int_{t_i}^{t_f} dt e^{iS_{I_p, \vec{p}}(t)} \int_{t_i}^{t} d\tau I_{\vec{k}}(t, \tau) \end{aligned} \tag{32}$$

where

$$\begin{aligned} I_{\vec{k}}(t, \tau) &= \int d\vec{k} \langle \vec{p} + \vec{A}(t) | \hat{V}(\vec{r}) | \vec{k} + \vec{A}(t) \rangle \langle \vec{k} + \vec{A}(\tau) | \vec{r} \cdot \vec{E}(\tau) | \psi_0 \rangle \\ &\quad \times e^{i\left[S_{I_p, \vec{k}}(\tau) - S_{I_p, \vec{k}}(t)\right]}. \end{aligned} \tag{33}$$

Analogous to the practical evaluation of the zeroth-order transition amplitude, we consider the upper limit $t_f = T_p$, since numerical calculations have shown that the contribution of the amplitude from $[T_p, \infty]$ is small. The reason is that, according to the classical theory, the electron energy does not change after the elastic rescattering because the field is off for $t > T_p$.

2.3 SADDLE POINT APPROXIMATION AND QUANTUM ORBITS

We assume that N photons, each having the energy $\hbar\omega$, are required to overcome the ionization potential I_p. If $N = I_p/\hbar\omega \gg 1$, we resort to the SPA to simplify the transition amplitudes (26) and (32). The SPA can significantly alleviate computational burdens. Moreover, it is endowed with an intuitive picture of quantum orbits.

2.3.1 *Zeroth-Order Transition Amplitude*

Since the action $S_{I_p,\vec{p}}(t)$, as an exponent, is a rapidly oscillating function of t, we can use the SPA by deforming the contour integral in the complex plane and passing near a saddle point, to approximate the integral (26) (see, e. g., [59], about techniques for asymptotic expansions of integrals). The integration over τ in (26) is thus recast in the form of a sum over saddle points $\{t_s^{(\alpha)}\}$,

$$M_{\vec{p}}^{(0)} = -\frac{\kappa}{\sqrt{2}} \sum_{\alpha} \frac{e^{iS_{I_p,\vec{p}}(t_s^{(\alpha)})}}{S''_{I_p,\vec{p}}(t_s^{(\alpha)})}, \tag{34}$$

where $\kappa = \sqrt{2I_p}$ is the characteristic momentum of a bound electron, and S'' denotes the second-order time derivative of $S_{I_p,\vec{p}}(t)$. The αth saddle point $t_s^{(\alpha)}$ satisfies the saddle point equation (SPE),

$$\frac{1}{2}\left[\vec{p} + \vec{A}(t_s^{(\alpha)})\right]^2 = -I_p. \tag{35}$$

The solution $t_s^{(\alpha)}$ of (35) is complex if $I_p > 0$, which is the case for atomic bound-states. Not all $t_s^{(\alpha)}$ fulfilling (35) for a given $\vec{p}$ are physical. Therefore we impose two restrictions for valid saddle points.

Firstly, the real part of $t_s^{(\alpha)}$, $t_r = \mathrm{Re}t_s$, is required to be within the time interval when the laser is present, i. e., $0 < t_r < T_p$. In the picture of the tunneling ionization, t_r is the time when an electron reaches the outer turning point of the potential barrier and enters the continuum. The first condition guarantees that, only when a light field is present can an atom be ionized.

Secondly, the imaginary part of t_s, $t_i = \mathrm{Im}t_s$, should satisfy $\mathrm{Im}t_s > 0$. According to the general theory of adiabatic transitions [60, 61], the final-state energy is higher than the initial-state energy. Only when t_s stays in the positive-half complex time plane can we find a sensible tunneling ionization probability, which is closely related to t_i. Given a momentum $\vec{p}$, $t_i^{(\alpha)}$ determines the weight of the αth trajectory in the final spectra. Generally, a small $t_i^{(\alpha)}$ assigns a large weight to the αth term in (34), and conceivably the smallest $t_i^{(\alpha)}$ corresponds to $t_r^{(\alpha)}$ when the absolute amplitude of an electric field is near the local maximum.

Besides the benefit from substantially reduced efforts at numerical integrations, by virtue of "quantum orbits" [10, 11], the sum (34) offers deeper insights than the integral form (26). The concept of quantum orbits helps analyze complicated ionization dynamics by "sewing quantum mechanical flesh onto classical bones" [62]. Classical properties with regard to trajectories are quite intuitive. Quantum-mechanically, on one hand, the coherent summation over different trajectories with the same asymptotic momentum manifests

the "multi-slit-in-time" nature in ionization processes [63, 64]. On the other hand, the quantum tunneling is naturally depicted with quasi-classical methods by incorporating complex trajectories extending to classically forbidden regions. The analysis using complex trajectories is generally known as ITM [65] (see Chapter 3). Both complex and classical trajectories are determined by solving Newton's equation of motion. However, we leave details about how trajectories are evaluated to the unified treatment together with the TCSFA in Chapter 4.

2.3.2 *High-Order Transition Amplitude*

The SPA is also applicable to evaluating the HATI transition amplitude (32). Applying the SPA to the integral (33) over the intermediate momentum $\vec{k}$, we solve the SPE

$$\frac{d}{d\vec{k}}\left[S_{I_p,\vec{k}}(\tau) - S_{I_p,\vec{k}}(t)\right]\Big|_{\vec{k}=\vec{k}_s} = 0$$

and find the saddle point

$$\vec{k}_s = -\frac{\vec{\alpha}(t) - \vec{\alpha}(\tau)}{t-\tau},$$

where $\vec{\alpha}(t)$ is the excursion of the electron,

$$\vec{\alpha}(t) = \int_0^t \vec{A}(t')dt'. \tag{36}$$

Hence the integral (33) is reduced to

$$I_{\vec{k}}(t,\tau) \simeq \left[\frac{2\pi}{i\,(t-\tau)}\right]^{3/2} V_{\vec{p},\vec{k}_s}(t)\langle\vec{k}_s + \vec{A}(\tau)|\vec{r}\cdot\vec{E}(\tau)|\psi_0\rangle e^{i\Delta S_{I_p,k}(t,\tau)} \tag{37}$$

with the matrix element for the rescattering potential

$$V_{\vec{p},\vec{k}}(t) \equiv \langle\vec{p} + \vec{A}(t)|\hat{V}(\vec{r})|\vec{k} + \vec{A}(t)\rangle \tag{38}$$

and the action

$$\Delta S_{I_p,k}(t,\tau) = S_{I_p,\vec{k}}(\tau) - S_{I_p,\vec{k}}(t).$$

With the short-range interaction modeled by Yukawa's potential $V(r) = -\,(b + a/r)\exp(-\lambda r)$, the matrix element (38) is given by

$$V_{\vec{p},\vec{k}}(t) \to V_{\vec{p},\vec{k}} = -\frac{2b\lambda + aC}{2\pi^2 C^2}, \qquad C = \left(\vec{p} - \vec{k}\right)^2 + \lambda^2.$$

2.4 CLASSICAL DESCRIPTION: SIMPLE MAN'S MODEL

The simple man's model (SMM) describes the classical limit of quantum orbits, and we can use the SMM to estimate the cutoff in above-threshold ionization (ATI) [66], HATI, [67, 68] and high-order harmonic

generation (HHG) spectra [45]. In the SMM, the assumption $I_p = 0$ leads to $t_s \in \mathbb{R}$, and hence quantum orbits become classical trajectories. Still, the Coulomb field is neglected throughout the electron propagation. The SMM describes the oscillation of an electron in the laser field abiding by Newton's equation of motion, and hence it can predict the maximum kinetic energy of an electron acquired from the oscillating electric field. In this work, the estimate of the cutoff with the SMM can help determine the spectral range in momentum spectra.

Firstly, we show the maximum kinetic energy acquired by a photoelectron in the "direct" ionization, i. e., the cutoff of ATI spectra. Given an electron "born" at t_r, the velocity of the electron is given by

$$\vec{v}^{(\text{before})}(t) = -\int_{t_r}^{t} \vec{E}(t')dt' = \vec{A}(t) - \vec{A}(t_r). \tag{39}$$

Here we assume the initial velocity $\vec{v}^{(\text{before})}(t_r) = 0$, where the superscript "(before)" denotes the status before any "hard" interaction between the photoelectron and its parent ion. As $t \to \infty$, the light field vanishes, $\vec{A}(\infty) \to 0$. Hence the asymptotic velocity $\vec{v}(\infty) = -\vec{A}(t_r)$. The maximum momentum is $|\vec{v}_{\max}| = |\vec{A}(t_r)| = E_0/\omega$, corresponding to the maximum kinetic energy

$$E_{\max} = \frac{1}{2}\left|\vec{v}_{max}\right|^2 = \frac{E_0^2}{2\omega^2} = 2U_p. \tag{40}$$

If rescattering processes are allowed, HATI may take place. By integrating (39), the trajectory before the rescattering is given by (we assume the tunnel exit, where the electron enters the continuum, is close to the origin, $\vec{r}(t_r) \simeq \vec{0}$)

$$\vec{r}^{(\text{before})}(t) = \vec{\alpha}(t) - \vec{\alpha}(t_r) - \vec{A}(t_r)\,(t - t_r)\,,$$

where $\vec{\alpha}(t)$ is the excursion of the electron as defined in (36). When the electron rescatters with its parent ion at t_{resc}, $\left|\vec{r}^{(\text{before})}(t_{\text{resc}})\right| = 0$, i. e.,

$$\left|\vec{\alpha}(t_{\text{resc}}) - \vec{\alpha}(t_r) - \vec{A}(t_r)\,(t_{\text{resc}} - t_r)\right| \sim 0. \tag{41}$$

Assuming a head-on collision with maximum momentum-transfer, from (39) the velocity instantly after the collision reads

$$\vec{v}^{(\text{after})}(t_{\text{resc}}) = -\left[\vec{A}(t_{\text{resc}}) - \vec{A}(t_r)\right], \tag{42}$$

where the reversed sign is due to the backward reflection. The subsequent velocity of the electron is obtained by solving the equation of motion with the initial condition (42),

$$\begin{aligned}\vec{v}^{(\text{after})}(t) &= -\int_{t_{\text{resc}}}^{t} \vec{E}(t')dt' + \vec{v}^{(\text{after})}(t_{\text{resc}}) \\ &= \vec{A}(t) - 2\vec{A}(t_{\text{resc}}) + \vec{A}(t_r).\end{aligned}$$

As $t \to \infty$, $\vec{A}(t) \to 0$, we have $\vec{v}^{(\text{after})}(\infty) = -2\vec{A}(t_{\text{resc}}) + \vec{A}(t_r)$. The maximum kinetic energy after the recollision cannot be determined analytically. Numerical evaluations indicate the photoelectron has the maximum kinetic energy [67],

$$E = \frac{1}{2}\left|-2\vec{A}(t_{\text{resc}}) + \vec{A}(t_r)\right|^2 < 10.007\, U_p. \tag{43}$$

In order to acquire the maximal return energy or backscattering energy, the electron has to start its orbit shortly after a maximum of the electric field strength. As a consequence, it returns or rescatters near a zero of the field.

3

IMAGINARY-TIME METHOD

When the intensity of the laser is sufficiently high, the light field substantially suppresses the binding potential and the bound electron can be emitted by tunneling through the distorted potential barrier. A narrow bundle of extremal trajectories that minimize the action functional can be used to account for the tunneling ionization in the semi-classical limit. Since the trajectories, as the most probable paths of electron tunneling, extend into the classical forbidden region, the time parameter is necessarily complex. In this chapter, the ITM technique concerning the non-relativistic strong field ionization is introduced (see [65] for a comprehensive review about the development of the ITM and more applications).

3.1 IMAGINARY TIME METHOD

The Hamiltonian for an atom in an external electric field $\vec{E}(t)$ is given by (11). In the length gauge, $\hat{W}(t) = \vec{r} \cdot \vec{E}(t)$, the TDSE reads

$$i\frac{\partial}{\partial t}|\psi(t)\rangle = \left[-\frac{1}{2}\nabla^2 + V(r) + \vec{r}\cdot\vec{E}(t)\right]|\psi(t)\rangle. \tag{44}$$

The integral form of (44) in the momentum space is [65]

$$\psi(\vec{p},t) = -i\int_{-\infty}^{t} dt' e^{iI_p t'} \int d^3\vec{r}' K(\vec{p},t;\vec{r}',t')V(\vec{r}')\varphi_0(\vec{r}'). \tag{45}$$

By applying the SPA, the coordinate representation of the kernel in the semi-classical limit is given by

$$K(\vec{r}t;\vec{r}'t') = \frac{\Theta(t-t')}{(2\pi i(t-t'))^{3/2}} e^{iS(\vec{r}t;\vec{r}'t')}. \tag{46}$$

Transforming (46) into the mixed representation using the Fourier transform, we find

$$K(\vec{p},t;\vec{r}',t') = \mathscr{F}\left[K(\vec{r}t;\vec{r}'t')\right] \simeq (2\pi)^{-3/2} e^{i[S(\vec{p},t;\vec{r}',t')-\vec{p}\cdot\vec{r}]}. \tag{47}$$

Substituting (47) into the wave function (45) and evaluating the action along the classical trajectory, $\psi(\vec{p},t)$ reads

$$\psi(\vec{p},t) = \frac{e^{iI_p t}}{(2\pi i)^{3/2}} \int_{-\infty}^{t} dt' \int d^3\vec{r}' e^{iW(\vec{p},t;\vec{p}',t')} V(\vec{r}')\varphi_0(\vec{r}'), \tag{48}$$

with the action

$$W(\vec{p},t;\vec{p}',t') = \int_{t'}^{t} \left(\mathcal{L}(\tau) - I_p\right) d\tau - \vec{p}\cdot\vec{r}. \tag{49}$$

Neglecting the binding potential, the Lagrangian $\mathcal{L}(\tau)$ is given by

$$\mathcal{L}_0(\tau) = \frac{\dot{\vec{r}}^2}{2} - \vec{r}\cdot\vec{E}(\tau). \tag{50}$$

Thus, the action (49) becomes

$$W_0 = \int_{t'}^{t} d\tau \left[\frac{\vec{v}^2(\tau)}{2} - \vec{r}\cdot\vec{E}(\tau) - I_p\right] - \vec{p}\cdot\vec{r}$$

with $-\vec{p}\cdot\vec{r}$ the upper boundary term for the integral $-\int_{t'}^{t} d\tau \frac{d}{d\tau}\left(\vec{v}(\tau)\cdot\vec{r}(\tau)\right)$ as long as $\vec{r}(t') = 0$ is assumed. With this substitution, the action

$$\begin{aligned} W_0 &= \int_{t'}^{t} d\tau \left[\frac{\vec{v}^2(\tau)}{2} + \vec{r}(\tau)\cdot\frac{d\vec{v}(\tau)}{dt} - I_p\right] - \int_{t'}^{t} d\tau \frac{d}{d\tau}\left(\vec{v}(\tau)\cdot\vec{r}(\tau)\right) \\ &= -\int_{t'}^{t} d\tau \left[\frac{\vec{v}^2(\tau)}{2} + I_p\right] = -\int_{t'}^{t} d\tau \left[\hat{\mathcal{H}}_0(\tau) + I_p\right] \end{aligned} \tag{51}$$

is obtained, where $\hat{\mathcal{H}}_0$ is the Hamiltonian for an electron in an external field. If the SPA is applied to the integral in Eq. (48), $dW/dt = 0$ leads to the SPA for the SFA in Eq. (35).

The major purpose of the ITM is to study the tunneling probability through a time-dependent potential barrier. In this chapter, we refer to the action W as the one in the sub-barrier region, $W \equiv W^{\text{sub}}$.

The minimized functional of the action determines that the trajectory of an electron satisfies the Euler-Lagrange equation, which are equivalent to Newton's equation of motion. In the following we introduce the complex trajectories used in this work.

3.2 COMPLEX TRAJECTORIES

The integration path $t = t_r + i\tau$ ($t_r \in \mathbb{R}$ and $\tau \in \mathbb{R}$ with the emission time t_r a constant) for the equations of motion in the complex-time plane, may be chose parallel to the imaginary-time axis. We assume t_r being a constant on the basis of the experimental evidence that, virtually, the measured tunneling delay time is zero [69].

Moreover, the following boundary conditions are imposed in accordance with the variation of W:

A. Spatially, the bound-state electron is located at the origin before the tunneling, $\text{Re}\vec{r}(t_s^{(\alpha)}) = \vec{0}$.

B. The initial kinetic energy equals the energy of the bound state, $\frac{1}{2}\vec{v}(t_s^{(\alpha)})^2 = -I_p$, in agreement with the SPE (35).

C. All dynamical variables are real after the electron has tunneled through the time-dependent potential barrier, $\text{Im}\vec{r}(t_r^{(\alpha)}) = \text{Im}\vec{v}(t_r^{(\alpha)}) = \vec{0}$. At $t = t_r$, $\vec{r}(t_r^{(\alpha)})$ is the tunnel exit.

In the absence of the Coulomb field (denoted by the subscript "o"), we choose the following complex trajectory which fulfills all the above assumptions,

$$\vec{r}_0(t) = \int_0^t \vec{A}(t')dt' + \vec{p}_0 t - \mathrm{Re}\left[\int_0^{t_s^{(\alpha)}} \vec{A}(t')dt' + \vec{p}_0 t_s^{(\alpha)}\right]. \tag{52}$$

Accordingly, the velocity is given by

$$\vec{v}_0(t) = \vec{p}_0 + \vec{A}(t). \tag{53}$$

3.3 IONIZATION PROBABILITY

The probability for a single trajectory to tunnel out of the potential barrier is given by

$$w = \left|M_p\right|^2 \sim \left|e^{iW}\right|^2 = \left|e^{i(\mathrm{Re}W + i\mathrm{Im}W)}\right|^2 = e^{-2\mathrm{Im}W}. \tag{54}$$

3.3.1 *Static Light Field*

As a first example, we use the ITM to derive the tunneling formula for the atomic ionization in a static field

$$E(t) = E_0, \qquad A(t) = -E_0 t. \tag{55}$$

Assuming that the z-axis is in the polarization direction, from Eq. (53) the sub-barrier velocity of the electron with the asymptotic momentum $\vec{p} = (p_z, p_x)$ is given by

$$v_z(t) \equiv v_z(t_r + i\tau) = (p_z - E_0 t_r) - iE_0\tau \tag{56}$$

$$v_x(t) \equiv v_x(t_r + i\tau) = p_x, \tag{57}$$

where τ is along the complex time path. At $t_s = t_r + it_i$, the boundary condition in Sec. 3.2 fulfills the SPE. Substituting (56) and (57) into (35) we find the components of t_s,

$$t_r = \frac{p_z}{E_0}, \qquad t_i = \frac{\sqrt{p_x^2 + 2I_p}}{E_0}. \tag{58}$$

Substituting (56) and (57) into the action (51) and using (58), the action reads

$$\begin{aligned} W &= -\int_{t_s}^{t_r} \left\{\frac{1}{2}\left[v_z^2(t) + v_x^2(t)\right] + I_p\right\} dt \\ &= i\int_0^{t_i} \left\{\frac{1}{2}\left[(-iE_0\tau)^2 + p_x^2\right] + I_p\right\} d\tau \\ &= i\left[\frac{1}{2}\left(p_x^2 + 2I_p\right)t_i - \frac{E_0^2}{6}t_i^3\right] \\ &= \frac{i}{3E_0}\left(p_x^2 + 2I_p\right)^{3/2}. \end{aligned}$$

Using (54), we find the tunneling formula [60]

$$\begin{aligned} w &\sim \exp\left[-\frac{2}{3E_0}\left(p_x^2+2I_p\right)^{3/2}\right] \\ &\simeq \exp\left[-\frac{2\kappa}{3E_0}\left(\kappa^2+\frac{3}{2}p_x^2\right)\right] \end{aligned} \tag{59}$$

with $\kappa=\sqrt{2I_p}$. The formula can be used to estimate the probability of ionization as a function of E_0 and the transverse momentum p_x.

3.3.2 *Arbitrary Light Field*

Let us consider an atom in a linearly polarized electric field $E(t)$, which can be decomposed into monochromatic components of frequencies $k\omega$ with $k\in\mathbb{N}$,

$$E(t)=E_0\sum_{k=1}^{\infty}f_k\cos(k\omega t),\qquad \sum_{k=1}^{\infty}f_k=1.$$

The vector potential reads

$$A(t)=-\frac{E_0}{\omega}\sum_{k=1}^{\infty}\frac{f_k}{k}\sin(k\omega t).$$

From Eq. (53) the components of velocity are given by

$$\begin{aligned} v_z(t) &= p_z-\frac{E_0}{\omega}\sum_{k=1}^{\infty}\frac{f_k}{k}\sin(k\omega t), \\ v_x(t) &= p_x. \end{aligned} \tag{60}$$

Inserting (60) into (51), we obtain the action for the sub-barrier propagation

$$\begin{aligned} W^{\text{sub}} &= -\int_{t_s}^{t_0}\left[\frac{1}{2}v(t)^2+I_p\right]dt \\ &= \left(\frac{1}{2}p^2+I_p\right)(t_s-t_r)+\frac{E_0p_z}{\omega^2}\sum_k\frac{f_k}{k^2}\left(\cos k\omega t_s-\cos k\omega t_r\right) \\ &+\frac{U_p}{\omega}\sum_k\sum_{k'}\frac{f_kf_{k'}}{kk'}\left[\frac{\sin\left[(k-k')\,\omega t\right]}{k-k'}-\frac{\sin\left[(k+k')\,\omega t\right]}{k+k'}\right]\Bigg|_{t_r}^{t_s}. \end{aligned} \tag{61}$$

The imaginary part of (61) is found as

$$\begin{aligned} \text{Im}W^{\text{sub}} &= \left(\frac{1}{2}p^2+I_p\right)t_i-\frac{E_0p_z}{\omega^2}\sum_k\frac{f_k}{k^2}\sin k\omega t_r\sinh k\omega t_i \\ &-\frac{U_p}{\omega}\sum_k\sum_{k'}\frac{f_kf_{k'}}{kk'}\left\{\frac{\cos\left[(k+k')\,\omega t_r\right]\sinh\left[(k+k')\,\omega t_i\right]}{k+k'}\right. \\ &\left.-\frac{\cos\left[(k-k')\,\omega t_r\right]\sinh\left[(k-k')\,\omega t_i\right]}{k-k'}\right\}. \end{aligned}$$

By decomposing the third term into two parts for indices $k = k'$ and $k > k'$, respectively,

$$-\frac{U_p}{\omega}\sum_k\sum_{k'} = -\frac{U_p}{\omega}\sum_k \frac{f_k^2}{k^2}\left(\frac{\cos 2k\omega t_r \sinh 2k\omega t_i}{2k} - \omega t_i\right) - \frac{2U_p}{\omega}\sum_{k'}\sum_{k>k'},$$

we are able to recover Eqs. (7) and (8) in Ref. [12],

$$\begin{aligned}\mathrm{Im}W^{\mathrm{sub}} = &\left(\frac{1}{2}p^2 + I_p + U_p\sum_k \frac{f_k^2}{k^2}\right)t_i - \frac{E_0 p_z}{\omega^2}\sum_k \frac{f_k}{k^2}\sin k\omega t_r \sinh k\omega t_i \\ &- \frac{U_p}{2\omega}\sum_k \frac{f_k^2}{k^3}\cos 2k\omega t_r \sinh 2k\omega t_i \\ &- \frac{2U_p}{\omega}\sum_{k'}\sum_{k>k'}\left[\frac{f_k f_{k'}}{kk'}\frac{\cos\left(k+k'\right)\omega t_r \sinh\left(k+k'\right)\omega t_i}{k+k'}\right. \\ &\left.- \frac{\cos\left(k-k'\right)\omega t_r \sinh\left(k-k'\right)\omega t_i}{k-k'}\right]\end{aligned}$$

and derive the ionization probability using Eq. (54). The formulas in [12] were derived under the assumption that the electron enters the continuum at the peak of the electric field, $t_r = 0$, and the corresponding momentum $\vec{p} = 0$. In the above derivation, however, trajectories are allowed to take any asymptotic momentum $\vec{p}$, and saddle points t_s are $\vec{p}$-dependent. This extension allows for the full range of classical trajectories of all possible $\vec{p}$. Therefore the ITM is not restricted to the evaluation of the ionization probability from just one extremal trajectory. Instead, it may be extended to account for all trajectories with arbitrary sampling momenta and provides the possibility to study problems which require more than on trajectory, such as interference phenomena.

3.4 COULOMB CORRECTION TO THE IONIZATION PROBABILITY

In a neutral atomic system, the asymptotic wave function is given by (see Sec. A.1)

$$\psi_{\mathrm{at}}(r) = (\kappa r)^{n_*} e^{-\kappa r} = e^{n_* \ln(\kappa r) - \kappa r} \equiv e^{iS_{\mathrm{at}}},$$

where $n_* = Z/\kappa$ is often referred to as the effective principle quantum number, and the atomic action is defined as

$$S_{\mathrm{at}} = i\kappa r - i n_* \ln\left(\kappa r\right). \tag{62}$$

If the Coulomb potential is present, the action due to the Coulomb interaction is perturbatively given by

$$S_c = \int_{t_s}^{t_r} V\left[r_0(t)\right] dt, \tag{63}$$

where the Coulomb effect is evaluated along the unperturbed trajectory $r_0(t)$. For convenience sake, defining the complex phase $\phi = \omega t$, the action (63) reads

$$S_c = \int_{t_s}^{t_r} \left[-\frac{Z}{r_0(t)} \right] dt = -\frac{Z}{\omega} \int_{\phi_s}^{\phi_r} \frac{d\phi}{r_0(\phi)}. \tag{64}$$

Evaluating the integral along the complex path $\phi = \phi_r + i\varphi$ with the variable of integration φ, Eq. (64) becomes

$$S_c = i\frac{Z}{\omega} \int_0^{\phi_i} \frac{d\varphi}{r_0(\phi_r + i\varphi)} = in_* \int_0^{\phi_i} \frac{d\varphi}{\xi_0(\varphi)}, \tag{65}$$

with $\phi_i = \mathrm{Im}\phi_s$, and $\xi_0(\varphi) = (\omega/\kappa)\, r_0(t(\varphi))$ the dimensionless trajectory.

3.4.1 *Sub-Barrier Trajectory*

With the boundary condition $\vec{r}_0(t_s) = 0$, the trajectory is given by

$$\vec{r}_0(\phi) = \frac{\vec{p}}{\omega} (\phi - \phi_s) + \frac{1}{\omega} \int_{\phi_s}^{\phi} \vec{A}(\phi') d\phi'. \tag{66}$$

Near the saddle point, $\phi \to \phi_s$, we expand

$$\begin{aligned} \vec{r}_0(\phi) &\simeq \frac{\vec{p}}{\omega} (\phi - \phi_s) + \frac{1}{\omega} \vec{A}(\phi_s) (\phi - \phi_s) \\ &= \frac{1}{\omega} \left[\vec{p} + \vec{A}(\phi_s) \right] (\phi - \phi_s). \end{aligned} \tag{67}$$

Substituting the relation from the SPE (35), $\left[\vec{p} + \vec{A}(\phi_s) \right]^2 = -\kappa^2$, into (67), we obtain the sub-barrier trajectory,

$$r_0(\varphi) = \pm \frac{\kappa}{\omega} (\phi_i - \varphi),$$

or the dimensionless trajectory ξ_0,

$$\xi_0(\varphi) = \frac{\omega}{\kappa} r_0(\varphi) = \pm (\phi_i - \varphi). \tag{68}$$

3.4.2 *Matching Procedure*

The integrand in Eq. (65) is divergent at $\varphi = \phi_i$. The difficulty due to the singularity can be circumvented using the matching procedure. Let ϕ_* be a point adjacent to the singularity,

$$\lim_{\phi_* \to \phi_i} \int_0^{\phi_*} \frac{d\varphi}{\xi_0(\varphi)} = \int_0^{\phi_i} \frac{d\varphi}{\xi_0(\varphi)}.$$

If a matching point ϕ_1 which is close to ϕ_* and satisfies the conditions $\phi_1 < \phi_*$ and $\phi_* - \phi_1 \ll 1$ exists, the trajectory for $\phi_1 < \varphi < \phi_*$ can be approximated by Eq. (68). Thus, Eq. (65) is split into two parts,

$$S_c = in_* \left[\int_0^{\phi_1} \frac{d\varphi}{\xi_0(\varphi)} + \int_{\phi_1}^{\phi_*} \frac{d\varphi}{\xi_0(\varphi)} \right], \tag{69}$$

and by using Eq. (68) the integrand of the second term is given by

$$\begin{aligned}\int_{\phi_1}^{\phi_*} \frac{d\varphi}{\xi_0(\varphi)} = \int_{\phi_1}^{\phi_*} \frac{d\varphi}{\phi_i - \varphi} &= -\ln(\phi_i - \varphi)\big|_{\phi_1}^{\phi_*} \\ &= \ln(\phi_i - \phi_1) - \ln(\phi_i - \phi_*)\,.\end{aligned}$$

Applying the approximation $\phi_i - \phi_* \simeq \frac{\omega}{\kappa} r_0(\phi_*)$ near ϕ_i to the last term, the action (69) becomes

$$\begin{aligned}S_c &= in_* \left[\int_0^{\phi_1} \frac{d\varphi}{\xi_0(\varphi)} + \ln(\phi_i - \phi_1) - \ln\frac{\omega}{\kappa} r_0(\phi_*)\right] \\ &= in_* \left[\int_0^{\phi_1} \frac{d\varphi}{\xi_0(\varphi)} + \ln(\phi_i - \phi_1) - \ln\frac{\omega}{\kappa^2} - \ln\kappa r_0(\phi_*)\right]. \quad (70)\end{aligned}$$

Though the last term is divergent as $\phi_* \to \phi_i$, it matches the second term of the asymptotic wave function (62). Thus, the regularized action $S_c^{(R)}$, i. e., the part of the action corresponding to the long-range Coulomb potential, is given by

$$\begin{aligned}S_c^{(R)} &= S_c + \ln\kappa r_0(\phi_*) \\ &= \lim_{\phi_* \to \phi_i} in_* \left[\int_0^{\phi_*} \frac{d\varphi}{\xi_0(\varphi)} + \ln\kappa r_0(\phi_*)\right] \\ &= \lim_{\phi_* \to \phi_i} in_* \left[\int_0^{\phi_*} \frac{d\varphi}{\xi_0(\varphi)} + \ln\frac{\kappa^2}{\omega} - \int_0^{\phi_*} \frac{d\varphi}{\phi_i - \varphi} + \ln\phi_i\right] \\ &= \lim_{\phi_* \to \phi_i} in_* \left[\ln\left(\frac{\kappa^2\phi_i}{\omega}\right) + \int_0^{\phi_*} \left[\frac{1}{\xi_0(\varphi)} - \frac{1}{\phi_i - \varphi}\right] d\varphi\right] \\ &= in_* \left[\ln\left(\frac{\kappa^2\phi_i}{\omega}\right) + \int_0^{\phi_i} \left[\frac{1}{\xi_0(\varphi)} - \frac{1}{\phi_i - \varphi}\right] d\varphi\right]. \quad (71)\end{aligned}$$

Similarly, the Coulomb correction to the ionization rate is obtained by substituting (71) into (54). For a constant field in the form of (55), the correction to the ionization probability induced by the sub-barrier Coulomb interaction is given by a prefactor $Q = \left(2\kappa^3/E_0\right)^{2n_*}$ [12].

4

TRAJECTORY-BASED COULOMB CORRECTED STRONG FIELD APPROXIMATION

Although the SFA facilitates the study of non-perturbative ionization processes in strong field physics, considerable deviations are found between the SFA and *ab initio* results. The disagreements are largely due to the lack of proper descriptions of the Coulomb interaction between the emitted electron and its parent ion. In this chapter, the TCSFA method is presented on the basis of the SFA. The aim of the TCSFA is to cure inherent shortcomings in the SFA by taking the Coulomb interaction into consideration, while retaining the advantage of the SFA being simple and intuitive using the concept of quantum orbits.

4.1 TRAJECTORY-BASED COULOMB CORRECTION

In order to distinguish physical quantities before and after applying the Coulomb-correction, we use the subscript "0" to indicate "unperturbed" variables in the absence of the Coulomb potential, such as trajectories in the plain SFA.

Given a final momentum $\vec{p}$, the action (27) as a function of the αth saddle point $t_s^{(\alpha)} \equiv t_s^{(\alpha)}(\vec{p})$ is recast into [70]

$$S_{I_p,\vec{p}}(t_{s0}^{(\alpha)}) = C(\vec{p}) - \int_{t_{s0}^{(\alpha)}}^{\infty} \left[\frac{1}{2}\vec{v}_0^2(t) + I_p\right] dt, \tag{72}$$

where $\vec{v}_0(t) = \vec{p} + \vec{A}(t)$ is the velocity of an electron subjected to the light field of the vector potential $\vec{A}(t)$. $C(\vec{p}) = \int_0^{\infty} \left[\frac{1}{2}\vec{v}_0^2(t) + I_p\right] dt$, varies with different asymptotic momenta $\vec{p}$, while it does not depend on the saddle point $t_{s0}^{(\alpha)}$. Hence, $C(\vec{p})$ can be factored-out of the summation (34) and thus does not affect the ionization probability. The integrand in (72), $H_0(t) \equiv \frac{1}{2}\vec{v}_0^2(t)$, is the Hamiltonian of a free electron in an electromagnetic field. The action (72) reads

$$S_{I_p,\vec{p}}(t_{s0}^{(\alpha)}) = C(\vec{p}) - \int_{t_{s0}^{(\alpha)}}^{\infty} \left[H_0(t) + I_p\right] dt. \tag{73}$$

Switching-on the binding potential, since the motion of the electron is influenced by the Coulomb force, the trajectory is distorted,

$$\vec{r}_0 \to \vec{r}, \qquad \vec{v}_0 \to \vec{v}. \tag{74}$$

Moreover, the potential in the Hamiltonian of the action (73) includes the Coulomb interaction between the electron and the parent ion [71],

$$H_0 \to H = H_0 + U_{\text{Coulomb}} = H_0 - \frac{Z}{|\vec{r}(t)|}. \tag{75}$$

Using (74) and (75) to reformulate the transition amplitude (73), the TCSFA transition amplitude thus reads

$$\begin{aligned} M_{\vec{p}}^{(0)} &\sim e^{iC(\vec{p})} \sum_{\alpha} \frac{\exp\left[-i\int_{t_s^{(\alpha)}}^{\infty}\left(\frac{1}{2}\vec{v}^2(t) - \frac{Z}{|\vec{r}(t)|} + I_p\right)dt\right]}{S''(t_s^{(\alpha)})} \\ &\equiv e^{iC(\vec{p})} \sum_{\alpha} M_{\vec{p}}(t_s^{(\alpha)}), \end{aligned} \tag{76}$$

where

$$\begin{aligned} M_{\vec{p}}(t_s^{(\alpha)}) &= \left[S''(t_s^{(\alpha)})\right]^{-1} \exp\left[iW(t_s^{(\alpha)})\right] \\ &\equiv \mathcal{P}(t_s^{(\alpha)}) \exp\left[iW(t_s^{(\alpha)})\right] \end{aligned} \tag{77}$$

is the single-trajectory transition amplitude for ionization, and $W(t_s^{(\alpha)})$ is the action,

$$W \equiv W(t_s^{(\alpha)}) = -\int_{t_s^{(\alpha)}}^{\infty}\left[\frac{1}{2}\vec{v}^2(t) - \frac{Z}{|\vec{r}(t)|} + I_p\right]dt. \tag{78}$$

The above derivation is rigorous for the H(1s) state, while the prefactor $\mathcal{P}(t_s^{(\alpha)})$ may vary if excited states are involved.

The action (78) can be split into two parts,

$$W = W^{\text{sub}} + W^{\text{re}}, \tag{79}$$

where

$$W^{\text{sub}} = -\int_{t_s^{(\alpha)}}^{t_r^{(\alpha)}}\left[\frac{1}{2}\vec{v}^2(t) - \frac{Z}{\sqrt{\vec{r}^2(t)}} + I_p\right]dt \tag{80}$$

is the action for the sub-barrier propagation (here we write on purpose $Z/\sqrt{\vec{r}^2(t)}$ instead of the non-analytic $Z/|\vec{r}(t)|$), and

$$W^{\text{re}} = -\int_{t_r^{(\alpha)}}^{\infty}\left[\frac{1}{2}\vec{v}^2(t) - \frac{Z}{|\vec{r}(t)|} + I_p\right]dt \tag{81}$$

is the action for the real-time propagation. The incorporation of Coulomb interaction into W^{re} and W^{sub} introduces different influences on photoelectron momentum distributions.

The evaluation of W^{re} with the Coulomb interaction is straightforward, since we only need to solve ordinary differential equations (ODEs) for real trajectories. However, the incorporation of Coulomb effects into the sub-barrier action W_{sub} is usually nontrivial because of the extra dimensions involved for complex variables. For practical convenience, we split the sub-barrier Coulomb action

$$W^{\text{sub}} = W^{\text{sub,0}} + W^{\text{subcc}}, \tag{82}$$

into the sub-barrier part for the plain SFA

$$W^{\text{sub,0}} = -\int_{t_s}^{t_r}\left[\frac{1}{2}\vec{v}^2(t) + I_p\right]dt \tag{83}$$

and the action for the sub-barrier Coulomb correction (sub-CC)

$$W^{\text{subcc}} = \int_{t_s}^{t_r} \frac{Z}{\sqrt{\vec{r}^2(t)}} dt. \tag{84}$$

For simplicity's sake, the distortion of trajectories due to the Coulomb interaction is neglected for the sub-barrier propagation, thus $\vec{r}(t) = \vec{r}_0(t)$ and $\vec{v}(t) = \vec{v}_0(t)$. The influence of W^{subcc} is not considered in the following discussions except in Sec. 5.2 where we explicitly study sub-CC effects.

4.2 NUMERICAL IMPLEMENTATION

The transition amplitude (76) of the TCSFA resembles (34) of the SFA except for an extra term describing the Coulomb interaction. Nevertheless, the TCSFA requires explicit evaluations of trajectories. In the following the implementation of the TCSFA is introduced.

We focus on the atomic ionization in a linearly polarized laser field and investigate photoelectron momentum spectra. Because of the azimuthal symmetry about the polarization axis, it is sufficient to consider the motion of the photoelectron in a two-dimensional space parallel and perpendicular to the polarization direction. We study the doubly-differential momentum distribution $\left|M_{\vec{p}}\right|^2$ as a function of $\vec{p} = (p_\parallel, p_\perp)$, that is, for example, along $p_\parallel \equiv p_z$ and $p_\perp \equiv p_x$, respectively.

Our implementation of the TCSFA consists of two stages. In the first stage, we calculate millions of independent trajectories and record their information in a database. In the second stage, we post-process the database and calculate the momentum spectra.

In the first stage, the steps to evaluate the transition matrix element (77) for a single trajectory are as follows:

A. Generate a random seed $\vec{p}_0 = (p_{z0}, p_{x0})$ as an initial momentum within $[-p_{z0}^{\max}, p_{z0}^{\max}] \times [0, p_{x0}^{\max}]$. The seeds are uniformly distributed. Note we have neglected $\vec{p}_0$ of $p_{x0} < 0$, because trajectories starting with initial momenta (p_{z0}, p_{x0}) and $(p_{z0}, -p_{x0})$ are always symmetrical due to the axial symmetry along the polarization direction, whether the Coulomb potential is included or not.

B. Given the initial momentum $\vec{p}_0$, we solve the SPE (35)

$$\frac{1}{2}\left[\vec{p}_0 + \vec{A}(t_s^{(\alpha)})\right]^2 = -I_p \tag{85}$$

to acquire the αth solution $t_s^{(\alpha)}$ using a complex root-finding routine [72]. Most numerical root-finding routines need a seed $t_{\text{guess}}^{(\alpha)}$ to begin with. We need to choose $t_{\text{guess}}^{(\alpha)}$ with care, since

generally there are several solutions to the SPE (85). We need a set of estimated values $\{t_{\text{guess}}^{(\alpha)}\}$ for all valid solutions, at least the most important ones, and each element of $\{t_{\text{guess}}^{(\alpha)}\}$ should correspond uniquely to an exact solution. In practice, we use a graphical method to find the set $\{t_{\text{guess}}^{(\alpha)}\}$. Given the initial momentum $\vec{p}_0$, we calculate a target function $f(i,j)$ on the two-dimensional grid representing the discrete complex time $t_{\text{guess}}(i,j) = \text{Re}t_{\text{guess}}(i) + i\text{Im}t_{\text{guess}}(j)$,

$$f(i,j) = \left| \frac{1}{2}\left[\vec{p}_0 + \vec{A}(t_{\text{guess}}(i,j))\right]^2 + I_p \right|. \tag{86}$$

By finding the local minima of $f(i,j)$, whose indices are denoted by (i',j'), we obtain $\{(i',j')\}$, and the set for the estimated saddle points is thus given by $\{t_{\text{guess}}^{(\alpha)}\} = \{t_{\text{guess}}(i,j)|(i,j) \in \{(i',j')\}\}$.

C. Calculate trajectories for the sub-barrier propagation and the action W^{sub} in (82). Details are presented in Sec. 4.2.1. At $t = t_r^{(\alpha)}$, the complex trajectories become real and the values specify the initial conditions $\vec{r}(t_r^{(\alpha)})$ and $d\vec{r}(t)/dt|_{t=t_r^{(\alpha)}}$ for the real-time propagation of the next step.

D. We integrate along the real-time axis by solving the ODEs of motion from the tunnel exit (defined in Sec. 3.2), in the presence of both the laser and Coulomb fields, until the laser is switched off at $t = T_p$. Details of the numerical implementation are presented in Sec. 4.2.2. At each time step, the action W^{re} (81) is evaluated simultaneously. At $t = T_p$, variables $\vec{r}(T_p)$ and $d\vec{r}(t)/dt|_{t=T_p}$ are recorded to calculate the asymptotic momentum in the next step.

E. After the laser is switched off, we calculate the asymptotic momentum $\vec{p}$ using Kepler's formula [28] as shown in Sec. 4.2.3.

F. Calculate W in Eq. (79). From Eq. (77), evaluate the single-trajectory transition amplitude $M_{\vec{p}}(t_s^{(\alpha)})$.

The above procedure describes how a single trajectory is evaluated in the first stage. In order to attain momentum spectra with good statistics we need a large number of initial momenta $\vec{p}_0$ and perform the above procedure repeatedly. The method is straightforward for parallelization thanks to the independence of trajectories in the current single-electron system. In practice, we partition the set of $\vec{p}_0$, which are randomly and uniformly generated, and distribute subdivided sets onto multiple computational nodes. Each $\vec{p}_0$ corresponds to several $t_s^{(\alpha)}$ after solving the SPE, and each $t_s^{(\alpha)}$ determines a single trajectory of the asymptotic momentum $\vec{p}$ (in SFA, $\vec{p} = \vec{p}_0$; in TCSFA,

generally $\vec{p} \neq \vec{p}_0$) and the transition matrix element $M_{\vec{p}}(t_s^{(\alpha)})$. All information of trajectories can be stored in a dataset for the further analysis.

In the second stage, we post-process the dataset and calculate the doubly-differential momentum distribution on a grid representing the final momentum. Looping over all trajectories, the ionization probability for the bin of a certain momentum $\tilde{\vec{p}}$ is given by

$$\left|M_{\tilde{\vec{p}}}\right|^2 = \left|\sum_i M_{\vec{p}}^{(i)}(t_s^{(\alpha)})\right|^2, \tag{87}$$

where i is the index of the trajectory whose $\vec{p}$ falls into the bin centered at $\tilde{\vec{p}}$ with the transition amplitude $M_{\vec{p}}^{(i)}(t_s^{(\alpha)})$.

4.2.1 *Complex Trajectories for Sub-Barrier Propagation*

With the complex trajectories introduced in Sec. 3.2 on the basis of the ITM for the tunneling process, we calculate the action W^{sub} by substituting (52) and (53) into (82), (83) and (84). The integrals in W^{sub} are evaluated by numerical integrations.

Though we have introduced W^{subcc} in Eq. (84), the term is neglected in the following discussions except for the explicit investigation into the sub-CC effect in Sec. 5.2. Note (84) may diverge if the complex trajectory $\vec{r}(t) = \vec{0}$. However, thanks to the negligible occurrence of such trajectories, we rarely encounter singularities in the numerical implementation of the sub-CC, and spectra are not influenced.

4.2.2 *Numerical Evaluation of Trajectories for Real-Time Propagation*

The motion of the electron in the real-time propagation is determined by systems of ODEs. In this work, we use the classical fourth-order Runge-Kutta method (RK4) to solve ODEs (see Sec. A.3). In order to retain a high computational efficiency, the RK4 routine dynamically adjusts the time step h. Most of the time the electron is far away from the parent ion, hence the trajectories are usually smooth and a relatively large h is adequate to achieve the desired numerical precision. However, when the electron approaches the ion, h decreases and the computational efficiency drops dramatically, because systems of ODEs are highly singular near the Coulomb center. In order to avoid such an efficiency loss, we can either discard trajectories which are excessively close to the parent ion, or treat trajectories with the recipe as shown in Sec. 4.2.4.

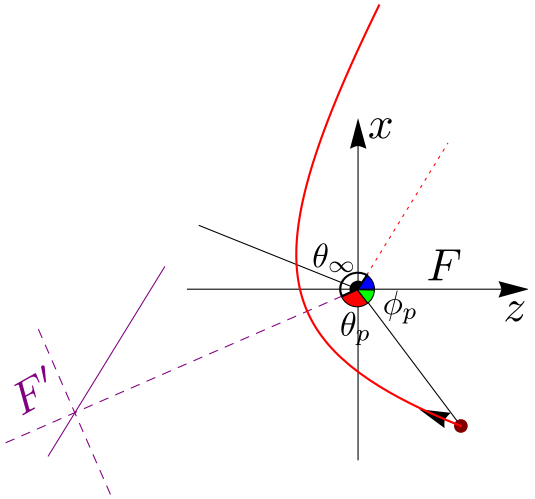

Figure 1: The Kepler orbit of a photoelectron in the Coulomb field for $t > T_p$. At $t = T_p$, the photoelectron is indicated by the red point with the initial position $\vec{r}_p \equiv \vec{r}(T_p)$ and the initial velocity $\vec{v}_p \equiv \vec{v}(T_p)$. The default coordinate system F (black solid frame), the new coordinate system F' (purple dashed frame) in which the formula of Kepler's orbits applies, and the direction of the asymptotic momentum (red dotted line) are shown. Parameters are $\vec{r}_p = (2.03, -2.70)$, $\vec{v}_p = (-0.8259, 0.3312)$ and the charge $Z = 1$.

4.2.3 *Propagation after Switching-Off the Laser Pulse*

If the light field is switched off at $t = T_p$, the asymptotic momentum of the free electron, $\vec{p}(\infty)$, equals the kinetic momentum $\vec{p}(T_p)$. In the TCSFA, since the long-range Coulomb force acts on the electron, the acceleration continues changing and hence $\vec{p}(\infty) \neq \vec{p}(T_p)$. The distortion of trajectories also influences the action (81) for the interval $t > T_p$ of the integration.

The system without the laser field can be studied as a classical two-body problem (see Sec. A.4) without numerical evaluations of trajectories. Given the position $\vec{r}_p \equiv \vec{r}(T_p)$ and the velocity $\vec{v}_p \equiv \vec{v}(T_p)$ at $t = T_p$, we can analytically derive $\vec{p}(\infty)$ and (81) for the interval $[T_p, \infty]$ using Kepler's formula.

4.2.3.1 *Coordinate Transformation*

If the electron arrives at the detector, $|\vec{r}(\infty)| \to \infty$, the trajectory requires to be an open orbit with a positive total energy. In a two-body system, the open orbit is described by a branch of hyperbola with its focus located at the Coulomb center. Before determining the hyperbola, we should first ensure that the total energy of the photoelectron $E = \vec{v}_p^2/2 - Z/|\vec{r}_p| > 0$. Otherwise the trajectory does not contribute to the photoelectron spectrum.

In Sec. A.4, Eq. (171) describes the Kepler orbit in a specified reference coordinate system F'. In Eq. (171), r is the distance between

the Coulomb center and the electron, and θ is the angle with the vertex at the core from the perigee. In order to use Eq. (171), we need to transform between F' and the coordinate system F we use in the simulation. As is illustrated in Fig. 1, in the coordinate system F, the origin is the location of the Coulomb center, and the z-axis is determined by the polarization direction. In the coordinate system F', the hyperbola has the standard form, that is, the Coulomb center is one focus of the hyperbola, and the major axis of the hyperbola is along the z'-axis.

The relation between coordinate systems F and F' depends on $\vec{r}_p$ and $\vec{v}_p$. Substituting $r_p = |\vec{r}_p|$ into Eq. (171), we have the angle $\theta_p \equiv \theta(T_p)$,

$$\cos\theta_p = \frac{k - r_p}{r_p \epsilon} = \frac{\frac{l^2}{Z r_p} - 1}{\epsilon}, \tag{88}$$

where the angular momentum l and the eccentricity ϵ are introduced in Sec. A.4. Taking the sign of θ_p, i. e., the rotation direction, into account, we have

$$\theta_p = \begin{cases} 2k\pi + \arccos(\frac{k-r_p}{r_p\epsilon}), & (\vec{r}_p \cdot \vec{v}_p)\, l \geq 0, \\ 2k\pi - \arccos(\frac{k-r_p}{r_p\epsilon}), & (\vec{r}_p \cdot \vec{v}_p)\, l < 0, \end{cases} \tag{89}$$

as shown in Fig. 1 (red angle). Now let us define ϕ_p as the angle with the vertex at the Coulomb center from the z-axis in F (green angle in Fig. 1). From Fig. 1, the angle of rotation from the z-axis to the z'-axis is given by

$$\gamma = \phi_p - \theta_p. \tag{90}$$

4.2.3.2 *Field-Free Asymptotic Momentum*

Substituting $r \to \infty$ into the Kepler orbit (171), the asymptotic angle (indicated by a bold arc in Fig. 1) in F' is given by

$$\theta_\infty = \arccos\left(-\frac{1}{\epsilon}\right). \tag{91}$$

With the aid of the energy conservation law (170), the asymptotic momentum in F is derived by the rotation,

$$\vec{p} \equiv (p_z, p_x) = \left(p\cos\left(\theta_\infty + \gamma\right), p\sin\left(\theta_\infty + \gamma\right)\right), \tag{92}$$

where $p = |p_0|$ is the total momentum.

4.2.4 *Near-Nucleus Trajectory*

When the electron enters the defined circle centered at the core with the small radius r_{thresh}, the interaction between the electron and the Coulomb center dominates. We can either neglect these trajectories

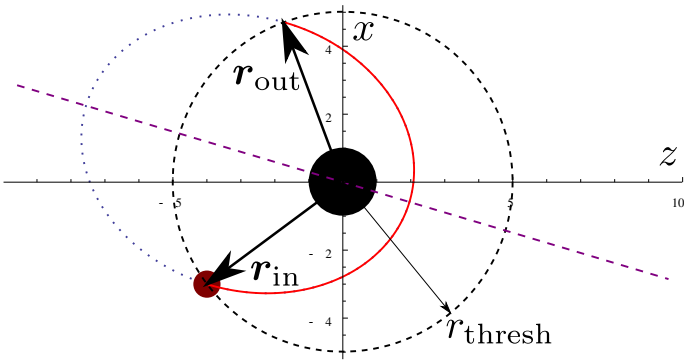

Figure 2: Neglecting the external light field, the Kepler orbit of a near-core photoelectron in the Coulomb field. At $t = T_p$, the photoelectron is indicated by the orange point with the initial position $\vec{r}_{\rm in} \equiv \vec{r}(t_{\rm in})$ and the initial velocity $\vec{v}_{\rm in} \equiv \vec{v}(t_{\rm in})$. The default coordinate system F (black solid frame), the new coordinate system F' (purple dashed frame) in which the formula of Kepler's orbits applies.

because of their small weights, or analytically connect trajectories by neglecting the influence of the external light field during such close encounters. The latter method uses Kepler's theory as described above. As is demonstrated in Fig. 2, at $t = t_{\rm in}$ when the electron enters the circle at the initial position $\vec{r}_{\rm in}$ ($|\vec{r}_{\rm in}| = r_{\rm threshold}$) and the velocity $\vec{v}_{\rm in}$, the angle in F' for (171) is $\theta_{\rm in} = \theta_0$. When the electron moves out of the circle at $t = t_{\rm out}$, the angle is $\theta_{\rm out} = -\theta_0$, and the "exit" $\vec{r}_{\rm out}$ is calculated by the coordinates transformation.

4.2.4.1 *Time at "Exit": $t_{\rm out}$*

We can find the relation between the angle θ and the time t from the angular momentum $l = r^2\dot{\theta}$, where l is conserved. Applying the integration on both sides of $dt = (r^2/l)d\theta$ and substituting r with the Kepler orbit (171),

$$t_{\rm out} - t_{\rm in} = \frac{k^2}{l}\int_{\theta_0}^{-\theta_0} \frac{d\theta}{(1+\epsilon\cos\theta)^2},$$

the time when the electron moves out of the defined region reads

$$t_{\rm out} = t_{\rm in} + \frac{2k^2}{l}\left\{\frac{2\,\text{arctanh}\left(\frac{\epsilon-1}{\sqrt{\epsilon^2-1}}\tan\frac{\theta_0}{2}\right)}{(\epsilon^2-1)^{3/2}} - \frac{\epsilon\sin\theta_0}{(\epsilon^2-1)\,(1+\epsilon\cos\theta_0)}\right\}.$$

The above formula is applicable for any type of Kepler orbitals. For a hyperbola,

$$t_{\rm out} = t_{\rm in} + \frac{2k^2}{l}\left\{\frac{\log\left[\frac{\sqrt{\epsilon^2-1}+(\epsilon-1)\tan(\theta_0/2)}{\sqrt{\epsilon^2-1}-(\epsilon-1)\tan(\theta_0/2)}\right]}{(\epsilon^2-1)^{3/2}} - \frac{\epsilon\sin\theta_0}{(\epsilon^2-1)(1+\epsilon\cos\theta)}\right\}.$$

4.2.4.2 *Position at "Exit": $\vec{r}_{\text{out}}$*

When the electron exits the circle at $t = t_{\text{out}}$, the boundary conditions,

$$|\vec{r}_{\text{out}}| = r_{\text{thresh}}, \quad \theta_{\text{out}} = -\theta_0,$$

are satisfied. Correspondingly, in the coordinate system F for our calculation, the "exit" on the defined circle is found by the transformation,

$$\vec{r} = r_{\text{thresh}} \left(\cos\left(\gamma - \theta_0\right), \sin\left(\gamma - \theta_0\right)\right) \quad ,$$

where the angle between the major-axis for the Kepler formula and the z-axis of the our coordinate system is given by $\gamma = \phi_0 - \theta_0$, similar to Eq. (90).

4.2.4.3 *Velocity at "Exit": $\vec{v}_{\text{out}}$*

Because of the symmetry $|\vec{v}_{\text{out}}| = |\vec{v}_{\text{in}}|$ in the coordinate system F', the particle enters with the angle θ_v and exits with $\pi - \theta_v$. In the two-dimensional system, we need to use the rotation matrix

$$\hat{R}(\gamma) = \begin{pmatrix} \cos\gamma & -\sin\gamma \\ \sin\gamma & \cos\gamma \end{pmatrix}$$

for the transformation from F to F'. The velocity of incidence in F' is $(v'_z, v'_x) = \hat{R}(-\gamma)(v_z, v_x)$. Therefore the angle of incidence is given by

$$\theta'_{\text{in}} = \begin{cases} \arccos \frac{v'_z}{\sqrt{v'^2_z + v'^2_x}}, & v_x \geq 0, \\ -\arccos \frac{v'_z}{\sqrt{v'^2_z + v'^2_x}} & v_x < 0. \end{cases}$$

Correspondingly, thanks to the symmetry, we have the angle for the "exit" in F', $\theta'_{\text{out}} = \pi - \theta'_{\text{in}}$. Transforming back to the coordinate system F, the angle of the velocity vector reads $\theta_{\text{out}} = \theta'_{\text{out}} + \gamma$, and the velocity is $\vec{v}_{\text{out}} = |\vec{v}_{\text{in}}|(\cos\theta_{\text{out}}, \sin\theta_{\text{out}})$.

4.2.4.4 *Action within the Circle: W^{circle}*

The action for the propagation in the circle can be evaluated analytically,

$$W^{\text{circle}} = \int_{t_{\text{in}}}^{t_{\text{out}}} \left(\frac{1}{2}\vec{v}^2 - \frac{Z}{|\vec{r}|} + I_p\right) dt. \tag{93}$$

First, we calculate $\vec{v}^2$ in the integrand of (93). The radial velocity is given by

$$\dot{r} = \frac{dr}{dt} = \frac{d}{dt}\left(\frac{k}{1 + \epsilon\cos\theta}\right) = -\frac{\epsilon k \sin\theta}{(1 + \epsilon\cos\theta)^2}\dot{\theta}. \tag{94}$$

Substituting the angular velocity

$$\dot{\theta} = \frac{l}{r^2} = \frac{l}{k^2}(1 + \epsilon\cos\theta)^2 \tag{95}$$

into (94), the radial velocity reads

$$\dot{r} = -\frac{\epsilon l \sin\theta}{k}. \tag{96}$$

Since the vector of the velocity is given by $\vec{v} = \dot{\vec{r}} = \dot{r}\vec{e}_r + r\dot{\theta}\vec{e}_\theta$, together with (95) and (96), we obtain the kinetic energy in (94)

$$\frac{1}{2}\vec{v}^2 = \frac{l^2}{2k^2}(\epsilon^2 + 1 + 2\epsilon\cos\theta). \tag{97}$$

Defining the integrand in (93) as $g(\theta)$, we rewrite W^{cirlce},

$$W^{\text{cirlce}} = \int_{t_{\text{in}}}^{t_{\text{out}}} g(\theta)dt = \int_{t_{\text{in}}}^{t_{\text{out}}} g(\theta)\frac{dt}{d\theta}d\theta = \int_{\theta_0}^{-\theta_0} \frac{g(\theta)}{\dot{\theta}}d\theta. \tag{98}$$

Using (97), the new integrand of (98) is given by

$$\begin{aligned}\frac{g(\theta)}{\dot{\theta}} &= \frac{1}{\dot{\theta}}\left(\frac{1}{2}\vec{v}^2 - \frac{Z}{r} + I_p\right) \\ &= \frac{k^2}{l\left(1+\epsilon\cos\theta\right)^2}\left[\frac{l^2}{2k^2}\left(\epsilon^2 + 1 + 2\epsilon\cos\theta\right) - \frac{Z\left(1+\epsilon\cos\theta\right)}{k} + I_p\right].\end{aligned}$$

Integrating (98) analytically, we obtain

$$\begin{aligned}W^{\text{circle}} \quad = \quad & \frac{2k^2}{l}\Bigg\{\frac{2\left[a + I_p - a\epsilon^2 + b\left(\epsilon^2-1\right)\right]\operatorname{arctanh}\left[\frac{\epsilon-1}{\sqrt{\epsilon^2-1}}\tan\frac{\theta_0}{2}\right]}{\left(\epsilon^2-1\right)^{3/2}} \\ & -\frac{\epsilon\left[I_p + a\left(\epsilon^2-1\right)\right]\sin\theta_0}{\left(\epsilon^2-1\right)\left(1+\epsilon\cos\theta_0\right)}\Bigg\},\end{aligned} \tag{99}$$

where $a = l^2/2k^2$ and $b = Z/k$.

4.3 RESULTS AND DISCUSSIONS

The TCSFA is a versatile method to account for diverse phenomena of strong field ionization in the semi-classical limit. In the last part of this chapter we apply the TCSFA to two case studies, which are analyzed from the quantum- and classical-mechanical aspects, respectively.

In Sec. 4.3.1, the dependence of the quantum interference on the number of laser cycles is presented. In order to facilitate a systematic analysis, we provide a pragmatical categorization of trajectories. Further detailed analysis of quantum interference, e. g., the intra-cycle interference including the sub-CC, is presented in Chapter 5.

In Sec. 4.3.2, the "ionization surprise" [48]—the LES [32, 33] is investigated [1]. The explanation of the LES has triggered considerable theoretical effort in several research groups [47, 1, 73, 74, 75, 24]. Analogous to the dynamics of a quantum wave packet, the collective behavior of trajectories explain the focusing of trajectories due to Coulomb effects.

4.3.1 *Temporal Analysis of Spectra: Cycle-Number Dependence*

In this section, we analyze how the number of laser cycles N_c affects the doubly-differential momentum spectra. The spectral features are progressively revealed by increasing the number of pulse cycles and hence the formation of spectra can be traced. Let us consider the photo-ionization of a hydrogen atom in a linearly polarized laser field of the frequency ω. In the polarization direction the laser field has the electric field component $E(t)$ and the vector potential $A(t)$,

$$E(t) = E_0 \cos \omega t, \quad A(t) = -A_0 \sin \omega t, \tag{100}$$

where $A_0 = E_0/\omega$. The duration of the laser is $T_p = 2\pi N_c/\omega$, and N_c is the number of laser cycles. The laser frequency $\omega = 0.0228$ (the wavelength 2 μm), the peak electric amplitude $E_0 = 0.0534$ (the intensity 1×10^{14} W/cm^2) and $I_p = 0.5$ are used. All results in this section (including the SFA) are numerically obtained with the trajectory-based implementation as described above. We set the charge $Z = 1$ for the TCSFA and $Z = 0$ for the SFA. Comparisons between results of the TCSFA and the SFA for different N_c are shown as follows.

4.3.1.1 *Strong Field Approximation ($Z = 0$)*

By appending increasing half-cycles, Fig. 3 shows the momentum distribution of the SFA for different N_c from $N_c = 0.5$ to $N_c = 1.5$. Since spectra are obtained by the coherent superposition of trajectories from different half-cycles, we can infer the origin of all interference patterns in terms of trajectories from the N_c-dependence. The temporal profile of trajectories corresponding to Fig. 3(a)-(c), respectively, is shown in Fig. 4. In Fig. 4(a)-(c), we plot the distribution of trajectories in the two-dimensional histogram as a function of ϕ and p_z, where $\phi = \omega t_r$ is the tunneling phase. In Fig. 4(d), the same histogram as a function of ϕ and p_x is shown for $N_c = 1.5$. Note we have $(p_z, p_x) = (p_{z0}, p_{x0})$ in the SFA.

In the SFA, trajectories are "short" if $z(t_r)$ and p_{0z} have the same sign, otherwise they are "long". A photoelectron of the short trajectory type drifts directly from the tunnel exit to the detector, whereas a photoelectron of the long trajectory type starts off into the "wrong" direction before its longitudinal momentum is reversed by the laser field.

Figure 3(a) shows the momentum distribution for $N_c = 0.5$. According to Eq. (156) for the monochromatic laser field, a trajectory whose tunneling time t_r fulfills $A(t_r) < 0$ has $p_z > 0$. In Fig. 4(a), two symmetrical branches of ϕ emerge as a function of p_z. One is "born" in the first quarter-cycle (the long trajectory) and the other in the second quarter-cycle (the short trajectory). The interference between trajectories of these two branches yields the fringes in Fig. 3(a). The interference is known as the "intra-cycle interference" [76] (more

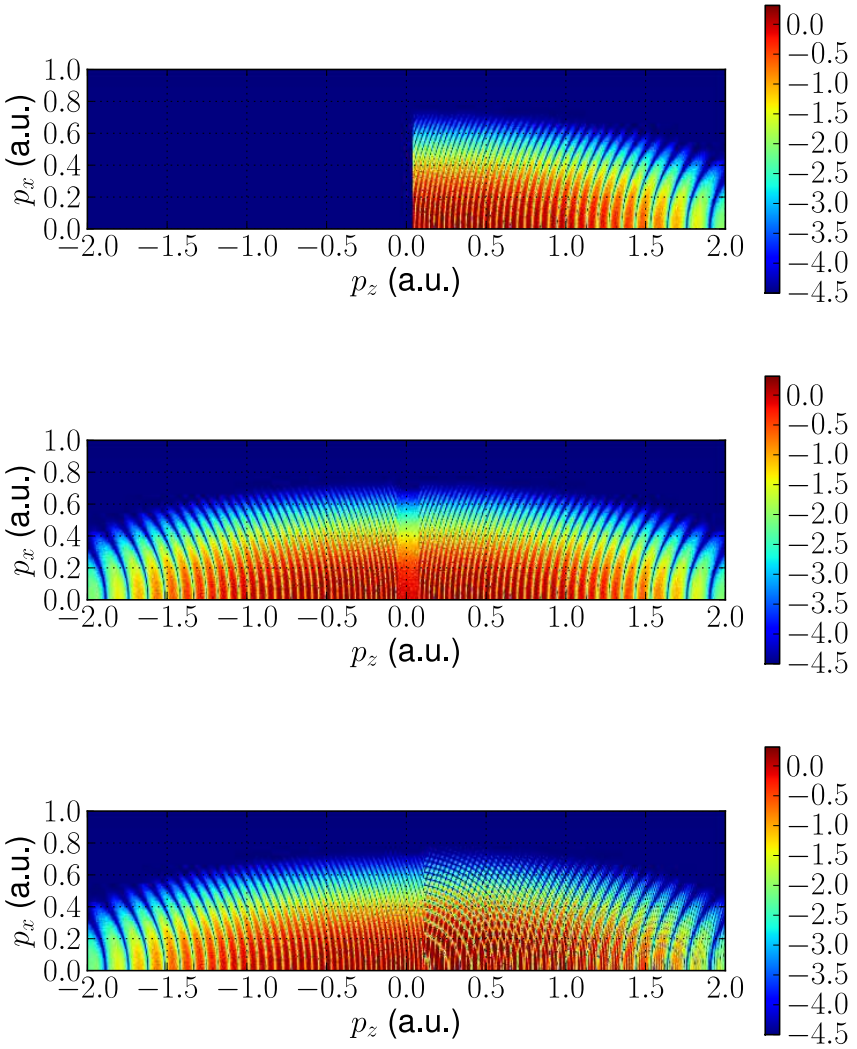

Figure 3: Photoelectron momentum distributions using different numbers of cycles of the laser pulse for the SFA ($Z = 0$). (a) $N_c = 0.5$, (b) $N_c = 1.0$ and (c) $N_c = 1.5$.

precisely, "intra-half-cycle interference"). Figure 4(a) shows a tilting ϕ-p_z distribution. Trajectories born at the extrema of the electric field ($\phi = 0$ and π for long and short trajectories, respectively) have relatively large weights, but end up with small $|p_z|$. In contrast, electrons "born" at t_r with $|E(t_r)| \sim 0$ gain the maximum kinetic energy near $2U_p$ in agreement with the prediction of the SMM.

Figure 3(b) shows a symmetric forward-backward momentum distribution for $N_c = 1$. The half momentum-plane for $p_z > 0$ remains the same as the one in Fig. 3(a) for $N_c = 0.5$, and the relevant trajectories have the tunneling phase $0 < \phi < \pi/2$. The other half plane for $p < 0$ records photoelectrons of $\pi/2 < \phi < \pi$. In the SFA, trajectories whose t_r are within the same single-cycle but in different half-cycles contribute to the distributions in forward- and backward-half momentum-planes separately.

In Fig. 3(c) for $N_c = 1.5$, electrons born in the third half-cycle of the laser field ($\pi < \phi < 3\pi/2$) contribute to the half momentum-plane $p_z > 0$ again, while the distribution for $p_z < 0$ remains the same as shown in Fig. 3(b). For $p_z > 0$, the interference between trajectories born in the first and the third half-cycles, known as the "inter-cycle interference", results in ring-like structures. Each ring corresponds to an ATI peak in energy spectra. In Fig. 4(c), the ϕ-p_z distribution for $\pi < \phi < 3\pi/2$ resembles the one for $0 < \phi < \pi/2$ in the half-plane of $p_z > 0$. The two patterns, fringes and rings, overlap for $p_z > 0$ due to the occurrence of both the intra-half-cycle interference and inter-cycle interference.

Figure 4(d) shows the distribution of trajectories in the ϕ-p_x plane for $N_c = 1.5$. In the SFA, p_x is invariant throughout the propagation in a linearly polarized field. Since trajectories start at initial momenta $p_{x0} > 0$, the ϕ-p_x distribution is confined rigorously in the upper-half momentum-plane $p_x > 0$. The distribution along the ϕ-axis is periodic with the maxima at peaks of the electric field. The distribution along the p_x-axis is roughly described by a Gaussian profile as expected from the adiabatic approximation [77].

4.3.1.2 *Coulomb Interaction ($Z = 1$)*

In order to investigate Coulomb effects, momentum distributions are calculated including the Coulomb interaction with $Z = 1$. Comparing with the SFA results, spectra for different N_c are shown in Fig. 5.

Figure 5(a) shows the TCSFA counterpart of Fig. 3(a) with $N_c = 0.5$. Even for the half-cycle laser field, the spectrum is significantly altered due to the Coulomb interaction. Firstly, instead of the rigorous one-to-one mapping in the SFA from the initial momentum $\vec{p}_0$ to the asymptotic momentum, $\vec{p} = \vec{p}_0$, the momentum distribution spreads into the momentum-plane of the opposite direction $p_z < 0$ and the higher energy region $p_z > 2.0$. Moreover, the scattering between the electron and the Coulomb center leads to classical boundaries near

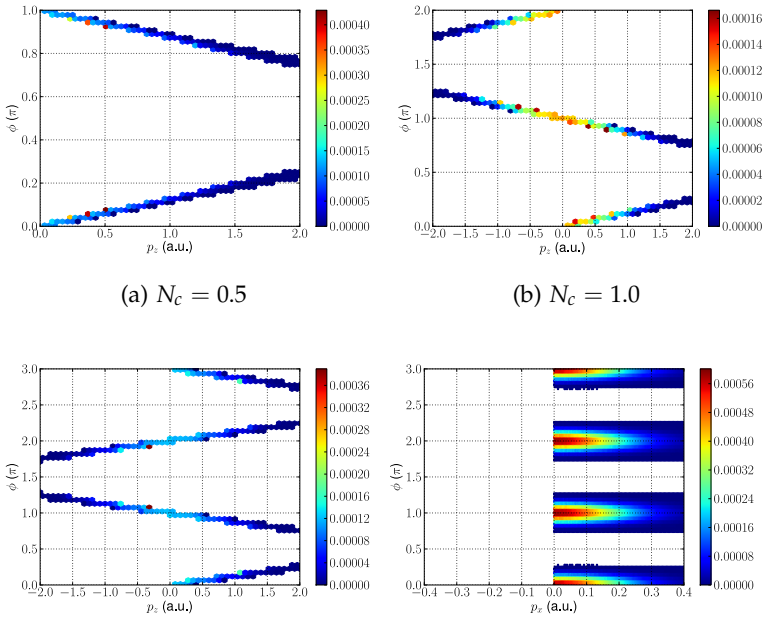

(a) $N_c = 0.5$ (b) $N_c = 1.0$

(c) $N_c = 1.5$ (d) $N_c = 1.5$

Figure 4: The dependence of the longitudinal momentum p_z on the initial tunneling phase $\phi = \omega t_r$ for different numbers of cycles in plain SFA with $Z = 0$.

the upper-right corner of the spectrum. In addition, interference patterns are modified. Fringes in the SFA are modulated by horizontally aligned side-lobes, which suggests a new type of interference plays a role. Correspondingly, the ϕ-p_z distribution in Fig. 6(a) deviates from the regular distribution for the plain SFA in Fig. 4(a). Given a tunneling phase ϕ, the distribution in the bottom branch corresponding to $0 < \phi < \pi/2$ (long trajectories) is scattered along the p_z-direction. The upper limit of p_z in the bottom branch is higher than in the SFA, since the Coulomb field can accelerate the photoelectron after its longitudinal direction of motion is reversed by the subsequent pulse cycle. The lower limit extends to the half-plane $p_z < 0$, which implies that backward scattering occurs. Within a single half-cycle, a scattered photoelectron can acquire a momentum in the opposite direction as high as $p_z = -1.8$. On the other hand, the distribution for short trajectories with $\pi/2 < \phi < \pi$ is less influenced by the Coulomb potential, since the electron of a short trajectory keeps moving away from the core throughout the propagation and feels a relatively weak force exerted by the Coulomb center. However, short trajectories may end up with $p_z < 0$ if p_{z0} is so small that the Coulomb force can drag the photoelectron into the opposite longitudinal direction permanently.

When $N_c = 1$, the half-plane $p_z < 0$ in Fig. 5(b) records photoelectrons of $\pi < \phi < 2\pi$. Instead of the forward-backward symmetric

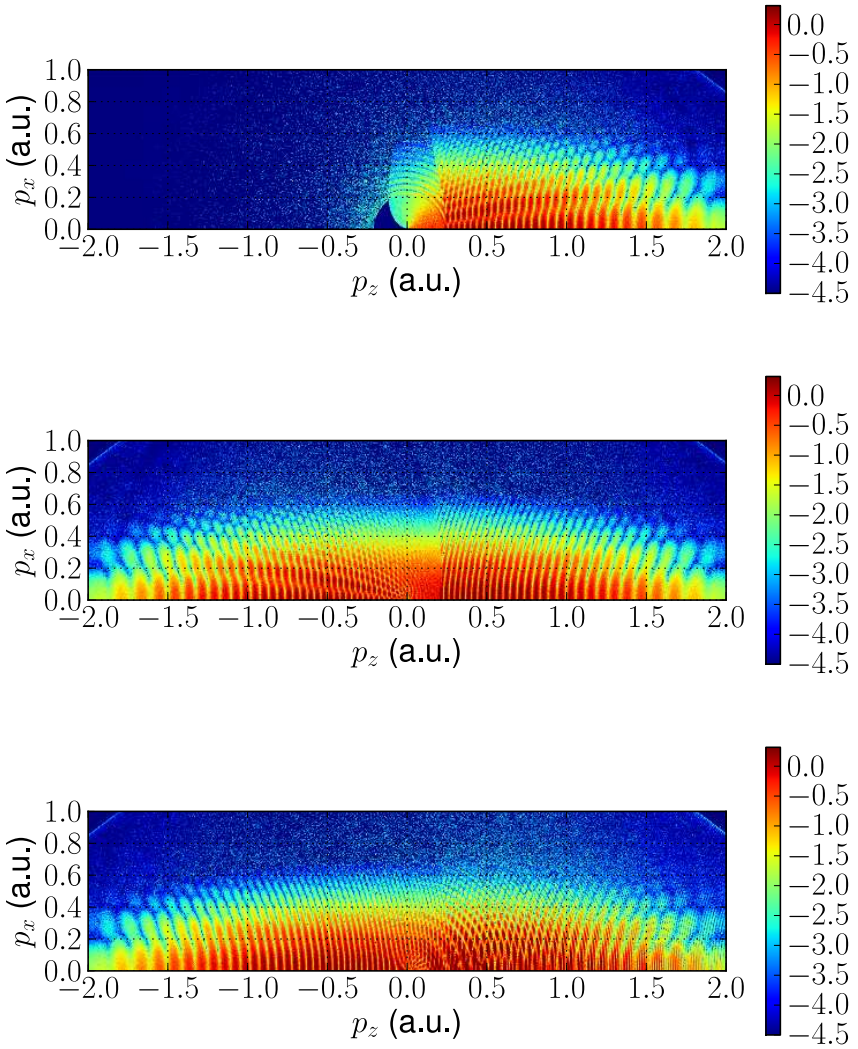

Figure 5: Photoelectron momentum distribution for different numbers of cycles with $Z = 1$: (a) $N_c = 0.5$, (b) $N_c = 1.0$ and (c) $N_c = 1.5$.

distribution in Fig. 3(b) for the SFA, the symmetry in 5(b) breaks down when the Coulomb field is present. In Fig. 5(c) for $N_c = 1.5$, ring-like structures due to the inter-cycle interference are found in the low-energy domain of the half-plane $p_z > 0$.

Figure 6(b) shows the ϕ-p_z distribution for $N_c = 1.0$. The distribution from the new half-cycle $\pi < \phi < 2\pi$ resembles the one in Fig. 6(a) except it is reversed in the p_z-direction. Moreover, the distribution of electrons born in the first half cycle $0 < \phi < \pi$ (the bottom branch) extends to $p_z \simeq -5.2$, corresponding to the $10U_p$-cutoff predicted by the SMM [Eq. (43)]. When $N_c = 1.5$, Fig. 6(c) shows that photoelectrons of $\pi < \phi < 2\pi$ also have the maximum momentum $p_z \simeq 5.2$ due to the rescattering, while the distribution of photoelectrons with $0 < \phi < \pi$ remains unchanged, which suggests the rescat-

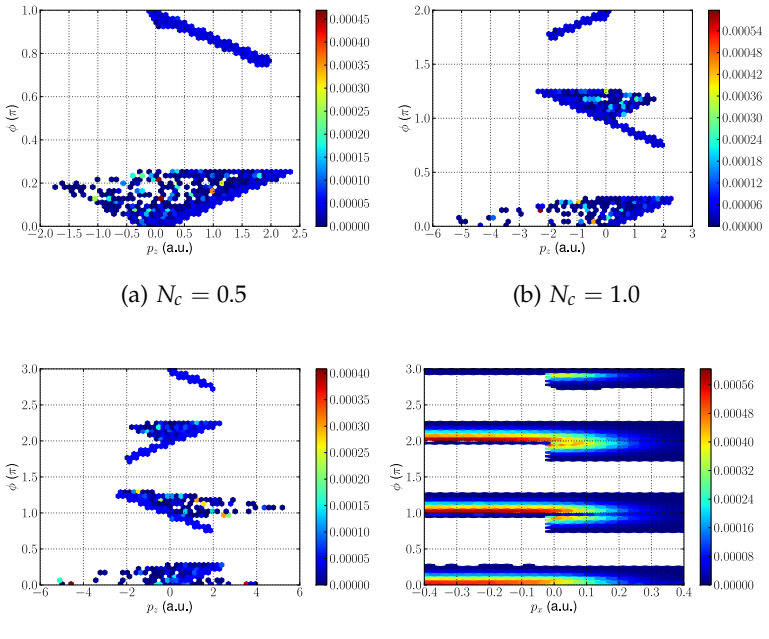

(a) $N_c = 0.5$ (b) $N_c = 1.0$

(c) $N_c = 1.5$ (d) $N_c = 1.5$

Figure 6: The dependence of the longitudinal momentum p_z on the initial tunneling phase $\phi = \omega t_r$ for different numbers of cycles with $Z = 1$.

tering in a linearly polarized field can occur only within a single cycle. In Fig. 6(d), the ϕ-p_x distribution for $N_c = 1.5$ is still similar to the SFA result [Fig. 4(d)] but loses the symmetry with respect to ϕ.

4.3.1.3 *Trajectory analysis for $N_c = 0.5$*

Though the pulse of $N_c = 0.5$ has the simplest temporal form, rich spectral features have already been revealed in Fig. 5(a). It is convenient to study this simplest case to understand how the classical boundaries and diverse interference patterns are formed. We choose 15 points related to typical spectral features, as indicated by labels in Fig. 7, and analyze the corresponding trajectories. Samples 1 to 12 and samples 13 to 15 have increasing p_z for $p_x = 0.165$ and 0.55, respectively. Let us define a circular bin whose center is located at the sample point i ($i = 1, ..., 15$) with a radius 0.02. We record all trajectories whose asymptotic momenta $\vec{p}$ fall into the defined bin. The corresponding trajectories for the ith sample are shown in the sub-figures of Fig. 8.

Samples 1-5 and 13 show trajectories (backward) scattering at the Coulomb center and ending up with $p_z < 0$. Trajectories for sample 1 in Fig. 8 have the largest scattering angle as the motion is almost along the p_z-axis. Decreasing $|p_z|$ in Fig. 7, trajectories depart from the polarization axis, while the number of trajectories in Fig. 8 and

the ionization probabilities in Fig. 7 increase. In addition, the excursion between the tunneling and the scattering events increases with the decreasing $|p_z|$.

Samples 6, 7 and 14 show trajectories near the small $|p_z|$ region. In Fig. 7, sample 6 is on the classical boundary which starts from the origin and spreads upwards. In Fig. 8, the corresponding trajectories start with initial momentum $p_{z0} \simeq 0$ and $p_{x0} > 0$, and then move upward. Since the Coulomb potential bends trajectories towards $p_z < 0$, in Fig. 6 we have distribution for $p_z < 0$ from trajectories which are expected to have $p_z > 0$ in the plain SFA. Since we have $p_{z0} \simeq 0$ for trajectories of sample 6, the classical boundary in Fig. 7 indicates the lower limit of p_z for an electron born at the tunnel exit $z(t_r) > 0$. For $p_{z0} < 0$, the tunneling exit moves to the other side $z(t_r) < 0$. Increasing p_z and moving away from the boundary, short trajectories which are also influenced by the Coulomb field contribute to the samples 7 and 14 in Fig. 7.

Sample 8 is positioned on a ring-like interference pattern. All trajectories for this sampling point analyzed above share similar dynamical properties, i. e., we observe just one branch of trajectories. However, there are two branches in Fig. 8. One branch represents short trajectories with the tunnel exits to the right side of the origin. The other branch is new to the SFA—the transverse component of the initial momentum $p_{x0} < 0$. The photoelectrons for this branch are supposed to move with $p_x < 0$, but intriguingly, their transverse momenta are reversed in the Coulomb field and these photoelectrons end up with the same asymptotic momentum with $p_x > 0$. In the following subsection 4.3.1.4 this new type of trajectories is referred to as T3. The superposition of transition amplitudes from T3 with short trajectories forms the ring-like interference pattern.

Samples 9 and 15 are located in another classical layer with richer interference features. The layer is formed by the emergence of long trajectories with their tunneling exits $z(t_r) < 0$. The analysis in Fig. 8 shows the pattern caused by the interference between short and long trajectories.

The spectral patterns around samples 10, 11 and 12 contain interference patterns including both fringes and side-lobes. Correspondingly, three groups of trajectories are clearly identified.

4.3.1.4 *Categorization of Trajectories*

For convenience sake, we extend the concept of "short" and "long" trajectories in the SFA and categorize types of trajectories as follows:

T1: "Short" trajectories, similar to the definition in the SFA, are born at the tunnel exits in the same direction of the longitudinal asymptotic momentum p_z. A trajectory is defined as T1 if it satisfies $p_z z_r > 0$, and $p_x p_{x0} > 0$.

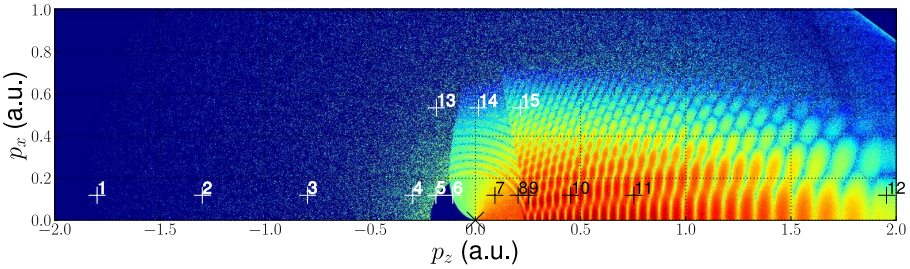

Figure 7: Sampling points for analysis. The crosses with labels indicate the momenta of samples which are referred to in the main text and in Fig. 8.

T2: "Long" trajectories, similar to the definition in the SFA, are born at the tunnel exits in the opposite direction of the longitudinal asymptotic momentum p_z. A trajectory is defined as T2 if it satisfies $p_z z_r < 0$ and $p_x p_{x0} > 0$.

T3: The trajectories are like the long trajectories T2 but has the transverse momentum p_x in the opposite direction. The transverse momentum of trajectories T3 is reversed later due to the Coulomb attraction and crosses the polarization axis. A trajectory is defined as T3 if it satisfies $p_z z_r < 0$ and $p_x p_{x0} < 0$.

T4: A trajectory is defined as T4 if it satisfies $p_z z_r > 0$, and $p_x p_{x0} < 0$.

Only when the Coulomb interaction is included can trajectories T3 and T4 exist, because in the SFA the transverse momentum is conserved ($p_x = p_{x0}$) in a linearly polarized field. However, when we take the Coulomb force into consideration, p_x changes. Note that the definitions of the types of trajectories in the form of formulas only specify boundary conditions but do not rigorously capture entire trajectories. If the whole dynamics are considered, the situation is more complicated, e. g., a trajectory may orbit the core for more than once. Nevertheless, the probability of the occurrence of such complicated orbits is usually low for the current parameters where a semi-classical treatment is valid.

4.3.1.5 *Partial Spectra*

Not only can we extract trajectories corresponding to a certain spectral feature, but also we are able to reproduce the spectrum from a given set of trajectories. With the categorization of trajectories in Sec. 4.3.1.4, we can select certain types of trajectories to calculate partial spectra. If certain spectral patterns can be reconstructed from a partial spectrum, we successfully identified the types of trajectories that are "responsible" for this spectral feature. Taking the interference pattern of the plain SFA for instance, the vertically aligned fringes are essentially reflected by the partial spectra constructed with trajectories T1+T2.

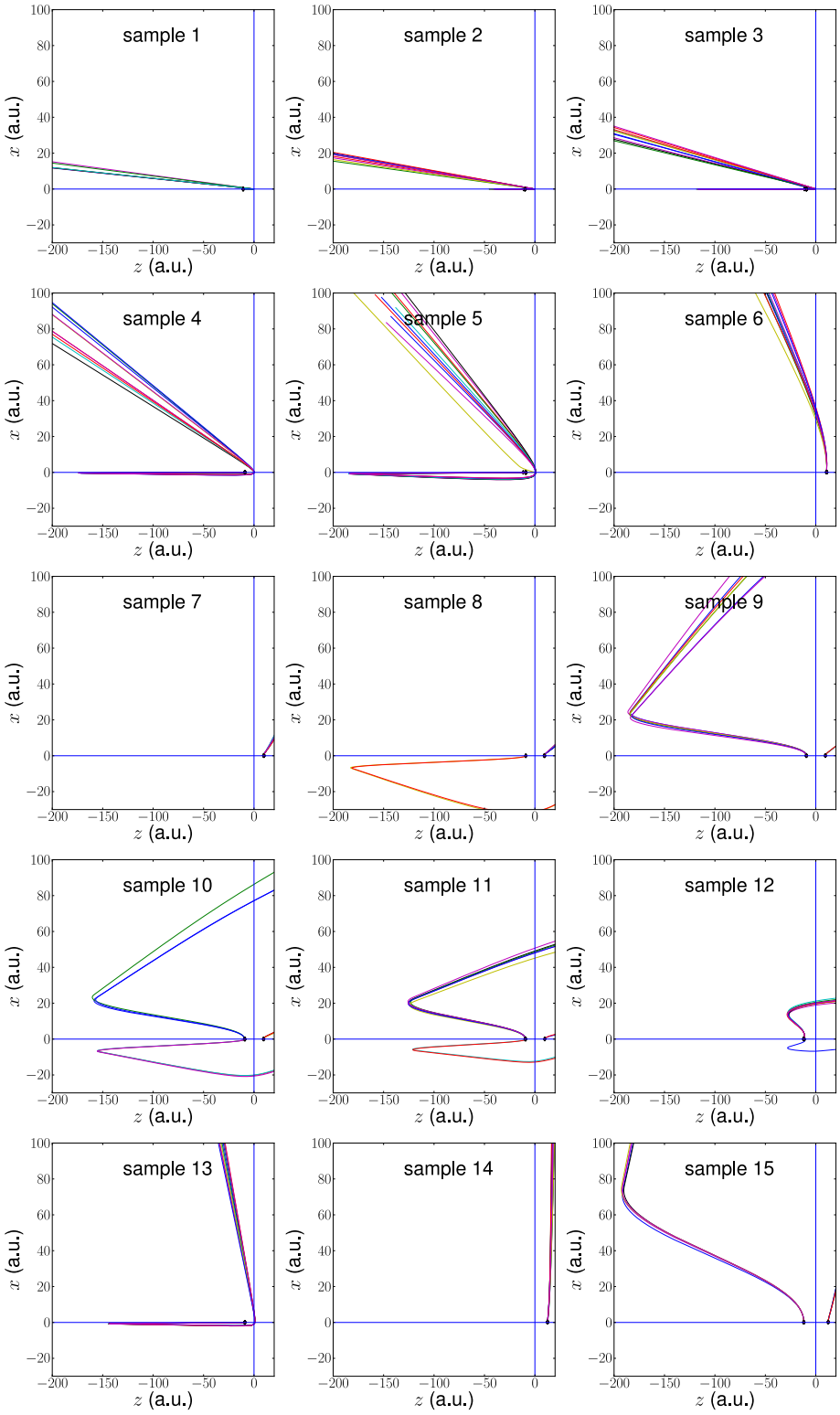

Figure 8: Trajectories for the samples labeled in Fig. 7. In each sub-figure, the asymptotic momenta of all trajectories are identical. The Coulomb center is located at the origin. The diamond symbols along the polarization direction represent tunnel exits of photo-electrons.

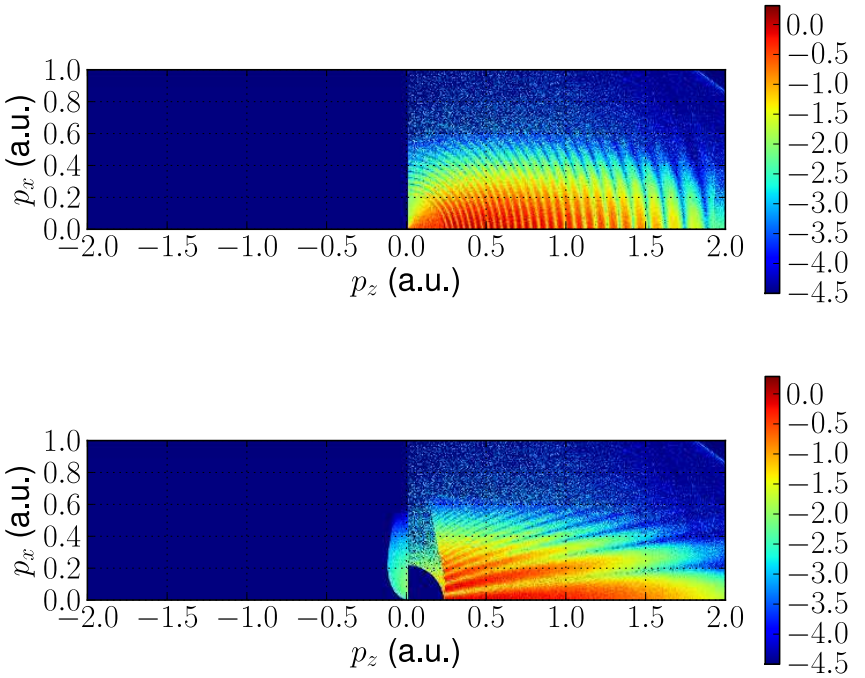

Figure 9: Partial spectra constructed with combinations of different types of trajectories: T1+T3 (a) and T2+T3 (b).

Figure 9(a) and (b) show partial spectra of trajectories T1+T3 and T2+T3, respectively. The interference between trajectories T1+T3 results in ring-like structures in the central part of Fig. 5(a). The superposition of T2+T3 forms side-lobes, which were discovered in a recent experiment and used for atomic holography in long wavelength laser radiation [78, 79, 80].

4.3.2 *Low-Energy Structure [1]*

As is discussed in Chapter 3, the Coulomb potential increases the ionization probability due to the tunneling enhancement, in particular, along the polarization direction. The mapping in the momentum space, from the initial momentum to the asymptotic momentum during the real-time propagation, may be modified. Especially in the low energy regime, the motion of electrons is strongly modified by the Coulomb interaction. The LES is such an example.

Let us consider an atom which is subjected to the light field described by the vector potential of a $\sin^2$-envelope,

$$A(t) = \begin{cases} -\frac{E_0}{\omega} \sin^2\left(\frac{\omega t}{2N_c}\right) \sin \omega t, & 0 \leq t \leq \frac{2N_c\pi}{\omega}, \\ 0, & \text{otherwise}, \end{cases} \tag{101}$$

with the laser frequency $\omega = 0.0228$ (wavelength $\lambda = 2$ μm), the peak field amplitude $E_0 = 0.0534$ (intensity $I = 100$ TW/cm^2) and the number of cycles $N_c = 3$. Motivated by the experiments [32, 33, 81], the argon atom is initially in the $1s$ state with the ionization potential $I_p = 0.576$. In the TDSE calculation, the binding potential is modeled by $V(r) = -1/r - 17.0e^{-17.43r}/r$. In the TCSFA, up to 10^7 trajectories are launched to obtain the corresponding transition amplitudes, which are binned into a 400×100 grid for post-processing and calculation of the momentum spectra. The results are tested for numerical convergence by increasing the number of time steps for the calculation of the trajectories. Increasing the number of trajectories enhances the resolution of the spectra.

Figure 10 presents the SFA, TCSFA and TDSE photoelectron momentum spectra. Several discrepancies between the TDSE and the SFA results are found: (i) the SFA predicts a symmetric momentum distribution while the TDSE spectrum is strongly asymmetric [18]. (ii) The radial structures [40, 64] around $\vec{p} = \vec{0}$ present in the TDSE spectrum are absent in the SFA result. (iii) Several side-lobes in the TDSE result are clearly visible for $p_z < 0$ but completely absent in the SFA. In 10(b) we anticipate the spectrum obtained with our TCSFA method, which is—as regards points (i)–(iii) above—in excellent agreement with the TDSE result. Only the probability along a line from $\vec{p} = (p_z, p_x) \simeq (-0.3, 0)$ to $(-0.1, 0.25)$ is overestimated. However, it turns out that this feature is related to the LES, as will be shown below.

The TDSE momentum spectrum in Fig. 10(c) does not allow a clear identification of the LES. In order to compare the TDSE results with Refs. [32, 81] angle-resolved energy spectra $dw(\mathcal{E}, \theta)/\sin\theta d\theta d\mathcal{E} = p|M_{\vec{p}}|^2$ were calculated. Figure 10(d) clearly shows the LES for the directional energy spectrum anti-parallel ($\theta = 180^\circ$) to the polarization axis. Because of the short pulse duration, no LES is visible for $\theta = 0^\circ$ (not shown), which helps to identify unambiguously the origin of the LES in the following. Despite the short pulse in our simulations Fig. 10(d) compares well with the experimental result in Fig. 3(b) of [81].

The TCSFA result in 10(b) shows the above introduced Coulomb features (i)–(iii) of the TDSE calculation. In addition there is a structure formed by an overestimated yield of photoelectrons with a maximum at $\vec{p}_c = (p_{cz}, p_{cx}) = (-0.22, 0.1)$. We have checked that for a fixed number of cycles in the pulse this maximum moves closer towards the polarization axis as the wavelength is increased. For shorter wavelengths it fades away while becoming more ringlike. With an increasing number of laser cycles (keeping $\lambda = 2$ μm fixed) the structure also appears in the opposite direction, as expected. Moreover, with an increasing pulse duration the structure narrows and moves more and more on axis. This is a strong indication that the structure formed by the overestimated photoelectron yield we observe in

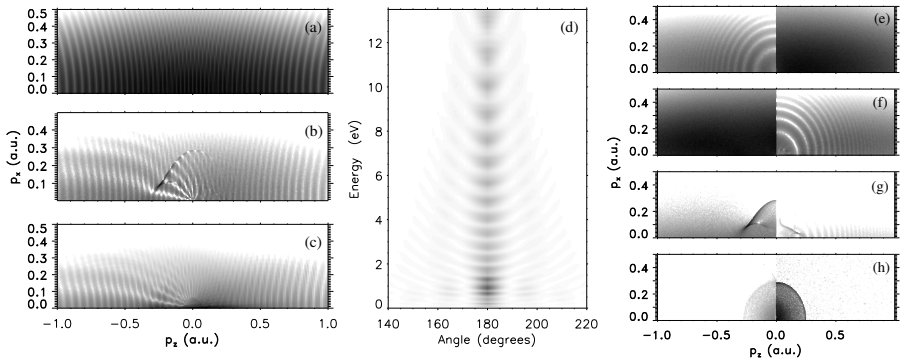

Figure 10: Logarithmically scaled photoelectron momentum distributions in the p_z-p_x plane calculated using (a) plain SFA, (b) TCSFA and (c) numerical solution of the TDSE. Panel (d) shows the linearly scaled, angle-resolved energy spectra in backward direction ($p_z < 0$) with the LES around 1 eV clearly visible. Each spectrum was normalized to its maximum value. (e)-(h) are partial spectra due to trajectories of types T1-T4.

the semi-classical TCSFA approach is the LES seen in the full quantum TDSE simulations and measured in the experiments.

It was argued already in the accompanying article [48] that the LES is due to low-energy forward scattering at the Coulomb potential. Certainly, only electrons emitted with high probability, i. e., when the absolute value of the electric field is high, can contribute to such a pronounced spectral feature as the LES. The quantum trajectories of the TCSFA responsible for the yield around $\vec{p}_c$ illustrate and confirm this viewpoint.

In order to understand the origin of spectral features such as the LES it is useful to study the partial contributions of each class of trajectories (categorized in Subsection 4.3.1.4) to the total spectrum in Fig. 10(b). Sub-figures 10(e)-(h) show the partial spectra in which interference patterns can only originate from the interference of trajectories of the same type. Clearly, the LES at $\vec{p}_c = (-0.22, 0.1)$ is generated by T3 trajectories. The LES is not due to interference of T3 trajectories. This we checked by adding all T3 contributions incoherently, giving the same LES structure. In fact, low-energy structures have also been observed in classical ensemble calculations [33].

As we have identified the T3 electrons as being responsible for the LES, we hereby confirm the conclusion in the recent work [47] that the change of the electrons' transverse momenta is the key for the understanding of the LES. This also explains why no LES was observed in one-dimensional TDSE simulations. But why do particularly many T3 quantum trajectories end up at $\vec{p}_c$ in momentum space so that the probability there is even overestimated as compared to the TDSE results? It is known from the Coulomb-free SFA with rescattering in-

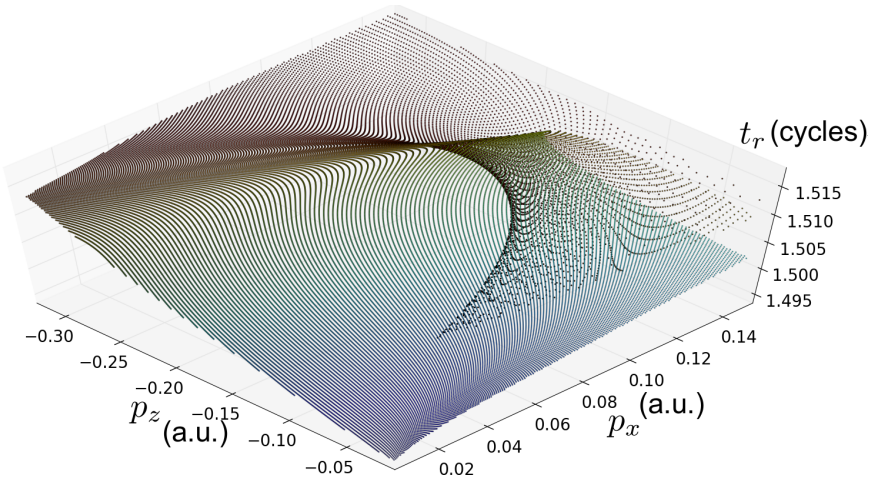

Figure 11: Emission times of T3 trajectories contributing to final momenta where the caustic structure is located. At $\vec{p}_c$ the number of contributing trajectories is particularly high (steep slope).

cluded [82] that semi-classical solutions merge or branch across classical boundaries (CBs) in the momentum plane [83]. When calculating the photoelectron spectra at the CBs one encounters singularities because of vanishing Jacobians in the denominator that describe the mapping from initial to final momentum $\{p_{0z}, p_{0x}\} \to \{p_z, p_x\}$. Such singularities form *caustics* in the photoelectron momentum spectra. The LES is a caustic formed at the CB for T3 trajectories, giving rise to the sharp structure visible in Fig. 10(g). This is shown explicitly in Fig. 11 where the emission times t_r of T3 trajectories contributing to final momenta around the caustic structure are indicated. Particularly many T3 trajectories contribute to $\vec{p}_c$. In the numerical TCSFA implementation singularities are smoothed out because of the finite number of trajectories. In exact quantum treatments like our solution of the TDSE there are no singularities but only local maxima because of the low energy forward scattering at a Coulomb potential. In improved semi-classical theories the singularities at CBs are also removed [84, 85].

5

TRAJECTORY ANALYSIS OF INTERFERENCE PATTERNS

In Sec. 4.3.1, the formation of quantum interferences is intuitively investigated by calculating momentum distributions and studying their dependence on increasing numbers of laser cycles. In this chapter, we will analytically discuss quantum interferences and analyze the influences caused by the Coulomb interaction. Comparisons between *ab initio*, SFA and TCSFA results are shown to survey Coulomb effects. In fact, the SFA can describe general interference patterns in photoelectron spectra with the advantage over classical models, e. g., the SMM, or the quasi-static method whose results lose all information about quantum interferences. The explication of the quantum interference with quantum orbits as the semi-classical approximation of the SFA is straightforward. However, subtle features of these interferences predicted by the SFA usually deviate from *ab initio* and experimental results, particularly in the low-energy regime. Such deviations are usually intolerable if quantum interference is used to mine information about ionization dynamics or atomic structure, since the granularity of the interference in momentum distributions is usually fine and any deviation would spoil the structure. Hence, it is necessary to refine the theoretical method to better describe spectra obtained by nowadays state-of-art high-resolution experimental techniques. The TCSFA shows that the incorporation of the Coulomb interaction can substantially improve results and help identify Coulomb-induced modifications to interference patterns. The modification induced by the Coulomb interaction may come from either the real-space propagation or from the sub-barrier propagation. In general, the former is due to the distortion of electronic trajectories under the influence of the long-range Coulomb interaction. The latter is caused by the sub-CC. With quantum orbits, we analyze the quantum interference by studying the superposition of different types of trajectories. In the following, we categorize the hitherto observed phenomena of quantum interferences in momentum distributions and present a systematic method to facilitate the analysis.

Typical momentum spectra include several interference structures. Taking the momentum distribution calculated with the *ab initio* TDSE method [Fig. 14(a), laser parameters are listed in the caption] for instance, interference patterns may contain ATI rings, fringes, side-lobes and the bouquet-like radial structures near the ionization threshold ($|\vec{p}| \simeq 0$).

- ATI rings. If the number of laser cycles is large enough, the ATI rings are the most significant interference pattern with regular ring-like structure.
- Fringes. The fringes are less significant. They align vertically near the polarization axis but bend outwards to the higher-$|p_z|$ direction as p_x increases. When fringes overlap with ATI rings, nodal structures are formed along rings.
- Side-lobes. The pattern of side-lobes aligns almost horizontally in momentum spectra, spreading from the low-$|p_z|$ to high-$|p_z|$ regime. This pattern only appears when the long-range Coulomb interaction is considered. Side-lobes are usually identifiable in light fields of long wavelengths and used for strong-field photoelectron holography (SFPH) [78, 80].
- Low-energy radial structure. The interference pattern near the continuum threshold ($|\vec{p}| \simeq 0$) exhibits finger- or bouquet-like structures. The near-threshold radial structure results from interfering trajectories released at different times but reaching the same Kepler asymptote [28].

In the context of quantum orbits, the quantum interference originates from the superposition (76) associated with different trajectories leading to the same asymptotic momentum. The starting point of the analysis is simply to find the relevant interfering trajectories. In the following section, the analysis of the above mentioned interference patterns in terms of quantum orbits is introduced.

5.1 INTERFERENCE PATTERNS FOR THE SFA

Let us consider an N-cycle linearly-polarized, monochromatic laser field given by (100). The polarization direction is along the z-axis and the motion of the photoelectron is studied in the two-dimensional z-x plane. In the following the subscripts "z" and "x" are used to indicate components of vectors. Substituting the velocity $\vec{v} = \vec{p} + \vec{A}(t)$ into the action (78) for a trajectory without the Coulomb interaction ($Z = 0$), we obtain

$$W(t_s) = \left\{ -\int^t dt' \left[\frac{1}{2}\left(p_z - \frac{E_0}{\omega}\sin\omega t' \right)^2 + \frac{1}{2}p_x^2 + I_p \right] \right\} \Bigg|_{t_s}^{\infty}.$$

The boundary at $t \to \infty$ can be neglected, since $W(\infty)$, being a real constant value, does not contribute to the ionization probability. Moreover, it has no influence on the interference since the value of $W(\infty)$ is a constant for all trajectories of the same asymptotic momentum $\vec{p}$. Neglecting all trivial t_s-independent terms, we have

$$W(t_s) = \left(\frac{1}{2}p^2 + I_p + U_p \right) t_s + \frac{E_0 p_z}{\omega^2}\cos\omega t_s - \frac{E_0^2}{8\omega^3}\sin 2\omega t_s, \quad (102)$$

where $U_p = E_0^2/(4\omega^2)$ and $p = \sqrt{p_z^2 + p_x^2}$. Substituting $W(t_s)$ into the transition amplitude (76) and factoring the same prefactor out of all terms, (76) becomes

$$M_p = S''^{-1} \sum_\alpha e^{i\left(\frac{1}{2}p^2 + I_p + U_p\right)t_s^{(\alpha)}} e^{i\left(u\cos\omega t_s^{(\alpha)} - v\sin 2\omega t_s^{(\alpha)}\right)}, \tag{103}$$

where $u = E_0 p_z/\omega^2$ and $v = E_0^2/(8\omega^3)$. Following [58], using the Jacobi-Anger identity [86],

$$e^{iu\sin\theta + iv\sin 2\theta} = \sum_{n=-\infty}^{\infty} e^{in\theta}\tilde{J}_n(u,v), \tag{104}$$

where $\tilde{J}_n(u,v)$ is the generalized Bessel function which, expanded in ordinary Bessel function $J_n(v)$, reads

$$\tilde{J}_n(u,v) = \sum_{k=-\infty}^{\infty} J_{n-2k}(u)J_k(v), \tag{105}$$

we have

$$e^{iu\cos\theta - iv\sin 2\theta} = \sum_{n=-\infty}^{\infty} e^{in\left(\theta+\frac{\pi}{2}\right)}\tilde{J}_n(u,v). \tag{106}$$

Substituting (106) into the transition amplitude (103) yields

$$\begin{aligned} M_p &= S''^{-1} \sum_\alpha e^{i\left(\frac{1}{2}p^2 + I_p + U_p\right)t_s^{(\alpha)}} \sum_{m=-\infty}^{\infty} e^{im\left(\omega t_s^{(\alpha)} + \frac{\pi}{2}\right)} \tilde{J}_m\left(\frac{E_0 p_z}{\omega^2}, \frac{E_0^2}{8\omega^3}\right), \\ &= S''^{-1} \sum_{m=-\infty}^{\infty} \tilde{J}_m\left(\frac{E_0 p_z}{\omega^2}, \frac{E_0^2}{8\omega^3}\right) e^{im\pi/2} \sum_\alpha e^{iE_p(m)t_s^{(\alpha)}}, \end{aligned} \tag{107}$$

where $E_p(m) = \left(\frac{1}{2}p^2 + I_p + U_p + m\omega\right)$.

The sum over m in Eq. (107) describes the total contribution from different numbers of absorbed photons m. The sum over α describes, for a given m, the interference between different semi-classical trajectories associated with their saddle points $t_s^{(\alpha)}$. In a monochromatic laser field, each cycle has a pair of saddle points $t_s^{(1)}$ and $t_s^{(2)}$ for a given asymptotic momentum (Sec. A.2). All other saddle points are simply periodic repetitions with the fixed temporal interval. Given a pair of saddle points $t_s^{(1,2)}$ for the first cycle, the saddle points in the kth cycle are given by

$$t_s^{(\alpha)} \equiv t_s^{(1,2;k)} = t_s^{(1,2)} + k\frac{2\pi}{\omega}. \tag{108}$$

Therefore the sum over α in (107) reads

$$\begin{aligned} \sum_\alpha e^{iE_p(m)t_s^{(\alpha)}} &= \sum_{i=1}^{2}\sum_{k=0}^{N_c} e^{iE_p(m)\left(t_s^{(i)} + \frac{2k\pi}{\omega}\right)} \\ &= \sum_{i=1}^{2} e^{iE_p(m)t_s^{(i)}} \sum_{k=0}^{N_c} e^{iE_p(m)\frac{2k\pi}{\omega}}. \end{aligned} \tag{109}$$

With the factorization (109) of the sum (107), two different interference patterns are identified:

- Inter-cycle interference. The second term $\sum_{k=0}^{N_c}$ does not rely on saddle points. Instead, it describes the general interference between all cycles. The series expansion with the exponential function can be calculated with the Dirichlet kernel [87]

$$D_n(x) \equiv \sum_{k=-n}^{n} e^{ikx} = \frac{\sin\left[\left(n+\frac{1}{2}\right)x\right]}{\sin\left(\frac{x}{2}\right)}. \tag{110}$$

  In consequence, the second term in (109) reads

$$\sum_{k}^{N} e^{ikE_p(m)\frac{2\pi}{\omega}} = \frac{\sin\left[\left(n+\frac{1}{2}\right)E_p(m)\frac{2\pi}{\omega}\right]}{\sin\left(E_p(m)\frac{\pi}{\omega}\right)}.$$

  For long pulses as $N_c \to \infty$,

$$\sum_{k}^{\infty} e^{ikE_p(m)\frac{2\pi}{\omega}} = \omega\delta\left(\frac{1}{2}p^2 + I_p + U_p + m\omega\right).$$

  The δ-function reflects energy conservation for an ATI peak which is related to the absorption of m photons.

- Intra-cycle interference. The terms of the sum $\sum_{i=1}^{2}$ depend for a given asymptotic momentum on two trajectories within a single cycle and is thus called intra-cycle interference. Using the relation that $t_s^{(2)} = \pi/\omega - \mathrm{Re}t_s^{(1)} + i\mathrm{Im}t_s^{(1)}$, we can rewrite $\sum_{i=1}^{2}$ in terms of $t_s^{(1)}$,

$$\begin{aligned}\sum_{i}^{2} e^{iE_p(m)t_s^{(i)}} &= e^{iE_p(m)t_s^{(1)}} + e^{iE_p(m)t_s^{(2)}} \\ &= e^{iE_p(m)\left[\mathrm{Re}t_s^{(1)} + i\mathrm{Im}t_s^{(1)}\right]} + e^{iE_p(m)\left[\pi/\omega - \mathrm{Re}t_s^{(1)} + i\mathrm{Im}t_s^{(1)}\right]} \\ &= e^{-E_p(m)\mathrm{Im}t_s^{(1)}}\left[e^{iE_p(m)\mathrm{Re}t_s^{(1)}} + e^{iE_p(m)\pi/\omega}e^{-iE_p(m)\mathrm{Re}t_s^{(1)}}\right].\end{aligned}$$

  Choosing the momentum corresponding to ATI peaks in photoelectron spectra, $E_p(m) = k\omega$, the intra-cycle interference is reduced to

$$\sum_{i=1}^{2} e^{iE_p(m)t_s^{(i)}} = 2e^{-E_p(m)\mathrm{Im}t_s^{(1)}}\cos\left[E_p(m)\mathrm{Re}t_s^{(1)}\right].$$

In summary, inter-cycle and intra-cycle interferences can be identified from Eq. (109) for the SFA, in agreement with the numerical results in section 4.3.1. Accordingly, the interpretation of interference patterns is feasible [88]. In the next section, we apply a similar analysis to study intra-cycle interference.

5.2 COULOMB EFFECTS ON INTRA-CYCLE INTERFERENCE [2]

Supposing two types of quantum orbits, (a) and (b), are dominant for a certain momentum $\vec{p}$, and each has the transition amplitude $M_{\vec{p}}^{(a)}$ and $M_{\vec{p}}^{(b)}$, respectively, the ionization probability of the photoelectron is

$$w(\vec{p}) = \left[M_{\vec{p}}^{(a)} + M_{\vec{p}}^{(b)}\right] * \left[M_{\vec{p}}^{(a)} + M_{\vec{p}}^{(b)}\right]$$

with $M_{\vec{p}}^{(\alpha')} \sim e^{iW^{(\alpha')}}$ $(\alpha' = a, b)$. The action $W^{(\alpha')}$ is of the form (78). Interference with pronounced contrast requires the weights of $M_{\vec{p}}^{(a)}$ and $M_{\vec{p}}^{(b)}$ being comparable, $e^{-\mathrm{Im}W^{(a)}} \sim e^{-\mathrm{Im}W^{(b)}}$. If this is the case,

$$\begin{aligned} w(\vec{p}) &= \sum_{\alpha=a,b} \left[e^{-\mathrm{Im}W^{(\alpha)}}\right]^2 + 2e^{-\mathrm{Im}\left[W^{(a)}+W^{(b)}\right]} \cos\phi \\ &\simeq 2e^{-2\mathrm{Im}W^{(a)}} \left(1 + \cos\phi\right). \end{aligned}$$

Hence, the interference is determined by the phase difference $\phi = \mathrm{Re}[W^{(b)} - W^{(a)}]$. For $\phi = m\pi$ with m even we have interference maxima, for m odd interference minima, provided prefactors $\mathcal{P}(t_s^{(\alpha)})$ in (77) do not introduce extra phase difference, which is true for the tunneling ionization starting from the ground state.

From (79) and (82), the full form of the action is separable as $W = W^{\mathrm{sub},0} + W^{\mathrm{re}} + W^{\mathrm{subcc}}$ including the sub-CC action W^{subcc}. Accordingly, we can split the phase difference ϕ,

$$\phi = \phi^{\mathrm{sub},0} + \phi^{\mathrm{re}} + \phi^{\mathrm{subcc}} \tag{111}$$

which can be used to analyze the influence of Coulomb effects on the interference pattern.

5.2.1 *Model*

In order to investigate the influence of the sub-CC on the interference pattern in photoelectron momentum spectra we consider H($1s$) ($I_p = 0.5$) in a linearly polarized laser pulse. The vector potential of the laser pulse of carrier frequency ω is given by Eq. (101). $A_0 = E_0/\omega$ is the vector potential amplitude.

Figure 12(a) shows the photoelectron momentum spectrum, calculated from the exact numerical solution of the TDSE using the QPROP code [89]. The laser parameters are $N_c = 4$, $\omega = 0.0228$, $E_0 = 0.0534$ (corresponding to $\lambda = 2$ μm and an intensity of 10^{14} W/cm^2). Here we focus on the almost vertically aligned interference fringes. These fringes are discussed in Sec. 4.3.1 as a result of intra-half-cycle interference of two trajectories "born" at times $t_r^{(1)}$ and $t_r^{(2)}$. The electric field has opposite signs at $t_r^{(1)}$ and $t_r^{(2)}$, meaning that the tunnel exits point in opposite directions.

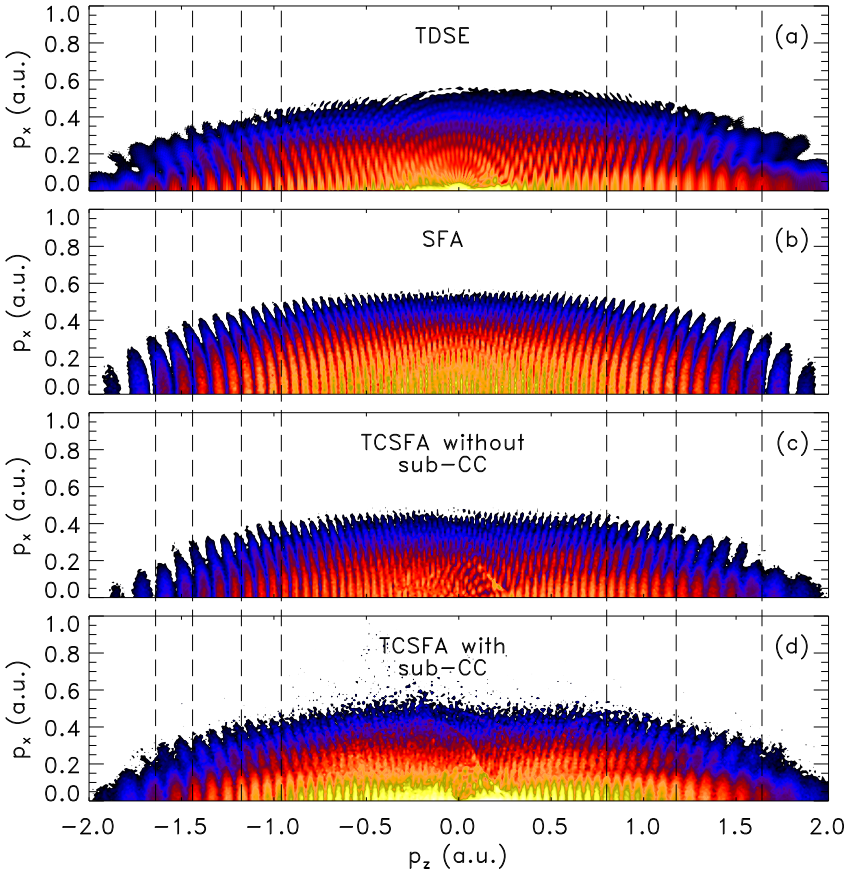

Figure 12: Logarithmically scaled photoelectron momentum distribution in the p_z-p_x plane calculated using (a) TDSE, (b) plain SFA, (c) TCSFA without sub-CC, and (d) TCSFA with sub-CC. The calculation is for H(1s) in a 4-cycle, $\sin^2$-envelope, near-infrared laser pulse of wavelength $\lambda = 2$ μm and intensity 10^{14} W/cm^2. Four orders of magnitude in probability are shown.

The vertical fringes are also present in the SFA spectrum Fig. 12(b). However, the positions are shifted relative to the TDSE results. When there is constructive interference in the TDSE result, there is destructive interference in the SFA spectrum, and *vice versa*. This indicates that there is an erroneous phase-shift of π between the long and the short trajectory in the plain SFA as compared to the exact TDSE result. It is expected that incorporating the Coulomb-attraction between the outgoing electron and the parent ion should cure this disagreement.

Let us now "switch-on" the Coulomb-attraction for the propagation in the classically allowed region (from the tunnel exit to the detector). The result is shown in Fig. 12(c). As has been discovered recently [78], side-lobes are reproduced by incorporating the Coulomb correction to real trajectories. However, the vertical interference fringes still have the same position as in the plain-SFA result, meaning that the erroneous phase-shift between the long and the short trajectory of π is not cured by the Coulomb-correction out of the Coulomb-barrier. Only if the sub-CC (84) is incorporated as well, do positions of fringes coincide with the *ab initio* TDSE result, as is shown by Fig. 12(d). Hence, the sub-CC not only affects the statistical weight of a quantum orbit via the imaginary part of W^{subcc} but also the interference pattern in photoelectron spectra via the real part of W^{subcc}. In the following we show how the introduction of W^{subcc} cures the erroneous phase shift and derive an analytical expression for ϕ^{subcc} in the long-wavelength limit.

5.2.2 *Momentum Distribution in Polarization Direction with $\omega \to 0$*

In the long-wavelength limit ($\omega \to 0$) it is possible to evaluate the sub-CC phase difference ϕ^{subcc} in the polarization direction analytically. We consider a monochromatic laser field (100) and assume $A_0 > 0$. We will prove that in the long wavelength limit we obtain a momentum-independent sub-CC phase shift of

$$|\phi^{\text{subcc}}| = \frac{Z\pi}{\sqrt{2I_p}}. \tag{112}$$

In particular, for the case of Fig. 12 where $Z = 2I_p = 1$ we have $|\phi^{\text{subcc}}| = \pi$, turning constructive interference maxima of the plain SFA into destructive interference minima in the TCSFA with sub-CC and *vice visa*. As we know already from the results in Fig. 12 that the Coulomb correction of the propagation in real space is not responsible for the fringe shift, we ignore its effect on $\vec{p}_0^{(1)}$ and $\vec{p}_0^{(2)}$ (and thus also on $t_s^{(1)}$ and $t_s^{(2)}$) in this section and assume

$$\vec{p}_0^{(1)} = \vec{p}_0^{(2)} = \vec{p}, \tag{113}$$

which we know is valid along the polarization axis in the long-wavelength regime from numerical results. For a monochromatic

laser field (100), $\vec{p} = (p_x, p_z)$, and $t_s = t_r + it_i$ the saddle point equation (35) yields

$$\sin(\omega t_r)\cosh(\omega t_i) = \frac{p_z}{A_0}, \tag{114}$$

$$\cos(\omega t_r)\sinh(\omega t_i) = \mp\frac{\sqrt{2I_p + p_x^2}}{A_0}. \tag{115}$$

Equation (114) shows that the possible t_r can be determined as the intersections between $p_z/\cosh\omega t_i \overset{\omega\to 0}{\simeq} p_z$ and the negative vector potential $-A(t) = A_0 \sin\omega t$, as indicated in Fig. 13(b). The figure shows that a pair of saddle points per cycle, e. g., $t_s^{(1+)}$ and $t_s^{(2+)}$, exists for a specified p_z (dashed horizontal lines). The so-called intra-cycle interference is thus due to two saddle-points for which

$$\begin{aligned} \vec{p}^{(1)} &= \vec{p}^{(2)} = \vec{p}, \\ t_r^{(1)} &= \frac{\pi}{\omega} - t_r^{(2)}, \\ t_i^{(1)} &= t_i^{(2)} = t_i \end{aligned} \tag{116}$$

are fulfilled. In the polarization direction, $p_x = 0$, the sub-CC action is

$$W^{\text{subcc}} = \int_{t_s}^{t_r} \frac{Z}{\sqrt{z^2(t)}} dt = i\int_{t_i}^{0} \frac{Z}{\sqrt{\tilde{z}^2(\tau)}} d\tau \tag{117}$$

with $\tilde{z}(\tau) = z(t_r + i\tau)$ along the integration path $t = t_r + i\tau$, $\tau \in [t_i, 0]$, as shown in Fig. 13(a). The superscript (α) is suppressed here. For the sub-barrier trajectory in polarization direction calculated from (52)

$$z(t) = \frac{A_0}{\omega}\left[\cos\omega t - \text{Re}\cos\omega t_s\right] + p_z\left[t - \text{Re}t_s\right] \tag{118}$$

results. Separating the real and imaginary parts of $\tilde{z}(\tau)$,

$$\tilde{z}(\tau) = a(\tau) + ib(\tau), \tag{119}$$

one finds

$$\begin{aligned} a(\tau) \equiv \text{Re}[\tilde{z}(\tau)] &= \frac{A_0}{\omega}\cos\omega t_r\left(\cosh\omega\tau - \cosh\omega t_i\right), \\ b(\tau) \equiv \text{Im}[\tilde{z}(\tau)] &= p_z\tau - \frac{A_0}{\omega}\sin\omega t_r \sinh\omega\tau. \end{aligned} \tag{120}$$

In the long wavelength limit $\omega \to 0$, the functions sinh and cosh in $a(\tau)$ and $b(\tau)$ can be expanded about $\omega = 0$, leading to

$$\begin{aligned} a(\tau) &\simeq \frac{A_0}{2}\omega\cos\omega t_r\left(\tau^2 - t_i^2\right), \\ b(\tau) &\simeq \tau\Delta \end{aligned} \tag{121}$$

with

$$\Delta \simeq p_z - A_0\sin\omega t_r \simeq \frac{A_0}{2}\omega^2 t_i^2 \sin\omega t_r. \tag{122}$$

Let us consider emission times t_r for positive p_z. In this case $0 < \omega t_r < \pi$ and thus $\Delta > 0$. As $\tau > 0$ [60] as well, $b(\tau) > 0$. Hence the integrand in W^{subcc} in (117) may be simplified by choosing the positive root to $Z[\tilde{z}^2(\tau)]^{-1/2} = Z/\tilde{z}(\tau)$ for $a(\tau) \geq 0$ and $Z[\tilde{z}^2(\tau)]^{-1/2} = -Z/\tilde{z}(\tau)$ for $a(\tau) < 0$ so that it is sufficient to consider the simplified action

$$W_{\pm}^{\text{subcc}'} = \pm i \int_{t_i}^{0} \frac{Z}{\tilde{z}(\tau)} d\tau. \tag{123}$$

The real part of this action,

$$\text{Re}W_{\pm}^{\text{subcc}'} = \pm \int_{t_i}^{0} \frac{Zb(\tau)}{a^2(\tau) + b^2(\tau)} d\tau,$$

is relevant for interference patterns in the spectra. Inserting Eq. (120), with (115) for $p_x = 0$ and $\omega \to 0$,

$$A_0 \omega t_i \cos \omega t_r \simeq \mp \sqrt{2I_p},$$

leads to

$$\begin{aligned} \text{Re}W_{\text{cc}}^{\text{sub}'} &= \pm \frac{2t_i^2 \Delta}{I_p} \int_{t_i}^{0} \frac{\tau}{\tau^4 + 2\left[\left(\Delta^2/I_p\right) - 1\right] t_i^2 \tau^2 + t_i^4} d\tau \\ &= \pm \frac{1}{\sqrt{2I_p - \Delta^2}} \arctan \left[\frac{\Delta^2 t_i^2 - I_p t_i^2 + I_p \tau^2}{t_i^2 \sqrt{-\Delta^4 + 2\Delta^2 I_p}} \right] \Bigg|_{t_i}^{0} \\ &\overset{\Delta \to 0}{\simeq} \mp \frac{Z}{\sqrt{2I_p}} \frac{\pi}{2}. \end{aligned} \tag{124}$$

It follows from Eqs. (120) and (116) that, for a given p_z, the two-saddle point times $t_s^{(1)}$ and $t_s^{(2)}$ are such that $a^{(1)}(\tau) = -a^{(2)}(\tau)$ and $b^{(1)}(\tau) = b^{(2)}(\tau)$. The opposite signs of $a(\tau)$ have been considered already in our calculation of $\text{Re}W_{\pm}^{\text{subcc}'}$. Hence

$$|\phi^{\text{subcc}}| = \left| \text{Re}W_{+}^{\text{subcc}'} - \text{Re}W_{-}^{\text{subcc}'} \right| \simeq \frac{Z\pi}{\sqrt{2I_p}}, \tag{125}$$

as claimed in Eq. (112).

For a hydrogen-like ion in a state with principle quantum number $n = 1, 2, 3, \ldots$, we have $I_p = Z^2/(2n^2)$ and thus $|\phi^{\text{subcc}}| = n\pi$. In particular, for ground states $n = 1$ we have independently of Z that $|\phi^{\text{subcc}}| = \pi$. This is the required phase shift for bringing the intra-cycle fringe pattern in agreement with the *ab initio* TDSE result [see Fig. 12(d)].

We compared TDSE and TCSFA results for other parameters Z, I_p, and n and find good agreement if the sub-CC is included, provided the minimum number of photons required for ionization $I_p/\omega \gg 1$ and the Keldysh parameter $\sqrt{I_p/(2U_p)} \lesssim 1$. Moreover, as Z is smaller, the approximation to use the zeroth-order, plain SFA trajectory for the sub-CC is better. Excited states $n > 1$ may introduce extra phase differences via the prefactors $\mathcal{P}(t_s^{(\alpha)})$ in Eq. (77).

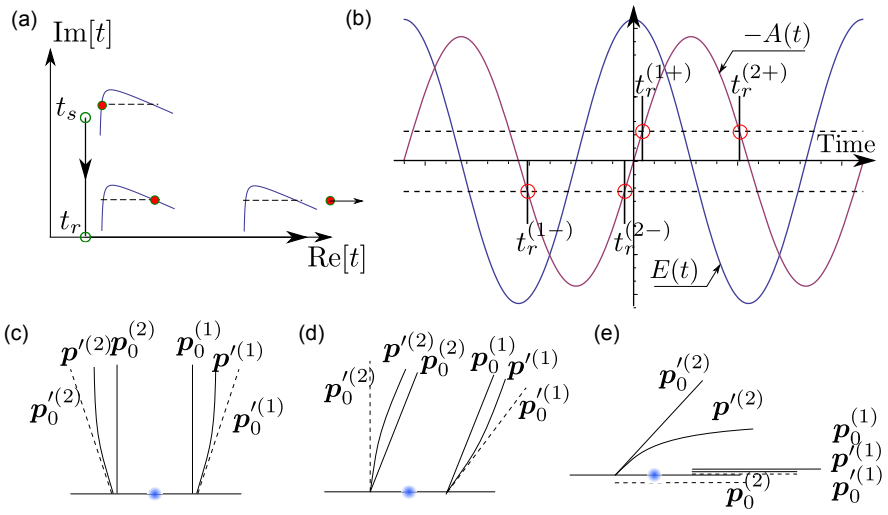

Figure 13: (a) Integration path in the complex time plane. Starting at t_s we integrate parallel to the imaginary time axis down to t_r on the real axis, and then along the real axis to infinity. The corresponding situation in position space around the tunneling barrier are illustrated: at t_s the electron is inside the atom in front of the barrier, at t_r it leaves the barrier at the tunnel exit and subsequently moves in the classically allowed region. (b) Real parts of the saddle point times for a monochromatic laser with the electric field $E(t) = E_0 \cos \omega t$ and vector potential $A(t) = -A_0 \sin \omega t$, $E_0 = A_0 \omega$. The superscripts of t_r indicate the sign of the asymptotic momentum p_z; the numbers 1 and 2 indicate whether the corresponding quantum trajectory is "long" or "short", respectively. The negative vector potential and the electric field in arbitrary units are indicated. Panel (c)-(e) illustrate the asymptotes of real trajectories in perpendicular direction $\theta = \pi/2$ (c), for an angle $0 < \theta < \pi/2$ (d), and parallel to the polarization direction, $\theta = 0$ (e). The bold solid lines $\vec{p}_0^{(1)}$ and $\vec{p}_0^{(2)}$ represent trajectories in plain SFA where initial and asymptotic momentum $\vec{p}$ are equal. Thin solid lines represent the corresponding TCSFA trajectories, which start off like the dashed trajectories with a modified initial momentum but then get Coulomb-distorted such that the asymptotic momentum is $\vec{p}$.

5.2.3 *Momentum Distribution in Perpendicular Direction*

In subsection 5.2.2, we show that the sub-CC in the polarization direction contributes an extra phase shift ϕ^{subcc}, which approaches $\pi/\sqrt{2I_p}$ in the long-wavelength limit. The analysis starts from the conventional picture of interference between long-short trajectories with the corresponding saddle points $t_s^{(1)}$ and $t_s^{(2)}$. We are also interested in effects from the sub-CC in the perpendicular direction $p_z = 0$. In the SFA, the short and long trajectories are asymptotically parallel, as shown in Figs. 13(c-e). In the perpendicular direction [Fig. 13(c)], the parallel asymptotes are vertical when two saddle points merge as $p_z \to 0$ in Eq. (114). One easily verifies that in Fig. 13(b), $t_r^{(1+)}$ merges with $t_r^{(2-)}$ and $t_r^{(2+)}$ merges with $t_r^{(1-)}$. Hence, in plain SFA the momenta and the saddle point times of long and short trajectories become degenerate in perpendicular direction [$\vec{p}_0^{(1)}$ and $\vec{p}_0^{(2)}$ in Fig. 13(c)]. However, with the long-range Coulomb interaction included, this degeneracy is lifted. In order to have a common asymptotic momentum $\vec{p}'$ the initial momenta $\vec{p}_0'$ must be different, as indicated in Fig. 1(c).

In order to cancel the longitudinal shift induced by the long-range Coulomb distortion, the two trajectories should satisfy

$$p_{0z}^{(1)} = -p_{0z}^{(2)}, \quad p_{0x}^{(1)} = p_{0z}^{(2)}.$$

The corresponding saddle points are easily found for these criteria from Fig. 13(b). Taking, e. g., the saddle point $(1+)$ as the reference, the other saddle point is $(1-)$. Therefore, the initial condition for these trajectories are

$$\begin{aligned} p_{0z}^{(1+)} &= -p_{0z}^{(1-)}, \quad p_{0x}^{(1+)} = p_{0x}^{(1-)}, \\ t_r^{(1+)} &= \frac{\pi}{\omega} + t_r^{(1-)}, \quad t_i^{(1-)} = t_i^{(1+)}. \end{aligned} \tag{126}$$

In the following, the phase contribution $\phi_{c\perp}^{\text{subcc}}$, $\phi_{c\perp}^{\text{sub},0}$ and $\phi_{c\perp}^{\text{re}}$ are deduced, and the interference pattern in the perpendicular direction is inferred. The subscript "c" indicates that the phase difference between the trajectories has been generalized to allow for the real-space trajectory-distortion by the Coulomb force. The interference pattern in perpendicular direction is determined by the symmetry properties of the interfering trajectories, while it is independent of the detailed, Coulomb-modified dynamics because both trajectories of a pair collect equal phase distortions. This suggests that the SFA, TCSFA with or without sub-CC result in the same interference structure in the perpendicular direction, as will be discussed in the following.

5.2.3.1 *Phase difference from sub-CC: $\phi_{c\perp}^{subcc}$*

We show first that the sub-CC phase difference $\phi_{c\perp}^{subcc}$ does not contribute in (111),

$$\phi_{c\perp}^{subcc} = \mathrm{Re}\left[W_{\perp}^{subcc(1+)} - W_{\perp}^{subcc(1-)}\right] = 0. \tag{127}$$

The real part of the sub-CC action can be written down with the complex trajectory expressed by parallel and perpendicular components $z(t)$ and $x(t)$

$$\begin{aligned} \mathrm{Re}W^{subcc} &= \int_{t_s}^{t_r} \frac{dt}{\left[z(t)^2 + x(t)^2\right]^{1/2}} \\ &= i\int_{t_i}^{0} \frac{d\tau}{\left[\tilde{z}(\tau)^2 + \tilde{x}(\tau)^2\right]^{1/2}}. \end{aligned} \tag{128}$$

For a monochromatic laser pulse (100), the zeroth-order sub-barrier trajectories (100) as a function of $t = t_r + i\tau$ can be cast into [see (120), (121)]

$$\begin{aligned} \tilde{z}(\tau) &= \frac{E_0}{\omega^2}\cos(\omega t_r)\left(\cosh\omega\tau - \cosh\omega t_i\right) \\ &\quad + i\left(p_z\tau - \frac{E_0}{\omega^2}\sin\omega t_r \sinh\omega\tau\right) \end{aligned} \tag{129}$$

and

$$\tilde{x}(\tau) = ip_x\tau. \tag{130}$$

Substituting $t_r^{(1\pm)}$ and $p_z^{(1\pm)}$ into $\tilde{z}(\tau)$ (129), we find with the help of the conditions (126) $\tilde{z}^{(1+)}(\tau) = -\tilde{z}^{(1-)}(\tau)$. For $\tilde{x}(\tau)$ (130) clearly follows $\tilde{x}^{(1+)}(\tau) = \tilde{x}^{(1-)}(\tau)$. As a consequence, the integrands in (128) is identical for both trajectories. As the integration starts for both trajectories at $t_i^{(1+)} = t_i^{(1-)} = t_i$ we obtain $\mathrm{Re}W_{c\perp}^{subcc(1+)} = \mathrm{Re}W_{c\perp}^{subcc(1-)}$, i. e., the sub-CC phase difference vanishes, and (127) is proved.

In passing, we would like to mention that caution has to be exercised regarding which saddle-points are chosen for $p_z = 0$ if zeroth-order, plain SFA were used, for which the degeneracy of the saddle points is not lifted. If the "usual" long and short trajectories $(1+)$ and $(2+)$ with $t_r^{(1+)}$ and $t_r^{(2+)}$ shown in Fig. 13(b) are chosen, $\tilde{z}^{(2+)}(\tau)$ can be expressed by variables of $(1+)$ as

$$\begin{aligned} \tilde{z}^{(2+)}(\tau) &= -\frac{A_0}{\omega}\cos\left(\omega t_r^{(1+)}\right)\left(\cosh\omega t - \cosh\omega t_i\right) \\ &\quad + i\left[p_z^{(1+)}t - \frac{E_0}{\omega^2}\sin\left(\omega t_r^{(1+)}\right)\sinh\omega t\right]. \end{aligned} \tag{131}$$

Compared to (129), this expression differs by a sign only in the first term. Since $\tilde{x}^{(1+)}(\tau) = \tilde{x}^{(2+)}(\tau)$, the imaginary parts of $z(t)^2 + x(t)^2$ in the denominator of (128) for $(1+)$ and $(2+)$ are opposite in signs. It seems a paradox occurs: in the exact perpendicular direction, the

integrands are identical since the imaginary part in (131) is zero, and thus no phase difference exists. But a tiny longitudinal momentum p_z would lead to the abrupt appearance of a finite phase difference due to the multiplicity of the complex square-root function in the denominator, which is unphysical. The problem does not arise in the above employed sub-CC, thanks to the Coulomb distortion of the trajectories in real-space, which enforces $p_{0z}^{(1+)} = -p_{0z}^{(1-)}$, thus determining the relevant saddle-point times to be $(1+)$ and $(1-)$, not $(1+)$ and $(2+)$.

5.2.3.2 *Phase difference from sub-barrier propagation without Coulomb interaction:* $\phi_{c\perp}^{sub,0}$

After having identified the relevant saddle-points $(1+)$ and $(1-)$ we now show that

$$\phi_{c\perp}^{sub,0} = \mathrm{Re}\left[W^{sub,0(1+)} - W^{sub,0(1-)}\right] = 0. \tag{132}$$

Substituting a monochromatic laser field (100) into (83), we obtain

$$\begin{aligned} W^{sub,0} &= i\left(I_p + \frac{1}{2}p^2 + U_p\right)t_i - \frac{E_0 p_z}{\omega^2}\left[\cos\omega t_r - \cos\omega t_s\right] \\ &\quad + \frac{E_0^2}{8\omega^3}\left[\sin 2\omega t_r - \sin 2\omega t_s\right], \end{aligned} \tag{133}$$

where $p = \sqrt{p_z^2 + p_x^2}$. The real part reads

$$\mathrm{Re}W^{sub,0} = \frac{A_0 p_z}{\omega}\cos\omega t_r\left(\cosh\omega t_i - 1\right) - \frac{A_0^2}{4\omega}\sin 2\omega t_r \sinh^2\omega t_i. \tag{134}$$

Inserting $p_z^{(1\pm)}$ and $t_r^{(1\pm)}$ we find

$$\mathrm{Re}W_{c\perp}^{sub,0(1-)} = \mathrm{Re}W_{c\perp}^{sub,0(1+)}, \tag{135}$$

confirming Eq. (132). No information from the sub-barrier propagation is recorded in the perpendicular direction.

5.2.3.3 *Phase difference from real propagation:* $\phi_{c\perp}^{re}$

The interference pattern in the perpendicular direction is entirely determined by the real-time trajectories and the corresponding phase difference

$$\phi_c^{re} = W^{re(1+)} - W^{re(1-)}. \tag{136}$$

Given real trajectories $z(t)$, $x(t)$, $v_z(t)$ and $v_x(t)$ for $t \in [t_r, T_p]$, the action due to the propagation in real time is

$$W^{re} = -\int_{t_r}^{T_p}\left[\frac{1}{2}\left(v_z(t)^2 + v_x(t)^2\right) - \frac{1}{\sqrt{z(t)^2 + x(t)^2}} + I_p\right]dt. \tag{137}$$

The symmetry properties for two interfering trajectories in the perpendicular direction are illustrated in Fig. 13(c),

$$\begin{aligned} v_{z\perp}^{(1-)}(t) &= -v_{z\perp}^{(1+)}\left(t+\frac{\pi}{\omega}\right), \quad v_{x\perp}^{(1-)}(t) = v_{x\perp}^{(1+)}\left(t+\frac{\pi}{\omega}\right), \\ z_{\perp}^{(1-)}(t) &= -z_{\perp}^{(1+)}\left(t+\frac{\pi}{\omega}\right), \quad x_{\perp}^{(1-)}(t) = x_{\perp}^{(1+)}\left(t+\frac{\pi}{\omega}\right). \end{aligned} \tag{138}$$

Moreover, $t_r^{(1-)} = t_r^{(1+)} - \pi/\omega$. Casting $W_{\perp}^{\mathrm{re}(1-)}$ in terms of the variables $(1+)$ one finds

$$\begin{aligned} W_{\perp}^{\mathrm{re}(1-)} &= -\int_{t_r^{(1+)}}^{T_p+\pi/\omega} \left[\frac{1}{2}\left(v_{z\perp}^{(1+)}(t)^2 + v_{x\perp}^{(1+)}(t)^2\right)\right. \\ &\quad \left. -\frac{1}{\sqrt{z_{\perp}^{(1+)}(t)^2 + x_{\perp}^{(1+)}(t)^2}} + I_p\right] dt \\ &= -\int_{t_r^{(1+)}}^{T_p+\pi/\omega} I(t)dt. \end{aligned} \tag{139}$$

The phase difference $\phi_{\mathrm{c}\perp}^{\mathrm{re}} = W_{\perp}^{\mathrm{re}(1+)} - W_{\perp}^{\mathrm{re}(1-)}$ is thus given by

$$\phi_{\mathrm{c}\perp}^{\mathrm{re}} = \left[-\int_{t_r^{(1+)}}^{T_p} + \int_{t_r^{(1+)}}^{T_p+\pi/\omega}\right] I(t)dt = \int_{T_p}^{T_p+\pi/\omega} I(t)dt, \tag{140}$$

independent of the specific saddle-point pair under consideration. As $T_p \to \infty$ the asymptotic position in polarization direction remains finite, $z(t)|_{t\to\infty} \to z_\infty$, but $x(t)|_{t\to\infty} \to \infty$, leading to a vanishing phase difference due to the Coulomb potential. In the kinetic energy term of the integrand, $v_z(t)|_{t\to\infty} \to A(t)$ and $v_x(t)|_{t\to\infty} \to p_x$, so that

$$\begin{aligned} \phi_{\mathrm{c}\perp}^{\mathrm{re}} &= \int_{T_p}^{T_p+\pi/\omega} \left(\frac{1}{2}p_x^2 + \frac{1}{2}A(t)^2 + I_p\right) dt \\ &= \frac{\pi}{\omega}\left(\frac{1}{2}p_x^2 + I_p\right) + \frac{1}{2}\int_{T_p}^{T_p+\pi/\omega} A(t)^2 dt. \end{aligned} \tag{141}$$

Using $p_x = \sqrt{2\left(n\omega - U_p - I_p\right)}$ from the energy conservation for ATI in the perpendicular direction with n the number of absorbed photons and $U_p = \frac{1}{2}\frac{1}{2\pi/\omega}\int_0^{2\pi/\omega} A(t)^2 dt$ we find

$$\phi_{\mathrm{c}\perp}^{\mathrm{re}} = n\pi. \tag{142}$$

This result agrees with the findings in Ref. [90] that every other ATI ring is destructively "interfered away" in perpendicular direction. Because of the prefactor $\mathcal{P}(t_s^{(\alpha)})$ in (77) the interference is destructive for odd n in the case of even-parity initial states and *vice versa*.

The interference concerning the ATI rings in perpendicular direction predicted by (142) is confirmed by the results for ionization of H(1s) in a 9-cycle trapezoidal envelope laser pulse of 800 nm wavelength shown in Fig. 14. The other laser parameters are given in the figure caption.

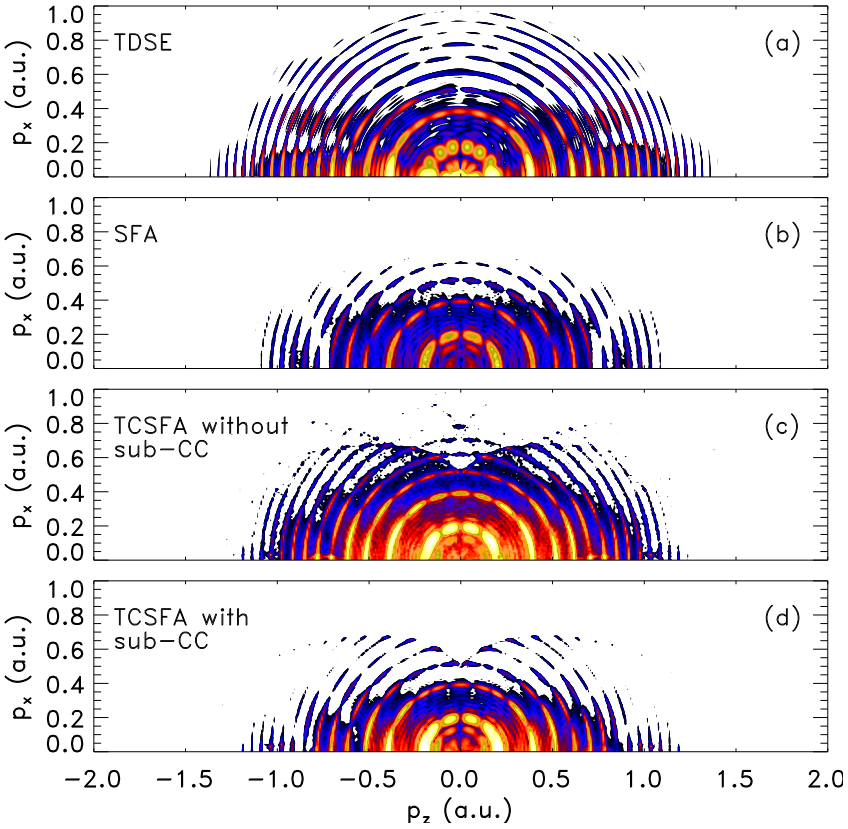

Figure 14: Same as Fig. 12 but for a 9-cycle, trapezoidal-envelope laser (2, 5, and 2 cycles for up-ramping, constant-envelope, and down-ramping, respectively). The wavelength is $\lambda = 800$ nm, the intensity is 10^{14} W/cm^2. In the spectrum calculated using the TCSFA with sub-CC (d) only trajectories of types T1 and T2 have been considered.

5.2.4 *On-Ring Nodal Structure*

The ATI peaks appear as rings of radius

$$p = \sqrt{2\left(n\omega - U_p - I_p\right)} \tag{143}$$

in the photoelectron momentum spectra. It is known from experiments that the ionization probability along the ATI rings is not isotropic but exhibits nodal structures. These structures, also visible in Fig. 14, have been analyzed recently within the SFA [90]. The radius of the ATI rings is well reproduced already by the plain SFA, which is verified by comparing Fig. 14(b) with the *ab initio* TDSE result Fig. 14(a). However, the positions of the nodes along low-order ATI rings do not agree well. Not even the number of minima and maxima agrees. Taking, e. g., the second ATI rings ($p = 0.3939$, absorption of 14 photons), for instance, the TDSE result in (a) shows 9 maxima along the ring, the plain SFA result in (b) only 7. The real time Coulomb corrected SFA in (c) does not affect the number of maxima. Instead, the sub-CC SFA in (d) does give the correct number. Along the next ATI-rings (absorption of 15 photons) TDSE and plain SFA agree already (10 maxima), and TCSFA with or without sub-CC does not change the nodal structures. Along the first ATI ring the TDSE shows 8 maxima, which is not properly reproduced, even with the sub-CC TCSFA, probably because our sub-barrier Coulomb correction involving only the zeroth-order plain SFA trajectories is insufficient.

Figure 15 shows the momentum distribution along the second ATI ring for the *ab initio* TDSE, the SFA and the TCSFA with or without sub-CC. TCSFA with sub-CC agrees well with the *ab initio* TCSFA result. The result from the TCSFA without sub-CC and the plain SFA are similar. They agree well with the TDSE around $\theta = \pi/2$ but deviate for smaller angles. As discussed above, there is one maximum less in the plain SFA and the TCSFA without sub-CC, as compared to the TDSE and the TCSFA with sub-CC. Hence we conclude that the nodal structure of low-order ATI rings is affected by the sub-CC. Higher-order ATI rings may be effected by the side-lobes (clearly visible in Fig. 14(a)) and discussed in [78].

5.3 CONCLUSION

In this chapter, the applications of the TCSFA to complicated interference patterns are discussed. We show that diverse spectral structures essentially originate from interferences between different types of trajectories, and the TCSFA provides a convenient tool for such exploration with the aid of trajectories.

In order to account for the disagreement in spectra between the plain SFA and *ab initio* TDSE results, we introduce the sub-CC and found substantial improvement to precisely describe fringe structures. The

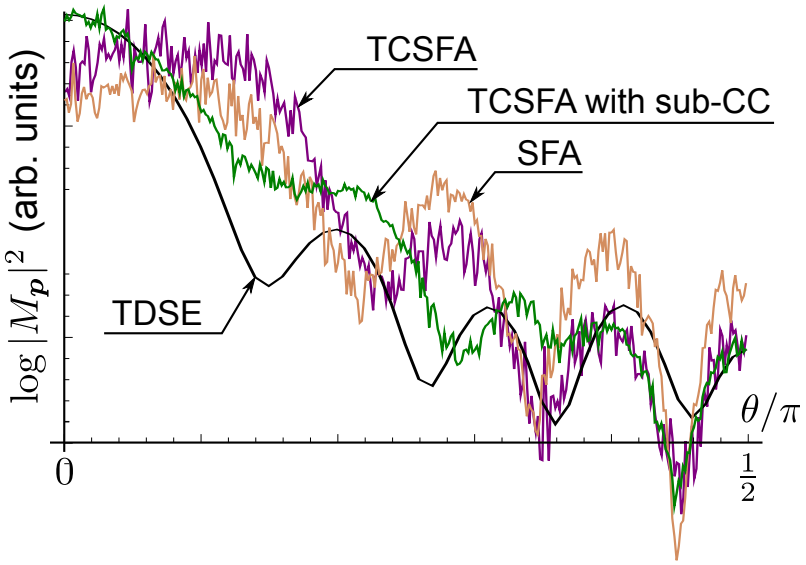

Figure 15: The ionization probability along the second ATI ring with $p = 0.3939$ in Fig. 14 according to the *ab initio* TDSE, the (plain) SFA, the TCSFA (without sub-CC), and the TCSFA with sub-CC result. The polar angle θ is in the range $[0, \pi/2]$, $\theta = 0$ corresponding to $p_x = 0$, and $\theta = \pi/2$ corresponding to $p_z = 0$. The plain SFA result is as noisy as the TCSFA because it was calculated using the same statistical sampling approach as for the TCSFA.

phase shift induced by the sub-CC takes a simple analytical form for all hydrogen-like atom in the long-wavelength limit. In addition the perpendicular distribution is found irrelevant with the sub-CC. Such intra-cycle interference provides potential applications for experimental exploration of ionization dynamics using photoelectron momentum spectra.

6 CONCLUSION AND OUTLOOK

The SFA lacks the proper description of the long-range Coulomb interaction between the electron and its parent ion. In this work, we have systematically developed the TCSFA method to overcome this deficiency. The TCSFA amounts to the trajectory-based SFA "patched" by the Coulomb interaction. In the TCSFA, the Coulomb interaction is incorporated by explicit evaluations of trajectories in combined fields, and the ionization probability is obtained by the coherent superposition of transition amplitudes, which are calculated along trajectories of the same asymptotic momentum. Using the TCSFA, we have explored the ionization dynamics of hydrogen-like atomic systems in a linearly polarized, long wavelength laser field by analyzing photoelectron momentum distributions. The SFA has an appealing interpretation in terms of quantum trajectories. With the incorporation of the Coulomb interaction, contributions from new types of trajectories have been identified. We successfully identified the origin of the so-called "ionization surprise", the LES, as the caustics formed by forward-scattering of trajectories at the Coulomb center in the laser field. Quantum mechanically, the interferences between trajectories account for recently observed interference patterns in experiments, which cannot be explained by the plain SFA. TCSFA allows for each quantum trajectory a splitting of the Coulomb correction into the part in the classically allowed region beyond the "tunnel exit" and the part "under the barrier" (sub-CC). We have analytically derived the phase shift caused by the sub-CC and explained the disagreement between positions of fringes for the plain SFA and the *ab initio* results. In brief, the TCSFA offers insights into any spectral feature in terms of trajectories.

In principle, extensions of the TCSFA to more complex systems are also feasible especially if a plain SFA has been already developed. In the following we present several possible applications. The most straightforward extension is towards two Coulomb centers, e. g., H_2^+, where the SFA for diatomic molecules, the molecular strong field approximation (MOSFA) [91, 92], has been established (see Sec. A.5).

The TCSFA may also be applied to the non-sequential double ionization (NSDI) in an effective two-electron system [93], though the computational burden would be heavy due to the sampling of trajectories in higher dimensional initial momentum space.

The extension to elliptically polarized laser fields is straightforward [94]. The influence of many-electron polarization effects could be in-

vestigated by incorporating a polarization potential into the equations of motion for the quantum trajectories [95, 96].

A

APPENDIX

A.1 ASYMPTOTIC FORM OF WAVE FUNCTION

The asymptotic form of hydrogen-like wave functions is used in Sec. 2.2.1 to evaluate the transition amplitude (29). In this Appendix we summarize the necessary prerequisites. The stationary Schrödinger equation for a point particle of the energy E and the mass μ in a radially symmetric potential $V(r)$ reads

$$\left[-\frac{\hbar^2}{2\mu}\nabla^2 + V(r)\right]\psi(\vec{r}) = E\psi(\vec{r}). \tag{144}$$

Since the orbital angular momentum is a constant of motion, we separate the solution of (144) into the radial function $f_l(r)$ and the spherical harmonics Y_{lm},

$$\psi(\vec{r}) = f_l(r)Y_{lm}(\theta,\phi). \tag{145}$$

Substituting (145) into (144), $f_l(r)$ satisfies the equation

$$\left[-\frac{\hbar^2}{2\mu}\left(\frac{d^2}{dr^2} + \frac{2}{r}\frac{d}{dr}\right) + \frac{l(l+1)\hbar^2}{2\mu r^2} + V(r)\right] f_l(r) = Ef_l(r). \tag{146}$$

Replacing $f_l(r)$ with $\phi_l(r)$, $f_l(r) = \phi_l(r)/r$, Eq. (146) becomes the stationary *radial Schrödinger equation*

$$\left[-\frac{\hbar^2}{2\mu}\frac{d^2}{dr^2} + V_{\text{eff}}(r)\right]\phi_l(r) = E\phi_l(r), \tag{147}$$

where

$$V_{\text{eff}}(r) = \frac{l(l+1)\hbar^2}{2\mu r^2} + V(r) \tag{148}$$

is the effective potential with the first term $l(l+1)\hbar^2/(2\mu r^2)$ the *centrifugal potential*. The three-dimensional equation (144) has been effectively reduced to (147) for a particle in a one-dimensional potential $V_{\text{eff}}(r)$.

The analytical solutions to Eq. (147) take different forms for bound states ($E < 0$) and the continuum ($E > 0$). The bound state in the Coulomb potential, $V(r) = -C/r$, is given by the Whittaker function

$$\phi_-(r) = W_{\nu,l+\frac{1}{2}}(2\kappa r)$$

with $\nu = \mu C/\hbar^2\kappa$ and $\kappa = \sqrt{2\mu|E|/\hbar^2}$. ν is the principal quantum number. Note that the wave function in most textbooks is usually

presented in the form of the associated Laguerre polynomial, which can be transformed into the Whittaker function by the Rodrigues representation,

$$L_n^k(r) = \frac{(-1)^n r^{-(k+1)/2}}{n!} e^{r/2} W_{k/2+n+1/2,k/2}(r).$$

When $r \gg 1$, as we usually assume for the tunnel exit, the asymptotic behavior of the Whittaker function results in

$$\phi_-(r) \underset{r\gg 1}{=} (2\kappa r)^\nu e^{-\kappa r}. \tag{149}$$

Substituting (149) and $f_l(r) = \phi_l(r)/r$ into (145), the asymptotic wave function for an arbitrary bound state of quantum numbers νlm is given by

$$\psi(\vec{r}) \simeq A r^{\nu-1} e^{-\kappa r} Y_{lm}(\hat{\vec{r}}), \tag{150}$$

where $\hat{\vec{r}}$ is the unit vector of $\vec{r}$. For the ground state, the asymptotic wave function is exact; for excited states, as long as the tunnel exit is far away from the origin, the asymptotic form is applicable.

Next, the Fourier transform of the asymptotic wave function (150),

$$\tilde{\psi}(\vec{k}) = \frac{1}{(2\pi)^{3/2}} \int d\vec{r} e^{-i\vec{k}\cdot\vec{r}} \psi(\vec{r}), \tag{151}$$

is shown. Using the partial wave expansion, the exponential function in (151) in spherical coordinates is given by

$$e^{-i\vec{k}\cdot\vec{r}} = \sum_{l'=0}^{\infty} \sqrt{4\pi\,(2l'+1)}\, i^{(-l')} \frac{j_{l'}(kr)}{kr} Y^*_{l',0}(\cos\gamma) \tag{152}$$

with γ the angle between $\hat{\vec{k}}$ (the unit vector of $\vec{k}$) and $\hat{\vec{r}}$, satisfying the relation (the addition theorem for spherical harmonics)

$$Y_{l',0}(\cos\gamma) = \sqrt{\frac{4\pi}{2l'+1}} \sum_{m'=-l'}^{l'} Y^*_{l',m'}(\hat{\vec{k}}) Y_{l',m'}(\hat{\vec{r}}). \tag{153}$$

Substituting the asymptotic wave function (150) and the exponential function (152) into (151) and applying the orthogonality relation for spherical harmonics which cancels the dependence on $\hat{\vec{r}}$, (151) becomes

$$\tilde{\psi}(\vec{k}) = \frac{1}{k}\sqrt{\frac{2}{\pi}} i^{-l} Y_{l,m}(\hat{\vec{k}}) \int_0^\infty j_l(kr) \left[A r^\nu e^{-\kappa r}\right] dr. \tag{154}$$

Using [86] for the last integral in (154), the asymptotic wave function in the momentum representation is given by

$$\tilde{\psi}(\vec{k}) \simeq 4\pi A (\pm 1)^l Y_{lm}(\hat{\vec{k}}) \frac{(2\kappa)^\nu \Gamma(\nu+1)}{(q^2+\kappa^2)^{\nu+1}}. \tag{155}$$

The mostly used expressions are listed in Table 1.

State	Fourier transform
$1s$	$\tilde{\psi}(\vec{q}) = \frac{4A\sqrt{\pi\kappa}}{(\vec{q}^2+\kappa^2)^2}$
$2s$	$\tilde{\psi}(\vec{q}) = \frac{16A\sqrt{\pi}\kappa^2}{(\vec{q}^2+\kappa^2)^3}$
$2p$	$\tilde{\psi}(\vec{q}) = \frac{16A\sqrt{3\pi}\kappa^2}{(\vec{q}^2+\kappa^2)^3}\,(\pm 1)\cos\theta$

Table 1: Fourier transforms of the asymptotic form, Eq. (155), for $\nu = 1, 2$, $l = 0, 1$, and $m = 0$.

A.2 SADDLE POINTS IN A MONOCHROMATIC LINEARLY POLARIZED FIELD

In this section, the saddle points used for the monochromatic laser field are derived. Substituting (100) into (35),

$$[p_z + A(t_s)]^2 + p_x^2 = -2I_p,$$

the SPE reduces to

$$p_z - \frac{E_0}{\omega}\sin\omega t_s = \pm i\sqrt{2I_p + p_x^2}.$$

With the complex saddle time $t_s = t_r + it_i$, $t_r, t_i \in \mathbb{R}$, the real and imaginary components are separated,

$$\sin\omega t_r \cosh\omega t_i = \frac{\omega p_z}{E_0}, \tag{156}$$

$$\cos\omega t_r \sinh\omega t_i = \mp\frac{\omega\sqrt{2I_p + p_x^2}}{E_0}. \tag{157}$$

Solving (156) and (157), two groups of solutions are found,

$$\begin{aligned} t_r^{(1)} &= \frac{1}{\omega}\arccos(c_2), \quad t_i^{(1)} = \frac{1}{\omega}\operatorname{arccosh}(c_3), \\ t_r^{(2)} &= \frac{1}{\omega}\arccos(-c_2), \quad t_i^{(2)} = \frac{1}{\omega}\operatorname{arccosh}(c_3), \end{aligned} \tag{158}$$

where

$$\begin{aligned} c_1 &= \sqrt{\left[E_0^2 + \omega^2\left(2I_p + p^2\right)\right]^2 - 4E_0^2\omega^2 p_z^2}, \\ &= \sqrt{(1+\beta)^2 - \frac{p_z^2}{U_p}} \\ c_2 &= \frac{\sqrt{E_0^2 - \omega^2\left(2I_p + p^2\right) + c_1}}{\sqrt{2}E_0} = \frac{1}{\sqrt{2}}\sqrt{1 - \beta + c_1}, \\ c_3 &= \frac{\sqrt{E_0^2 + \omega^2\left(2I_p + p^2\right) + c_1}}{\sqrt{2}E_0} = \frac{1}{\sqrt{2}}\sqrt{1 + \beta + c_1}, \end{aligned}$$

and $E_a^2 = \omega^2(2I_p + p^2)$, $\beta = E_a^2/E_0^2$.

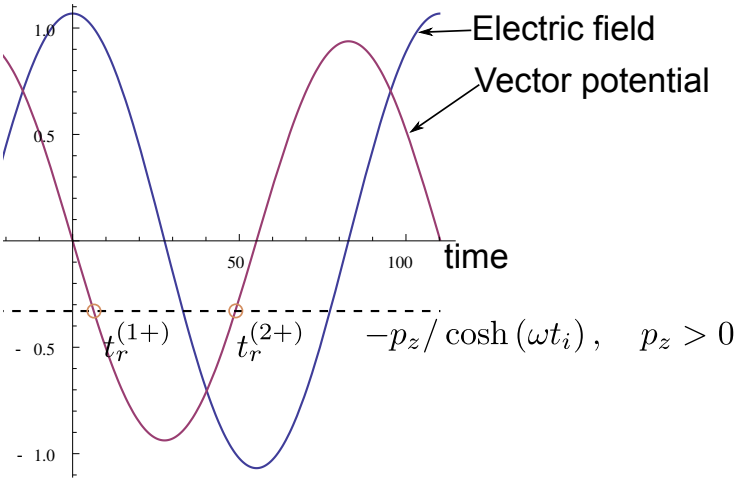

Figure 16: Illustration of the real parts of saddle points in the linearly polarized monochromatic laser field of the electric field (100).

The relation between two saddle points within one cycle is found from (158),

$$t_r^{(1)} = \frac{\pi}{\omega} - t_r^{(2)}, \quad t_i^{(1)} = t_i^{(2)} > 0. \tag{159}$$

For a pair of trajectories of saddle points satisfying (159), same imaginary parts, which imply that the trajectories are of the same weight, lead to the maximum contrast of interference fringes. Moreover, Eq. (156) shows that $t_r^{(\alpha)}$ is determined by the intersections between $-p_z/\cosh(\omega t_i)$ and the vector potential $A(t)$. We visualize this relation for real parts of saddle points in Fig. 16. $t_s^{(1)}$ and $t_s^{(2)}$ are assigned with signs "+" and "−" in Eq. (157), corresponding to the long and short trajectories, respectively.

By calculating $\vec{v}(t_r) = \vec{p}_0 + \vec{A}(t_r)$, the initial velocity when the electron emerges at the tunnel exit is also available,

$$v_z(t_r) = -2A(t_r)\sinh^2\left(\frac{\omega t_i}{2}\right), \tag{160}$$

$$v_x(t_r) = p_x. \tag{161}$$

From Eq. (160), one sees that $v_z(t_r)$ is small if the trajectory has a large weight (ωt_i is small), which justifies the assumption in the SMM that a photoelectron starts with $v_z(t_r) = 0$. Moreover one should note that $p_z(t_r)$ has the same sign as the sampling momentum p_{0z}.

A.3 FOURTH-ORDER RUNGE-KUTTA METHOD

Numerically, the classical fourth-order Runge-Kutta method (RK4) is widely used to solve systems of ODEs. The the algorithm for the nth time step is given by

$$\begin{aligned}
\vec{k}_1 &= hf(t_n, \vec{y}_n), \\
\vec{k}_2 &= hf(t_n + \frac{1}{2}h, \vec{y}_n + \frac{1}{2}\vec{k}_1), \\
\vec{k}_3 &= hf(t_n + \frac{1}{2}h, \vec{y}_n + \frac{1}{2}\vec{k}_2), \\
\vec{k}_4 &= hf(t_n + h, \vec{y}_n + \vec{k}_3), \\
\vec{y}_{n+1} &= \vec{y}_n + \frac{1}{6}\left[\vec{k}_1 + 2\vec{k}_2 + 2\vec{k}_3 + \vec{k}_4\right],
\end{aligned} \tag{162}$$

where $\vec{y}_n$ is a vector containing components of discrete dynamical variables ($\vec{r}$ and $\vec{v}$ in our work), t_n is the time, and h is the time step.

A.4 KEPLER'S ORBIT

The Lagrangian of a particle in a central field of potential $V(r)$ reads

$$L = T - V = \frac{1}{2}m\left(\dot{r}^2 + r^2\dot{\theta}^2\right) - V(r). \tag{163}$$

Substituting (163) into the Euler-Lagrange equation, the equations for θ and r are given by

$$\frac{\partial L}{\partial \theta} - \frac{d}{dt}\frac{\partial L}{\partial \dot{\theta}} = 0, \quad \frac{\partial L}{\partial r} - \frac{d}{dt}\frac{\partial L}{\partial \dot{r}} = 0, \tag{164}$$

respectively. The two equations in (164) imply the conservation of the angular momentum l

$$\frac{dl}{dt} \equiv \frac{d}{dt}\left(mr^2\dot{\theta}\right) = 0 \tag{165}$$

and the conservation of the energy

$$mr\dot{\theta}^2 - m\ddot{r} + f(r) = 0, \tag{166}$$

respectively. In (166), $f(r) = -\partial V(r)/\partial r$ is the force of the central field. Substituting (165), $\dot{\theta} = l/(mr^2)$, into (166), the radial equation for r is given by

$$\frac{l^2}{mr^3} - m\ddot{r} + f(r) = 0. \tag{167}$$

We reformulate Eq. (167),

$$m\ddot{r} = \frac{l^2}{mr^3} + f(r) = -\frac{d}{dr}\left[\frac{l^2}{2mr^2} + V(r)\right]. \tag{168}$$

Multiplying by dr/dt on both sides of (168),

$$m\dot{r}\ddot{r} = \frac{d}{dt}\left(\frac{1}{2}m\dot{r}^2\right) = -\frac{d}{dt}\left[\frac{l^2}{2mr^2} + V(r)\right],$$

we obtain

$$\frac{1}{2}m\dot{r}^2 + \frac{l^2}{2mr^2} + V(r) = \text{const.} \tag{169}$$

The constant is the total energy E of the system. Eliminating l with $l = mr^2\dot{\theta}$, we find

$$\frac{1}{2}m(\dot{r}^2 + r^2\dot{\theta}^2) + V(r) = E. \tag{170}$$

Next, the Kepler orbit is determined. Using Eqs. (169) and (170) we can write

$$dt = \pm\frac{dr}{\sqrt{\frac{2}{m}(E - V(r) - \frac{l^2}{2mr^2})}}.$$

Eliminating dt by using the conservation of the angular momentum, $\dot{\theta} = l/mr^2$, the relation between θ and r is given by

$$d\theta = \pm\frac{ldr}{mr^2\sqrt{\frac{2}{m}(E - V(r) - \frac{l^2}{2mr^2})}}.$$

By integrating from a radial distance r_0 when the angle is θ_0 to r, we have

$$\theta = \pm\int_{r_0}^{r}\frac{dr}{r^2\sqrt{\frac{2m}{l^2}[E - V(r)] - \frac{1}{r^2}}} + \theta_0.$$

Substituting the Coulomb potential $V(r) = -Z/r$, the relation between θ and r reads

$$\begin{aligned}
\theta - \theta_0 &= \pm\int_{r_0}^{r}\frac{dr}{r^2\sqrt{\frac{2m}{l^2}[E + \frac{Z}{r}] - \frac{1}{r^2}}} \\
&= \pm\int_{r_0}^{r}\frac{dr}{r^2\sqrt{-\left(\frac{1}{r} - \frac{mZ}{l^2}\right)^2 + \left(\frac{(mZ)^2}{l^4} + \frac{2mE}{l^2}\right)}} \\
&= \pm\int_{r_0}^{r} -\frac{1}{\sqrt{1 - u^2(r)}}d\left[u(r)\right] \\
&= \pm\arccos u(r)\big|_{r_0}^{r},
\end{aligned}$$

where

$$u(r) = \left(\frac{1}{r} - \frac{mZ}{l^2}\right)\left[\frac{(mZ)^2}{l^4} + \frac{2mE}{l^2}\right]^{-1/2}.$$

Choosing $\theta_0 = 0$ for $r_0 = r_{\min}$ (the perigee), we have $\theta = \arccos u(r)$, or

$$r = \left[\frac{mZ}{l^2} + \sqrt{\frac{(mZ)^2}{l^4} + \frac{2mE}{l^2}}\cos\theta\right]^{-1}.$$

In atomic units ($m = 1$), the equation for the conic section is given by

$$r = \frac{k}{1 + \epsilon \cos\theta}, \tag{171}$$

where $k = l^2/Z$ and $\epsilon = \sqrt{1 + 2El^2/Z^2}$. The sign of θ determines the direction of the motion, $dr/dt \propto \epsilon l \sin\theta/k = Z\epsilon \sin\theta/l$, and hence the sign of $l dr/dt$ can be determined. The electron moves towards the core as $dr/dt > 0$ and *vice versa*.

A.5 SFA TRANSITION AMPLITUDE FOR H_2^+

Let us consider a diatomic molecule having two Coulomb centers A and B with the internuclear vector $\vec{R}$. The nuclear wave packets for the initial and final states (ν_i and ν_f) are defined as $\varphi_{\mathrm{AB}\nu_f}(\vec{R})$ and $\varphi_{\mathrm{AB}\nu_i}(\vec{R})$, respectively. The transition amplitude for the photoelectron with the asymptotic momentum $\vec{p}$ in a diatomic molecule is given by [92]

$$M_{\vec{p}}(t, t') = i \int d\vec{R} \frac{\varphi^*_{\mathrm{AB}\nu_f}(\vec{R})\, \varphi_{\mathrm{AB}\nu_i}(\vec{R})}{\sqrt{2\left(1 + \mathcal{S}(\vec{R})\right)}} \sum_{J=\mathrm{A,B}} M_{\vec{p}J}(t, t'; \vec{R}), \tag{172}$$

with $\mathcal{S}(R)$ the overlap integral between the atomic orbitals for A and B with regard to the linear combination of atomic orbitals (the LCAO-MO method, see, e. g., Sec. 8.3 of [97]), and

$$\begin{aligned} M_{\vec{p}J}(t, t'; \vec{R}) = \int_{t'}^{t} d\tau \int d\vec{r}\, \phi^*_{e\vec{p}_f}(\vec{r}, \tau) \left(e_r \vec{r} + e_R \vec{R}\right) \cdot \vec{E}(\tau) \\ \times \psi_{1s}(\vec{r} - c_J \vec{R})\, e^{i\Delta E(R)\tau} \end{aligned} \tag{173}$$

denotes the contribution to the transition amplitude from the Coulomb center indexed by J, $J = \mathrm{A}, \mathrm{B}$. Here $\psi_{1s}(\vec{r})$ is the ground state atomic orbital for the ground state. The coefficients c_J can be found by the Rayleigh-Ritz method [97]. $\vec{r}$ is the position vector of the electron. The reduced charges e_r, e_R and the effective potential $\Delta E(R)$ for the molecular system are defined as (6a), (6b) and (42) in [92]. The sum in (172) explicates the interference induced by the two Coulomb centers, analogous to the interference in the double-slit experiment. If the time scale of the ionization dynamics is much smaller than that for the motion of the nuclear wave packets, we can use the fixed nuclear configuration for a given inter-nuclear distance $R = \left|\vec{R}\right|$ to simplify the problem. Hence we only consider the transition amplitude under the fixed nuclei approximation,

$$M_{\vec{p}}(t, t'; \vec{R}) \equiv \sum_{J=\mathrm{A,B}} M_{\vec{p}J}(t, t'; \vec{R}) = \int_{t'}^{t} d\tau\, e^{iS(\tau)} \sum_{J=\mathrm{A,B}} D_J(\tau; \vec{R}), \tag{174}$$

where $S(t)$ is the action defined in (175) and $D_J(t;\vec{R})$ defined in (176) is the dipole matrix element corresponding to the Coulomb center J. $S(t)$ is similar to the action (27),

$$S(t) = \int_0^\tau \left\{ \frac{1}{2m}\left[\vec{p} - e\vec{A}(\tau)\right]^2 + \Delta E(R) \right\} d\tau, \qquad (175)$$

except the effective ionization potential $\Delta E(R)$ depends on R.

Approximating $e_r\vec{r} + e_R\vec{R}$ by $e\vec{r}$ thanks to the huge mass-difference between the nuclei and the electron, the dipole matrix element $D_J(\tau;\vec{R})$ in (174) is given by

$$D_J(\tau;\vec{R}) = e\vec{E}(\tau)\cdot\int d\vec{r}\,(2\pi)^{-3/2}\, e^{-i\left[\vec{p}-e_r\vec{A}(\tau)\right]\cdot\vec{r}}\vec{r}\psi_{1s}(\vec{r}-c_J\vec{R}). \qquad (176)$$

With the translational symmetry

$$\psi_{1s}(\vec{r}-c_J\vec{R}) \to e^{-iec_J\vec{R}\cdot\vec{A}(\tau)}\psi_{1s}(\vec{r}-c_J\vec{R})$$

for the laser dressed initial state (vector potential $\vec{A}(t)$), the dipole matrix element reads

$$\begin{aligned} D_J(\tau;\vec{R}) &= e^{-iec_J\vec{R}\cdot\vec{A}(\tau)}e\vec{E}(t)\cdot\int d\vec{r}\,(2\pi)^{-3/2}\, e^{-i\left[\vec{p}-e_r\vec{A}(\tau)\right]\cdot\vec{r}}\vec{r}\psi_{1s}(\vec{r}-c_J\vec{R}) \\ &= e^{-ic_J\vec{p}\cdot\vec{R}}e\vec{E}(t)\cdot\left[i\frac{d}{d\vec{k}}\tilde{\psi}_{1s}(\vec{k}) + c_J\vec{R}\tilde{\psi}_{1s}(\vec{k})\right], \end{aligned} \qquad (177)$$

where $\vec{k} = \vec{p} - e\vec{A}(\tau)$, and

$$\tilde{\psi}_{1s}(\vec{k}) = \frac{1}{(2\pi)^{3/2}}\int d\vec{r}\,' e^{-i\vec{k}\cdot\vec{r}\,'}\psi_{1s}(\vec{r}\,')$$

is the Fourier transform of $\psi_{1s}(\vec{r})$. Hence the total dipole matrix element in (174) for the two Coulomb centers is given by

$$\sum_{J=\mathrm{A,B}} D_J(\tau) = e\vec{E}(t)\cdot\left[i\frac{d}{d\vec{k}}\tilde{\psi}_{1s}(\vec{k})\sum_{J=\mathrm{A,B}} e^{-ic_J\vec{p}\cdot\vec{R}} + \vec{R}\tilde{\psi}_{1s}(\vec{k})\sum_{J=\mathrm{A,B}} c_J e^{-ic_J\vec{p}\cdot\vec{R}}\right]. \qquad (178)$$

Substituting $c_A = 1/2$ and $c_B = -1/2$ into (178) for H_2^+, we find the dipole matrix element

$$\sum_{J=\mathrm{A,B}} D_J(\tau) = ie\vec{E}(t)\left[-\vec{R}\sin\left(\frac{\vec{p}\cdot\vec{R}}{2}\right)\tilde{\psi}_{1s}(\vec{k}) + 2\cos\left(\frac{\vec{p}\cdot\vec{R}}{2}\right)\frac{d\tilde{\psi}_{1s}(\vec{k})}{d\vec{k}}\right]. \qquad (179)$$

BIBLIOGRAPHY

[1] Tian-Min Yan, S. V. Popruzhenko, M. J. J. Vrakking, and D. Bauer. Low-Energy Structures in Strong Field Ionization Revealed by Quantum Orbits. *Physical Review Letters*, 105(25):253002, December 2010. (Cited on pages vii, 32, and 42.)

[2] Tian-Min Yan and D. Bauer. Sub-barrier Coulomb effects on the interference pattern in tunneling-ionization photoelectron spectra. *Physical Review A*, 86(5):053403, November 2012. (Cited on pages vii, 51, 53, 55, 57, 59, and 61.)

[3] Maria Göppert-Mayer. Über Elementarakte mit zwei Quantensprüngen. *Annalen der Physik*, 401:273–294, 1931. (Cited on pages 1 and 5.)

[4] G. Mainfray and G. Manus. Multiphoton ionization of atoms. *Reports on Progress in Physics*, 54(10):1333–1372, October 1991. (Cited on page 1.)

[5] G. S. Voronov and N. B. Delone. Ionization of the xenon atom by the electric field of ruby laser emission. *JETP Letters*, 1(2):66, March 1965. (Cited on page 1.)

[6] P. Agostini, G. Barjot, J. Bonnal, G. Mainfray, C. Manus, and J. Morellec. Multiphoton ionization of hydrogen and rare gases. *IEEE Journal of Quantum Electronics*, 4(10):667 – 669, October 1968. (Cited on page 1.)

[7] P. Agostini, F. Fabre, G. Mainfray, G. Petite, and N. K. Rahman. Free-Free Transitions Following Six-Photon Ionization of Xenon Atoms. *Physical Review Letters*, 42(17):1127–1130, April 1979. (Cited on page 1.)

[8] P. Kruit, J. Kimman, H. G. Muller, and M. J. van der Wiel. Electron spectra from multiphoton ionization of xenon at 1064, 532, and 355 nm. *Physical Review A*, 28(1):248–255, July 1983. (Cited on page 1.)

[9] W. Kohn. Nobel Lecture: Electronic structure of matter-wave functions and density functionals. *Reviews of Modern Physics*, 71(5):1253–1266, October 1999. (Cited on page 2.)

[10] P. Salières, B. Carré, L. Le D'eroff, F. Grasbon, G. G. Paulus, H. Walther, R. Kopold, W. Becker, D. B. Milošević, A. Sanpera, and M. Lewenstein. Feynman's Path-Integral Approach for Intense-Laser-Atom Interactions. *Science*, 292(5518):902 –905, May 2001. (Cited on pages 2 and 11.)

[11] W. Becker, F. Grasbon, R. Kopold, D. B. Milošević, G. G. Paulus, and H. Walther. Above-threshold ionization: From classical features to quantum effects. In Benjamin Bederson and Herbert Walther, editors, *Advances In Atomic, Molecular, and Optical Physics*, volume Volume 48, pages 35–98. Academic Press, 2002. (Cited on pages 2 and 11.)

[12] A. M. Perelomov and V. S. Popov. Ionization of Atoms in an Alternating Electrical Field. III. *JETP*, 25(2):336, 1967. (Cited on pages 2, 19, and 21.)

[13] M. V. Ammosov, N. B. Delone, and V. P. Krainov. Tunnel ionization of complex atoms and of atomic ions in an alternating electromagnetic field. *JETP*, 64(6):1191, 1986. (Cited on page 2.)

[14] S. L. Chin, Claude Rolland, P. B. Corkum, and Paul Kelly. Multiphoton Ionization of Xe and Kr with Intense 0.62-μm Femtosecond Pulses. *Physical Review Letters*, 61(2):153–156, July 1988. (Cited on page 2.)

[15] S. V. Popruzhenko, V. D. Mur, V. S. Popov, and D. Bauer. Strong Field Ionization Rate for Arbitrary Laser Frequencies. *Physical Review Letters*, 101(19):193003, November 2008. (Cited on page 2.)

[16] M. Bashkansky, P. H. Bucksbaum, and D. W. Schumacher. Asymmetries in Above-Threshold Ionization. *Physical Review Letters*, 60(24):2458–2461, June 1988. (Cited on page 2.)

[17] G. G. Paulus, F. Grasbon, A. Dreischuh, H. Walther, R. Kopold, and W. Becker. Above-Threshold Ionization by an Elliptically Polarized Field: Interplay between Electronic Quantum Trajectories. *Physical Review Letters*, 84(17):3791–3794, April 2000. (Cited on page 2.)

[18] Szczepan Chelkowski and André D. Bandrauk. Asymmetries in strong-field photoionization by few-cycle laser pulses: Kinetic-energy spectra and semiclassical explanation of the asymmetries of fast and slow electrons. *Physical Review A*, 71(5):053815, May 2005. (Cited on pages 2, 3, and 43.)

[19] J. Chen and C. H. Nam. Ion momentum distributions for He single and double ionization in strong laser fields. *Physical Review A*, 66(5):053415, November 2002. (Cited on page 2.)

[20] R. Moshammer, J. Ullrich, B. Feuerstein, D. Fischer, A. Dorn, C. D. Schröter, J. R. Crespo Lopez-Urrutia, C. Hoehr, H. Rottke, C. Trump, M. Wittmann, G. Korn, and W. Sandner. Rescattering of Ultralow-Energy Electrons for Single Ionization of Ne in the Tunneling Regime. *Physical Review Letters*, 91(11):113002, 2003. (Cited on page 2.)

[21] K. I. Dimitriou, D. G. Arbó, S. Yoshida, E. Persson, and J. Burgdörfer. Origin of the double-peak structure in the momentum distribution of ionization of hydrogen atoms driven by strong laser fields. *Physical Review A*, 70(6):061401, December 2004. (Cited on page 2.)

[22] A. Rudenko, K. Zrost, C. D. Schröter, V. L. B. de Jesus, B. Feuerstein, R. Moshammer, and J. Ullrich. Resonant structures in the low-energy electron continuum for single ionization of atoms in the tunnelling regime. *Journal of Physics B: Atomic, Molecular and Optical Physics*, 37:L407–L413, December 2004. (Cited on page 2.)

[23] L. Guo, J. Chen, J. Liu, and Y. Q. Gu. Origin of the double-peak structure in longitudinal momentum distributions for single ionization of an He atom in strong laser field. *Physical Review A*, 77(3):033413, March 2008. (Cited on page 2.)

[24] C. Y. Wu, Y. D. Yang, Y. Q. Liu, Q. H. Gong, M. Wu, X. Liu, X. L. Hao, W. D. Li, X. T. He, and J. Chen. Characteristic Spectrum of Very Low-Energy Photoelectron from Above-Threshold Ionization in the Tunneling Regime. *Physical Review Letters*, 109(4):043001, July 2012. (Cited on pages 2 and 32.)

[25] F. H. M. Faisal and G. Schlegel. Signatures of photon effect in the tunnel regime. *Journal of Physics B: Atomic, Molecular and Optical Physics*, 38(13):L223–L231, July 2005. (Cited on page 2.)

[26] A. S. Alnaser, C. M. Maharjan, P. Wang, and I. V. Litvinyuk. Multi-photon resonant effects in strong-field ionization: origin of the dip in experimental longitudinal momentum distributions. *Journal of Physics B: Atomic, Molecular and Optical Physics*, 39(17):L323–L328, September 2006. (Cited on page 2.)

[27] A. Rudenko, K. Zrost, Th. Ergler, A. B. Voitkiv, B. Najjari, V. L. B. de Jesus, B. Feuerstein, C. D. Schröter, R. Moshammer, and J. Ullrich. Coulomb singularity in the transverse momentum distribution for strong-field single ionization. *Journal of Physics B: Atomic, Molecular and Optical Physics*, 38(11):L191–L198, June 2005. (Cited on page 2.)

[28] D. G. Arbó, S. Yoshida, E. Persson, K. I. Dimitriou, and J. Burgdörfer. Interference Oscillations in the Angular Distribution of Laser-Ionized Electrons near Ionization Threshold. *Physical Review Letters*, 96(14):143003, April 2006. (Cited on pages 2, 26, and 48.)

[29] Zhangjin Chen, Toru Morishita, Anh-Thu Le, M. Wickenhauser, X. M. Tong, and C. D. Lin. Analysis of two-dimensional photoelectron momentum spectra and the effect of the long-range Coulomb potential in single ionization of atoms by intense

lasers. *Physical Review A*, 74(5):053405, November 2006. (Cited on page 2.)

[30] Diego G. Arbó, Konstantinos I. Dimitriou, Emil Persson, and Joachim Burgdörfer. Sub-Poissonian angular momentum distribution near threshold in atomic ionization by short laser pulses. *Physical Review A*, 78(1):013406, July 2008. (Cited on page 2.)

[31] T. Marchenko, H. G. Muller, K. J. Schafer, and M. J. J. Vrakking. Electron angular distributions in near-threshold atomic ionization. *Journal of Physics B: Atomic, Molecular and Optical Physics*, 43(9):095601, May 2010. (Cited on page 2.)

[32] C. I. Blaga, F. Catoire, P. Colosimo, G. G. Paulus, H. G. Muller, P. Agostini, and L. F. DiMauro. Strong-field photoionization revisited. *Nature Physics*, 5(5):335–338, 2008. (Cited on pages 2, 3, 32, and 43.)

[33] W. Quan, Z. Lin, M. Wu, H. Kang, H. Liu, X. Liu, J. Chen, J. Liu, X. T. He, S. G. Chen, H. Xiong, L. Guo, H. Xu, Y. Fu, Y. Cheng, and Z. Z. Xu. Classical Aspects in Above-Threshold Ionization with a Midinfrared Strong Laser Field. *Physical Review Letters*, 103(9):093001, 2009. (Cited on pages 2, 3, 32, 43, and 44.)

[34] Dylan C. Yost, Thomas R. Schibli, Jun Ye, Jennifer L. Tate, James Hostetter, Mette B. Gaarde, and Kenneth J. Schafer. Vacuum-ultraviolet frequency combs from below-threshold harmonics. *Nature Physics*, 5(11):815–820, 2009. (Cited on page 2.)

[35] Erik P. Power, Anne Marie March, Fabrice Catoire, Emily Sistrunk, Karl Krushelnick, Pierre Agostini, and Louis F. DiMauro. XFROG phase measurement of threshold harmonics in a Keldysh-scaled system. *Nature Photonics*, 4(6):352–356, 2010. (Cited on page 2.)

[36] Manoj Jain and Narkis Tzoar. Compton scattering in the presence of coherent electromagnetic radiation. *Physical Review A*, 18(2):538–545, August 1978. (Cited on page 2.)

[37] G. Duchateau, E. Cormier, and R. Gayet. Coulomb-Volkov approach of ionization by extreme-ultraviolet laser pulses in the subfemtosecond regime. *Physical Review A*, 66(2):023412, August 2002. (Cited on page 2.)

[38] G. L. Yudin, S. Chelkowski, and A. D. Bandrauk. Coulomb continuum effects in molecular interference. *Journal of Physics B: Atomic, Molecular and Optical Physics*, 39(2):L17–L24, January 2006. (Cited on page 2.)

[39] G. L. Yudin, S. Patchkovskii, P. B. Corkum, and A. D. Bandrauk. Attosecond photoelectron interference in the separable

Coulomb-Volkov continuum. *Journal of Physics B: Atomic, Molecular and Optical Physics*, 40(5):F93–F103, March 2007. (Cited on page 2.)

[40] Diego G. Arbó, Jorge E. Miraglia, María Silvia Gravielle, Klaus Schiessl, Emil Persson, and Joachim Burgdörfer. Coulomb-Volkov approximation for near-threshold ionization by short laser pulses. *Physical Review A*, 77(1):013401, January 2008. (Cited on pages 2 and 43.)

[41] A. M. Perelomov, V. S. Popov, and M. V. Terent'ev. Ionization of Atoms in an Alternating Electric Field: II. *JETP*, 24(1):207, 1967. (Cited on page 2.)

[42] V. S. Popov, V. P. Kuznetsov, and A. M. Perelomov. Quasiclassical Approximation for Nonstationary Problems. 26(1):222, 1968. (Cited on page 2.)

[43] Olga Smirnova, Michael Spanner, and Misha Ivanov. Analytical solutions for strong field-driven atomic and molecular one- and two-electron continua and applications to strong-field problems. *Physical Review A*, 77(3):033407, March 2008. (Cited on page 2.)

[44] Serguei Patchkovskii, Olga Smirnova, and Michael Spanner. Attosecond control of electron correlations in one-photon ionization and recombination. *Journal of Physics B: Atomic, Molecular and Optical Physics*, 45(13):131002, July 2012. (Cited on page 2.)

[45] P. B. Corkum. Plasma perspective on strong field multiphoton ionization. *Physical Review Letters*, 71(13):1994, 1993. (Cited on pages 2 and 13.)

[46] Bambi Hu, Jie Liu, and Shi-Gang Chen. Plateau in above-threshold-ionization spectra and chaotic behavior in rescattering processes. *Physics Letters A*, 236(5-6):533–542, December 1997. (Cited on page 3.)

[47] Chengpu Liu and Karen Z. Hatsagortsyan. Origin of Unexpected Low Energy Structure in Photoelectron Spectra Induced by Midinfrared Strong Laser Fields. *Physical Review Letters*, 105(11):113003, 2010. (Cited on pages 3, 32, and 44.)

[48] Farhad H. M. Faisal. Strong-field physics: Ionization surprise. *Nature Physics*, 5(5):319–320, 2009. (Cited on pages 3, 32, and 44.)

[49] M. Lewenstein, Ph. Balcou, M. Yu. Ivanov, Anne L'Huillier, and P. B. Corkum. Theory of high-harmonic generation by low-frequency laser fields. *Physical Review A*, 49(3):2117, March 1994. (Cited on page 5.)

[50] Andreas Becker and Farhad H. M. Faisal. Correlated Keldysh-Faisal-Reiss theory of above-threshold double ionization of He in intense laser fields. *Physical Review A*, 50(4):3256–3264, October 1994. (Cited on page 5.)

[51] Andreas Becker and Farhad H. M. Faisal. Mechanism of laser-induced double ionization of helium. *Journal of Physics B: Atomic, Molecular and Optical Physics*, 29(6):L197–L202, March 1996. (Cited on page 5.)

[52] A. Becker and Farhad H. M. Faisal. Interplay of electron correlation and intense field dynamics in the double ionization of helium. *Physical Review A*, 59(3):R1742–R1745, March 1999. (Cited on page 5.)

[53] S. P. Goreslavskii, S. V. Popruzhenko, R. Kopold, and W. Becker. Electron-electron correlation in laser-induced nonsequential double ionization. *Physical Review A*, 64(5):053402, October 2001. (Cited on page 5.)

[54] S. V. Popruzhenko, Ph. A. Korneev, S. P. Goreslavski, and W. Becker. Laser-Induced Recollision Phenomena: Interference Resonances at Channel Closings. *Physical Review Letters*, 89(2):023001, June 2002. (Cited on page 5.)

[55] C. Figueira de Morisson Faria and X. Liu. Electron-electron correlation in strong laser fields. *Journal of Modern Optics*, 58(13):1076–1131, 2011. (Cited on page 5.)

[56] L. V. Keldysh. Ionization in the Field of a Strong Electromagnetic Wave. *Zh. Eksp. Teor. Fiz.*, 47:1945–1957, 1964. (Cited on page 8.)

[57] Farhad H. M. Faisal. Multiple absorption of laser photons by atoms. *Journal of Physics B: Atomic and Molecular Physics*, 6(4):L89–L92, April 1973. (Cited on page 8.)

[58] Howard R. Reiss. Effect of an intense electromagnetic field on a weakly bound system. *Physical Review A*, 22(5):1786–1813, November 1980. (Cited on pages 8 and 49.)

[59] Norman Bleistein and Richard A. Handelsman. *Asymptotic Expansions of Integrals*. Dover Publications, November 2010. (Cited on page 11.)

[60] Lev Davidovich Landau and E. M. Lifshitz. *Quantum Mechanics: Non-Relativistic Theory*. Butterworth-Heinemann, 1977. (Cited on pages 11, 18, and 55.)

[61] G. F. Gribakin and M. Yu. Kuchiev. Multiphoton detachment of electrons from negative ions. *Physical Review A*, 55(5):3760, May 1997. (Cited on page 11.)

[62] M. V. Berry and K. E. Mount. Semiclassical approximations in wave mechanics. *Reports on Progress in Physics*, 35(1):315–397, January 1972. (Cited on page 11.)

[63] F. Lindner, M. G. Schätzel, H. Walther, A. Baltuška, E. Goulielmakis, F. Krausz, D. B. Milošević, D. Bauer, W. Becker, and G. G. Paulus. Attosecond Double-Slit Experiment. *Physical Review Letters*, 95(4):040401, July 2005. (Cited on page 12.)

[64] R. Gopal, K. Simeonidis, R. Moshammer, Th. Ergler, M. Dürr, M. Kurka, K.-U. Kühnel, S. Tschuch, C.-D. Schröter, D. Bauer, J. Ullrich, A. Rudenko, O. Herrwerth, Th. Uphues, M. Schultze, E. Goulielmakis, M. Uiberacker, M. Lezius, and M. F. Kling. Three-Dimensional Momentum Imaging of Electron Wave Packet Interference in Few-Cycle Laser Pulses. *Physical Review Letters*, 103(5):053001, July 2009. (Cited on pages 12 and 43.)

[65] V. Popov. Imaginary-time method in quantum mechanics and field theory. *Physics of Atomic Nuclei*, 68(4):686–708, 2005. (Cited on pages 12 and 15.)

[66] H. B. van Linden van den Heuvell and H. G. Muller. *Multiphoton Processes (Cambridge Studies in Modern Optics: 8).* Cambridge Univ. Press, 1988. (Cited on page 12.)

[67] G. G. Paulus, W. Becker, W. Nicklich, and H. Walther. Rescattering effects in above-threshold ionization: a classical model. *Journal of Physics B: Atomic, Molecular and Optical Physics*, 27(21):L703–L708, November 1994. (Cited on pages 12 and 14.)

[68] G. G. Paulus, W. Becker, and H. Walther. Classical rescattering effects in two-color above-threshold ionization. *Physical Review A*, 52(5):4043–4053, November 1995. (Cited on page 12.)

[69] P. Eckle, A. N. Pfeiffer, C. Cirelli, A. Staudte, R. Dörner, H. G. Muller, M. Büttiker, and U. Keller. Attosecond Ionization and Tunneling Delay Time Measurements in Helium. *Science*, 322(5907):1525 –1529, December 2008. (Cited on page 16.)

[70] T.-M. Yan, S. V. Popruzhenko, M. J. J. Vrakking, and D. Bauer. *Multiphoton Processes and Attosecond Physics, Springer Proceedings in Physics 125*. Springer-Verlag, 2012. (Cited on page 23.)

[71] S. V. Popruzhenko and D. Bauer. Strong field approximation for systems with Coulomb interaction. *Journal of Modern Optics*, 55(16):2573–2589, September 2008. (Cited on page 23.)

[72] H. Bach. Algorithm 365: complex root finding [C5]. *Communications of the ACM*, 12(12):686–687, December 1969. (Cited on page 25.)

[73] Chengpu Liu and Karen Z. Hatsagortsyan. Wavelength and intensity dependence of multiple forward scattering of electrons at above-threshold ionization in mid-infrared strong laser fields. *Journal of Physics B: Atomic, Molecular and Optical Physics*, 44(9):095402, May 2011. (Cited on page 32.)

[74] Chengpu Liu and Karen Z. Hatsagortsyan. Coulomb focusing in above-threshold ionization in elliptically polarized midinfrared strong laser fields. *Physical Review A*, 85(2):023413, February 2012. (Cited on page 32.)

[75] Alexander Kästner, Ulf Saalmann, and Jan M. Rost. Electron-Energy Bunching in Laser-Driven Soft Recollisions. *Physical Review Letters*, 108(3):033201, January 2012. (Cited on page 32.)

[76] Diego G. Arbó, Kenichi L. Ishikawa, Klaus Schiessl, Emil Persson, and Joachim Burgdörfer. Intracycle and intercycle interferences in above-threshold ionization: The time grating. *Physical Review A*, 81(2):021403, February 2010. (Cited on page 33.)

[77] A. I. Nikishov and V. I. Ritus. *JETP*, 23:168, 1966. (Cited on page 35.)

[78] Y. Huismans, A. Rouzée, A. Gijsbertsen, J. H. Jungmann, A. S. Smolkowska, P. S. W. M. Logman, F. Lépine, C. Cauchy, S. Zamith, T. Marchenko, J. M. Bakker, G. Berden, B. Redlich, A. F. G. van der Meer, H. G. Muller, W. Vermin, K. J. Schafer, M. Spanner, M. Yu. Ivanov, O. Smirnova, D. Bauer, S. V. Popruzhenko, and M. J. J. Vrakking. Time-Resolved Holography with Photoelectrons. *Science*, 331(6013):61 –64, January 2011. (Cited on pages 42, 48, 53, and 62.)

[79] Xue-Bin Bian, Y. Huismans, O. Smirnova, Kai-Jun Yuan, M. J. J. Vrakking, and André D. Bandrauk. Subcycle interference dynamics of time-resolved photoelectron holography with midinfrared laser pulses. *Physical Review A*, 84(4):043420, October 2011. (Cited on page 42.)

[80] Y. Huismans, A. Gijsbertsen, A. S. Smolkowska, J. H. Jungmann, A. Rouzée, P. S. W. M. Logman, F. Lépine, C. Cauchy, S. Zamith, T. Marchenko, J. M. Bakker, G. Berden, B. Redlich, A. F. G. van der Meer, M. Yu. Ivanov, T.-M. Yan, D. Bauer, O. Smirnova, and M. J. J. Vrakking. Scaling laws for photoelectron holography in the midinfrared wavelength regime. *Physical Review Letters*, 109(1):013002, July 2012. (Cited on pages 42 and 48.)

[81] F. Catoire, C. Blaga, E. Sistrunk, H. Muller, P. Agostini, and L. DiMauro. Mid-infrared strong field ionization angular distributions. *Laser Physics*, 19(8):1574–1580, 2009. (Cited on page 43.)

[82] D. B. Milošević, G. G. Paulus, D. Bauer, and W. Becker. Above-threshold ionization by few-cycle pulses. *Journal of Physics B: Atomic, Molecular and Optical Physics*, 39(14):R203–R262, July 2006. (Cited on page 45.)

[83] S. P. Goreslavskii and S. V. Popruzhenko. Rescattering and quantum interference near the classical cut-offs. *Journal of Physics B: Atomic, Molecular and Optical Physics*, 32(19):L531–L538, October 1999. (Cited on page 45.)

[84] C. Figueira de Morisson Faria, H. Schomerus, and W. Becker. High-order above-threshold ionization: The uniform approximation and the effect of the binding potential. *Physical Review A*, 66(4):043413, October 2002. (Cited on page 45.)

[85] M. V. Frolov, N. L. Manakov, and Anthony F. Starace. Analytic formulas for above-threshold ionization or detachment plateau spectra. *Physical Review A*, 79(3):033406, March 2009. (Cited on page 45.)

[86] I. S. Gradshteyn, I. M. Ryzhik, Alan Jeffrey, and Daniel Zwillinger. *Table of Integrals, Series, and Products, Sixth Edition*. Academic Press, 6th edition, August 2000. (Cited on pages 49 and 68.)

[87] Andrew M. Bruckner, Judith B. Bruckner, and Brian S. Thomson. *Real Analysis*. ClassicalRealAnalysis.com, 1997. (Cited on page 50.)

[88] T.-M. Yan, S. V. Popruzhenko, and D. Bauer. *Progress in Ultrafast Intense Laser Science*, volume 9. Springer-Verlag, 2013. (Cited on page 50.)

[89] Dieter Bauer and Peter Koval. Qprop: A Schrödinger-solver for intense laser-atom interaction. *Computer Physics Communications*, 174(5):396–421, March 2006. (Cited on page 51.)

[90] Ph. A. Korneev, S. V. Popruzhenko, S. P. Goreslavski, T.-M. Yan, D. Bauer, W. Becker, M. Kübel, M. F. Kling, C. Rödel, M. Wünsche, and G. G. Paulus. Interference Carpets in Above-Threshold Ionization: From the Coulomb-Free to the Coulomb-Dominated Regime. *Physical Review Letters*, 108(22):223601, May 2012. (Cited on pages 60 and 62.)

[91] J. Muth-Böhm, A. Becker, and F. H. M. Faisal. Suppressed Molecular Ionization for a Class of Diatomics in Intense Femtosecond Laser Fields. *Physical Review Letters*, 85(11):2280–2283, September 2000. (Cited on page 65.)

[92] D. B. Milošević. Strong-field approximation for ionization of a diatomic molecule by a strong laser field. *Physical Review A*, 74(6):063404, December 2006. (Cited on pages 65 and 73.)

[93] M. Yu Kuchiev. ATI as a source for multiply charged ion production in a laser field. *Journal of Physics B: Atomic, Molecular and Optical Physics*, 28(23):5093–5115, December 1995. (Cited on page 65.)

[94] S. V. Popruzhenko, G. G. Paulus, and D. Bauer. Coulomb-corrected quantum trajectories in strong-field ionization. *Physical Review A*, 77(5):053409, May 2008. (Cited on page 65.)

[95] Adrian N. Pfeiffer, Claudio Cirelli, Mathias Smolarski, Darko Dimitrovski, Mahmoud Abu-samha, Lars Bojer Madsen, and Ursula Keller. Attoclock reveals natural coordinates of the laser-induced tunnelling current flow in atoms. *Nature Physics*, 8(1):76–80, 2012. (Cited on page 66.)

[96] Jochen Maurer, Darko Dimitrovski, Lauge Christensen, Lars Bojer Madsen, and Henrik Stapelfeldt. Molecular-Frame 3D Photoelectron Momentum Distributions by Tomographic Reconstruction. *Physical Review Letters*, 109(12):123001, September 2012. (Cited on page 66.)

[97] Peter W. Atkins and Ronald S. Friedman. *Molecular Quantum Mechanics*. OUP Oxford, November 2010. (Cited on page 73.)

ACKNOWLEDGMENTS

The completion of this thesis is due, in no small part, to the help of many people. Foremost I would like to thank my supervisor, Professor Bauer, for his tremendous support and patient supervision during these years, from Heidelberg to Rostock, since 2009 till now. I am deeply grateful for the opportunity he gave me to work in the field of theoretical strong-field physics. He directed me into the fascinating world of physics and shared his expert experience with us. The inspirations from him never end. Without him, the completion of this thesis is simply impossible. On a personal note, I always feel indebted for his unfailing help, whether on the research or on my personal life. Many thanks go to our long-term collaborator from Moscow, Dr. Sergey Popruzhenko. The amazing analytical techniques he brought into our work are always of great help with deep insights. I have learned much from him—not only about specific skills, but also the methodology and scientific attitude. I would like to thank our secretary, Frau Hertzfeldt, and all group members of AG Quantentheorie und Vielteilchensysteme. Tatyana is always willing to give a hand when I encountered difficulties. The advice from Yaroslav often hits the mark and turns out helpful. It is nice to know Martins shares the same birthday with me. Since the days in Heidelberg, Varun has always been a nice travel companion and we really spent quite a few time out of the office. A lot of thanks to Julius—you will never regret having him as the officemate. I bothered him many times for correcting my poor German translations. Thanks to Volker for his trouble shooting as our system administrator. Whenever the computer resisted working he always came to my rescue. I would also like to thank Thomas, Mohammad, Nils and Franziska. There is a lot of fun as a member in this group.

Special thanks to the International Max Planck Research School Quantum Dynamics (IMPRS-QD) for funding my PhD study. Though I did not spend long time in Heidelberg, I still remember many colleagues in Max-Planck-Institut für Kernphysik (MPI-K). Many thanks to their help during the early days of my PhD study, especially when it was my first time studying abroad and living far away from my hometown. The academic atmosphere there is also impressive.

I have stayed in Rostock for more than three years. I really like the city—it is simple, tidy and open, just like the peaceful sea. Whether the weather is sunny or cloudy, it is always addicting to spend some time along the beach. The fresh sea air occasionally reminds me of my hometown and I never feel lonely.

At last but not least, I am grateful to my family—my parents and my grandparents, for their emotional support and endless love—though they are far away, they never fade.

ERKLÄRUNG

Ich versichere hiermit an Eides statt, dass ich die vorliegende Arbeit selbstständig angefertigt und ohne fremde Hilfe verfasst habe. Dazu habe ich keine außer den von mir angegebenen Hilfsmitteln und Quellen verwendet und die den benutzten Werken inhaltlich und wörtlich entnommenen Stellen habe ich als solche kenntlich gemacht.

Rostock, 26 November 2012

Tian-Min Yan